UC Irvine
UC Irvine Electronic Theses and Dissertations

Title

Polycrystalline Microporous Media: Hydraulic Transport and Two-Phase Heat Transfer Behaviors

Permalink

https://escholarship.org/uc/item/7tz186dt

Author

Pham, Quang Nhat

Publication Date

2020

Peer reviewed|Thesis/dissertation

UNIVERSITY OF CALIFORNIA,
IRVINE

Polycrystalline Microporous Media: Hydraulic Transport and Two-Phase Heat Transfer
Behaviors

DISSERTATION

submitted in partial satisfaction of the requirements
for the degree of

DOCTOR OF PHILOSOPHY

in Materials and Manufacturing Technology

by

Quang Nhat Pham

Dissertation Committee:
Assistant Professor Yoonjin Won, Chair
Associate Professor Lorenzo Valdevit
Associate Professor Timothy Rupert

2020

DEDICATION

To my family, from around the world.

TABLE OF CONTENTS

LIST OF FIGURES

LIST OF TABLES

ACKNOWLEDGMENTS

I am grateful to my advisor, Dr. Yoonjin Won, for giving me the opportunity to conduct research and mature as a scientist. Special thanks to Dr. Michael Barako, whose guidance and mentorship were invaluable to the development of my projects and the shaping of my professional scientific inquiries.

Thank you to my committee members, Dr. Lorenzo Valdevit and Dr. Timothy Rupert, who have graciously provided their invaluable time toward reviewing this dissertation and supporting me throughout this phase.

Thank you, Sarah, for being the light in my life and unconditionally supporting me; Laia for making everyday an enjoyable experience in lab; all my labmates and friends who have helped and supported my continual growth.

Lastly, I am tremendously thankful to have my family, from around the world, as the constant foundation within my life. I am forever appreciative of their love and in debt to their sacrifices.

VITA

Quang Nhat Pham

EDUCATION

Ph.D. in Materials & Manufacturing Technology   **2020**
University of California, Irvine   *Irvine, California*

MS in Mechanical & Aerospace Engineering   **2018**
University of California, Irvine   *Irvine, California*

BS in Mechanical Engineering   **2015**
University of Virginia   *Charlottesville, Virginia*

BA in Studio Art (Painting)   **2015**
University of Virginia   *Charlottesville, Virginia*

PROFESSIONAL EXPERIENCES

Graduate Research Assistant   **2015–2020**
University of California, Irvine   *Irvine, California*

Materials and Processing Intern   **2019–2020**
Northrop Grumman Aerospace Systems   *Redondo Beach, California*

Undergraduate Research Assistant   **2012–2015**
University of Virginia   *Charlottesville, Virginia*

Research Assistant Intern   **2014–2014**
Commonwealth Center for Advanced Manufacturing   *Disputanta, Virginia*

TEACHING EXPERIENCES

MAE 120: Heat and Mass Transport   **Fall 2019**
University of California, Irvine (Teaching Assistant)   *Irvine, California*

ENGR 190W: Communications in the Professional World   **Spring 2019**
University of California, Irvine (Teaching Assistant)   *Irvine, California*

MAE 120: Heat and Mass Transport   **Fall 2016**
University of California, Irvine (Teaching Assistant)   *Irvine, California*

JOURNAL PUBLICATIONS

Boiling Heat Transfer with Three-dimensionally Ordered Porous Architecture 2020
Pham, Q.N., Zhang, S., Hao, S., Montazeri, K., Lin, C.-H., Lee, J., Mohraz, A., Won, Y. *ACS Applied Materials & Interfaces.* 12, 19174.

Fabrication of Patterned Graphitized Carbon Wires Using Low Voltage Near-Field Electrospinning, Pyrolysis, Electrodeposition and Chemical Vapor Deposition 2020
George, D., Garcia, A., Pham, Q.N., Perez, M.R., Deng, J., Nguyen, M.T., Zhou, T., Chapa, S.O.M., Won, Y., Liu, C., Lo, R.C., Ragan, R., Madou, M. *Microsystems & Nanoengineering.* 6, 1.

Layered Manganese Metal-organic Framework with High Specific and Areal Capacitance for Hybrid Supercapacitors 2020
Shinde, P., Seo, Y., Khan, M.F., Pham, Q.N., Won, Y., Jun, S.C. *Chemical Engineering Journal.* 122982.

Evaporative Wicking Phenomena of Nanotextured Surfaces Heat for Pipe Application 2019
Le, D.V., Pham, Q.N., Lee, J., Won, Y. *Journal of Electronic Packaging.* 141, 031013.

The Control of Colloidal Grain Boundaries through Evaporative Vertical Self-Assembly 2019
Suh, Y., Pham, Q.N., Shao, B., and Won, Y. *Small.* 15, 1804523.

Droplets on Slippery Lubricant-Infused Porous Surfaces: A Macroscale to Nanoscale Perspective 2018
Pham, Q.N., Zhang, S., Montazeri, K., and Won, Y. *Langmuir.* 34, 14439.

Hierachical and Well-Ordered Porous Copper for Liquid Transport Properties Control 2018
Pham, Q.N., Shao, B., Kim, Y. and Won, Y. *ACS Applied Materials & Interfaces.* 10, 16015.

Controlled Wetting Properties through Heterogeneous Surfaces Containing Two-level Nanofeatures 2017
Dubey, P.P., Pham, Q.N., Cho, H., Kim, Y. and Won, Y. *ACS Omega.* 2, 7916.

Microscale Liquid Transport in Polycrystalline Inverse   **2017**
Opals across Grain Boundaries
Pham, Q.N., Barako, M.T., Tice, J. and Won, Y. *Scientific Reports.* 7, 10465.

Effect of Growth Temperature on the Synthesis of Car-   **2017**
bon Nanotube Arrays and Amorphous Carbon for Ther-
mal Applications
Pham, Q.N., Larkin, L.S., Lisboa, C.C., Saltonstall, C.B., Qiu, L., Schuler, J.D., Rupert,
T.J. and Norris, P.M. *Physica Status Solidi A.* 214, 1600852.

Thermal Conductivity of Vertically Aligned Carbon   **2014**
Nanotube Arrays: Growth Conditions and Tube Inho-
mogeneity
Bauer, M.L., Pham, Q.N., Saltonstall, C.B. and Norris, P.M. *Applied Physics Letter.*
105, 151909.

CONFERENCE PUBLICATIONS

Boiling Heat Transfer Using Spatially-Variant and Uni-   **Sept 2019**
form Microporous Coatings
Pham, Q.N., Suh, Y., Shao, B., and Won, Y. *Packaging and Integration of Electronic
and Photonic Microsystems (InterPACK)*, 1.

Boiling Heat Transfer Performance of Three-   **Jun 2018**
dimensionally Ordered Microporous Copper with
Modulated Pore Diameters
Pham, Q.N. Zhang, S., Cheng-Hui, L., Hao, S., and Won, Y. *Intersociety Conference
on Thermal and Thermomechanical Phenomena in Electronic Systems (ITherm)*, 1.

Designing an Autonomous Soil Monitoring Robot   **Jun 2015**
Piper, P.M., Vogel, J.S., Frahrenkrug, M.T., McNamee, S.J., Pham, Q.N., Lewin, G.C.
Systems and Information Engineering Design Symposium (SIEDS), 137.

HONORS AND AWARDS

Best Paper Award, Intersociety Conference on Thermal and Thermomechanical Phenom-
ena in Electronic Systems (2018)

Best Art in Science Award, Intersociety Conference on Thermal and Thermomechanical Phenomena in Electronic Systems (2018)

Poster Award, Southern California Society for Microscopy and Microanalysis Conference (2016)

Rodman Scholar, University of Virginia (2011)

Jefferson Book Award, University of Virginia (2011)

ABSTRACT OF THE DISSERTATION

Polycrystalline Microporous Media: Hydraulic Transport and Two-Phase Heat Transfer
Behaviors

by

Quang Nhat Pham

Doctor of Philosophy in Materials and Manufacturing Technology

University of California, Irvine, 2020

Assistant Professor Yoonjin Won, Chair

Through the extreme integration and compaction of high-power and high-frequency electronics, nano- and micromaterials have played a critical role in enabling next-generation thermal management technologies. Enormous efforts aim to leverage nanomaterials through advanced microfabrication techniques to reduce the thermal resistance between the device junction and the heat sink at different length scales. While the traditional convective air-cooling approach is limited in its effectiveness at dissipating high heat fluxes, the use of latent heat in liquid-vapor phase change offers an order of magnitude enhancement in thermal dissipation efficacy. Owing to their high reliability, passive operation, and effective thermal transport, heat pipes and vapor chambers are extensively used as thermal management devices, which rely on internal porous wicks to passively capillary-feed the working liquid to phase-change surfaces while dissipating heat from localized hot spots. The design, characterization, modeling, and fabrication of these microporous wicks enable the development of heat pipes and vapor chambers as well as the determination of their operational performance limits. In addressing application-driven demands to understand the fundamental hydraulic and heat transfer mechanisms of wick materials, a relatively new class of well-ordered microporous media known as inverse opal is evaluated due to its periodic and three-dimensionally interconnected, permeable pore network. The regularity in the pore packing arrangement

provides the unique opportunity to extract structure-property relations with high repro-
ducibility.

While the attractive characteristics of inverse opals are attributed to their deterministic and
well-ordered structures, their long-range periodicity is often naturally disturbed with defects,
such that these materials are categorized as polycrystalline porous media and are defined
by morphologies with discrete crystalline porous domains that intersect at grain boundaries.
Much like solid-state transport in an atomic polycrystal, hydraulic transport in a polycrys-
talline microporous medium is determined by the summative effects of transport within the
crystalline domains and transport across the grain boundaries. While hydraulic transport
in well-defined geometries can be predicted with relatively high accuracy using numerical
simulations, grain boundaries introduce flow field complexities that are significantly more
challenging to model while potentially having a significant impact on the collective trans-
port characteristics of the porous medium. To elucidate the hydraulic resistance induced by
grain boundaries, a novel combination of fluorescent microscopy and electron microscopy is
employed to visualize capillary-assisted liquid propagation in polycrystalline inverse opals
with high spatial, contrast, and temporal resolutions.

Under extremely high heat fluxes from concentrated hot spots, the operational performance
of two-phase thermal management devices is limited by their boiling heat transfer efficacy.
Utilizing the uniform and controllable features of inverse opals, structure-dependent proper-
ties and optimal heat transfer performance can be determined based on the effective balance
between competing liquid-vapor interactions within the confinement of the porous media.
The surface wettability of inverse opal is investigated in details for its dominant role in
bubble nucleation and departure that influence the heat removal rate and surface dryout.

Chapter 1

Introduction

1.1 Importance of Thermal Management

From the invention of the transistors to the advent of microelectromechanical systems (MEMS) and nanotechnologies, electronics systems continue to increase in their functionalities and performance, while compacting their electrical components into a dense packaging design for portability and lightweight utility. The increasing device operating frequency, clock speed, gate count, duty cycles, and complexity within a footprint constraint generate an aggressive amount of thermal load that can be performance-limiting. The inability to dissipate the unwanted heat can lead to accelerated degradation, thermal shock, and eventually, premature system failure. Such failure mode is the a major source of electronics failure in comparison to other contributing factors, such as dust, humidity, and vibration (Figure 1). [7] By reducing the temperature of electronic systems by 10 °C, the life-span of the associated components can double. To continually develop next-generation electronics and technologies, novel thermal management solutions are needed to keep pace with technical advancements in order to ensure system performance and reliability.
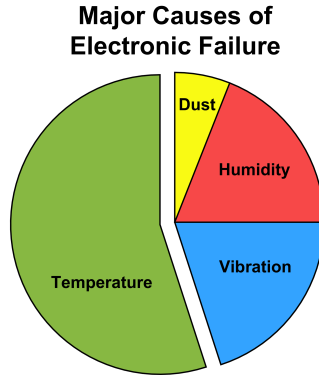
Figure 1.1: Causes of Electronics Failure. Percentage breakdown shows that electronics fail due to thermal mismanagement.

The prominence of electronics usage has become a pervasive part of modern society. Electronics in both the consumers and industrial/military sectors have been increasing in the global market within the past decade (see plotted circles in Figure 1.2a). To meet the thermal management demands of these ever-increasing high-powered electronics, the market for thermal management technologies have also been concatenately growing, closely following the market trends of electronics in their respective industry sectors (see bar graphs in Figure 1.2a). Considering all the technical sectors that thermal management technology encompasses (e.g., computers, renewable energy, telecommunications, light-emitting diodes, medical/office equipment, and automotive), the thermal management industry is projected to continue increasing to $15 billion and $16 billion by 2021 and 2023, respectively (Figure 1.2b). [7] These concatenating trends underscore the interdependency between the growing market for advanced electronics and the desperate demand to dissipate unwanted heat. Through both fundamental and application-based breakthrough in thermal management solutions, future electronics will be given a larger design space to continue to innovate in pushing their performance limits.
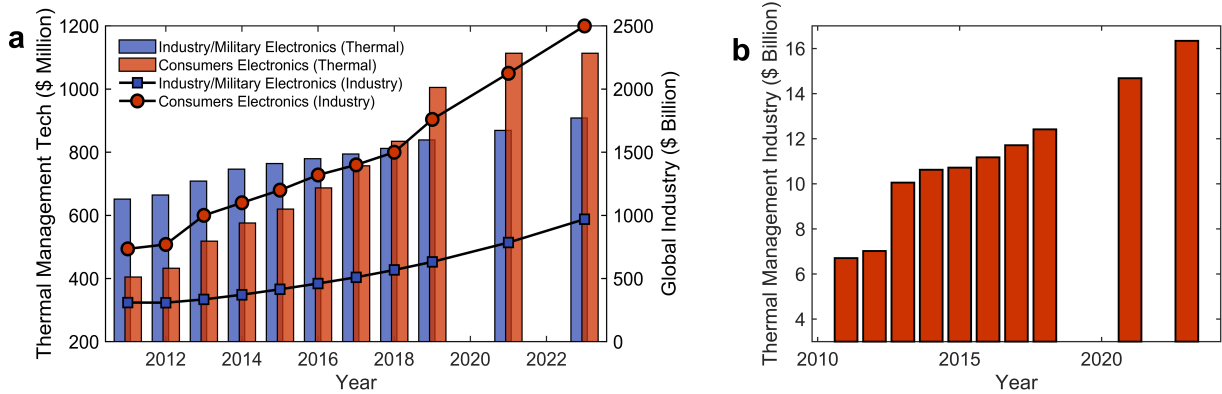
Figure 1.2: The Industry of Thermal Management Technologies. (a) The prominence of thermal management solutions increases with the development of next-generation technologies in the industrial, military, and consumer sectors. (b) The projection of the growing demands for thermal management technologies.

1.2 Heat Pipes and Vapor Chambers

Through the extreme integration and compaction of high power and high frequency electronic devices, nano- and micromaterials have played a critical role in enabling next-generation thermal management technologies. Enormous efforts aim to leverage nanomaterials through advanced microfabrication techniques to reduce the thermal resistance between the device junction and the heat sink at different length scales, which has contributed to the advancement of thermal interface materials, [8–14] integrated circuit cooling with microfluidic heat exchangers [15, 16] and thermal ground planes [17–19]. Among the emerging nanotechnologies used as thermal management hardware in electronics packaging, vapor chambers and heat pipes are becoming increasingly integrated into packaging architectures. The adoption of these passively operated multiphase cooling devices is particularly more efficient in thermal dissipation compared to conventional heat sink-fan configurations, especially within strict spatial confinement requirements. [20–34]

Heat pipes and vapor chambers operate by transporting the working fluid to the evaporating surface through a porous media, passively pumped by capillary pressure. At the evaporator region, evaporation and boiling of the liquid occurs, which absorb the heat through the latent
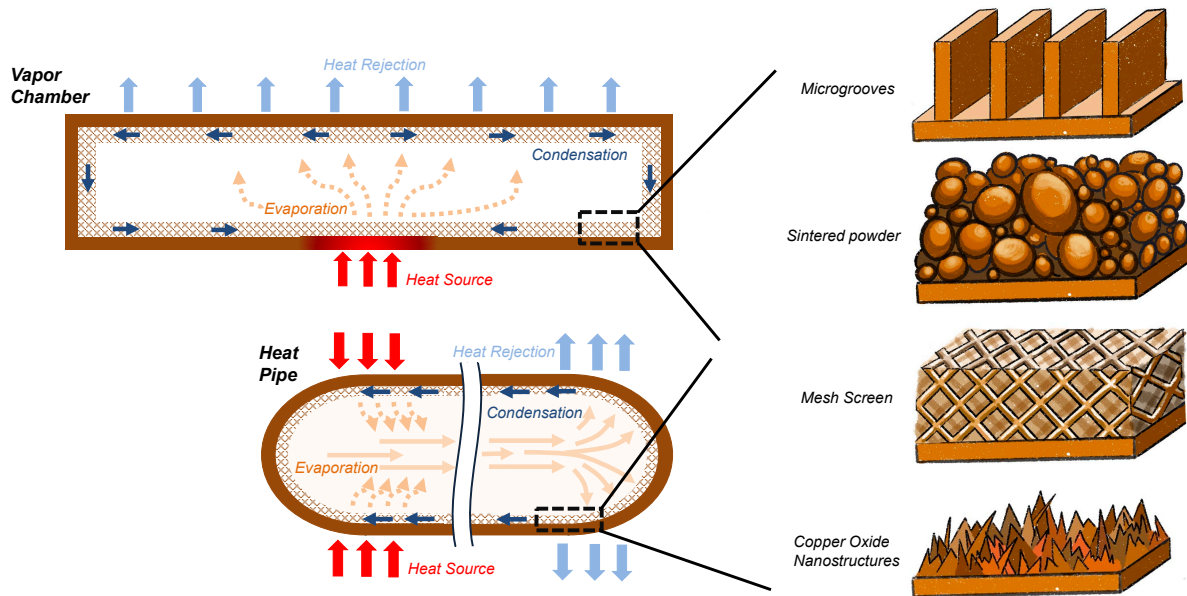
Figure 1.3: Porous Wicks in Heat Pipes and Vapor Chambers. Schematics showing operation of heat pipes and vapor chambers with various common choices of interior wicking media that facilitate capillary pumping and transport thermal energy from heat source to sink.

heat of phase change. The volumetric expansion during phase transition generates an increase in pressure, which forces the vapor toward the condenser region and reject the heat to the surface by condensing back into a liquid, releasing the latent heat. By leveraging the latent heat of phase change, the devices offer orders of magnitude higher in effective heat transfer coefficient in cooling performance in comparison to solid conduction heat spreaders or forced air cooling solutions. While heat pipes and vapor chambers can effectively dissipate heat in a low packaging profile design, the application of either devices varies depending on their desired functionality. For instance, vapor chambers spread thermal energy from localized high-powered hot spots to a larger surface area, where heat is rejected to a solid conduction heat spreader. In contrast, heat pipes transport thermal energy from a low-density power source to another source over a longer working distance.

1.3 Design Parameters of Heat Pipes and Vapor Chambers

In designing the utility of heat pipes or vapor chambers, the operational limiting factor of these thermal management devices significantly depend upon the wicking performance of the porous media that passively regulate the liquid wicking from the condenser to the evaporator. Conventional porous wicks that line the inside of heat pipes and vapor chamber include sintered metal powder, [29, 31, 35–39] wire mesh screens, [40–42] or microgrooves. [43–47] Other developing wick materials in two-phase cooling devices include metallic micropillar arrays, [48, 49] metal or graphite porous foams, [50–53] and 3D printed porous structures [54]. The wicking performance of the porous media is influenced by their generated capillary pressure, which is dependent upon the r_p pore radius

$$\Delta P_{cap} = \frac{2\sigma_l \cos(\theta_{app})}{r_p} \tag{1.1}$$

Where σ_l is the surface tension and θ_{app} is the apparent liquid-solid contact angle. Capillary pressure increases with decreasing pore sizes, which drive the liquid flow. Conversely, permeability K decreases with r_p, inhibiting the ease of flow through the porous media. The relationship between the flow resistance and permeability can be described using Darcy's law in one dimensional flow through a porous media,

$$\frac{dP}{dx} = -\frac{\mu_l \dot{m}_l}{\rho_l A_w K} \tag{1.2}$$

where ρ_l is the liquid density, A_w is the wick cross-sectional area, μ_l is the liquid viscosity, $\dot{m}_l$ is the liquid mass flow rate.

The capillary limit of a heat pipe can be further determined as [48]

$$Q_{max,cap} \simeq 2\left(\frac{\rho_l \sigma h_{fg}}{\mu}\right)\left(\frac{A_w}{L_{eff}}\right)\left(\frac{K}{R_{eff}}\right) \tag{1.3}$$

where Q is the heat transfer capacity, $\rho_l \sigma h_{fg}/\mu$ is the figure of merit of the working fluid, L_{eff} is the effective heat pipe length, and R_{eff} is the effective pore radius which is defined as $R_{eff} = 0.5 d_p \cos^{-1}\theta_{app}$. The ratio K/R_{eff} describes the capillary limit of the wicks and is called the capillary performance parameter. While decreasing pore sizes leads to high capillary pressure, it also decreases the permeability. Therefore, the balance between these two competing effects must be balanced to achieve an optimal K/R_{eff} and thus, an enhanced capillary limit.

The fluid transport performance inside porous media exhibit a trade-off between capillary pressure and flow resistance. Balancing these opposing parameters results in the design space constraint of heat pipe and vapor chamber and therefore, their capillary-driven thermal management performance limits. By elucidating the hydraulic transport behaviors through porous media, optimal hydraulic and thermal performances of heat pipes and vapor chambers can be rationally engineered and designed.

Beside the hydraulic transport limitations in heat pipes, the boiling limit poses another challenge that affect the device's effective thermal conductivity. In the evaporator region where phase transition occurs, the incipience of boiling can cause bubble formation within the porous media, obstructing liquid wicking routes. Continual starvation of liquid to the

evaporator region induces a critical heat flux, such that a vapor blanket coats the boiling surface and results in a surface dryout.

The wicking and boiling performances of porous media examined in prior two-phase cooling studies (i.e., sintered powder and porous foams) typically possess irregular pore distributions with polydispersed feature sizes. [55–60] The lack of highly-ordered and uniform pore packing arrangement limits the accuracy in predictive modeling of liquid flow and heat transfer. The contributing mechanisms of pore sizes on the thermal and hydraulic transport mechanism remain unclear due to the lack of systematic investigation with uniform pore distribution, preventing the derivation of a universal predictive tool for wick flow properties. In the cases of sintered particle coatings, the majority of studies reports the particle sizes without mentioning the actual dimensions of the interstitial cavities. [1, 59–61] This is most salient since particle sizes are not translatable to cavity dimensions. In the cases of highly-porous foam materials, the pore distributions and localized porosities widely vary. [56] Understanding the fundamental hydraulic transport behaviors using highly-ordered monoporous architecture can provide engineering guidance toward modeling and designing high-performance porous wick materials.

In the design of the optimal heat pipes and vapor chambers, both the working fluid properties and material selection are also carefully considered based on the required operating temperature of the device. Common working fluids include dielectric liquid, ammonia, sodium, and liquid metals. For the typical operating temperature of electronics, water has the maximum heat transport rate in heat pipes in the range of 25 to 100 °C. While the high thermal conductivity of metals offers the most effective heat transfer rate, the compatibility of the wicking *and* the structural materials of heat pipes needs to be considered in relation to the working fluid. For water, stainless steel and aluminum are incompatible while copper and nickel are. Therefore, with water being the working fluid in this work, we focus on the hydraulic and vapor transport using copper and nickel porous media as the basis materials.

1.4 Thesis Objectives and Outline

This work aims to ascertain fundamental hydraulic and thermal transport behaviors in mono-porous (i.e., uniform pore size and spatial distribution) wick medium. Recent advancement in microfabrication techniques have led to the creation in a relatively new class of mono-porous architecture, known as inverse opals (IOs), which serve as porous media used in these studies. The structural characteristics of IOs (i.e., porosity, distribution of pore sizes, and structural arrangement) are tunable using microfabrication templating process. IOs typically possess crystalline pore packing at small length scale ($\sim$10 μm); however, uncontrollable defects form between crystalline domains at larger length scale, exhibiting grain boundaries in polycrystalline porous media.

While numerical solutions of IOs's structural permeability for their unit cells can be trivially derived using computational fluid dynamics models, it fails to capture the the effective liquid permeability across the polcrystalline IOs and their linear distribution of boundary defects, which impede and throttle the flow with enormous amount of hydraulic resistances. Elucidating the microscopic hydraulic transport mechanisms across these grain boundaries and defects aims to incite future predictive models for wicking capabilities of this relatively new category of rationally designed and optimized porous media in application of two-phase thermal management devices.

The transfer of heat in heat pipes occurs over a long working distance but is limited by the capillary-driven hydraulic transport performance. Meanwhile, the thermal dissipation from a high heat flux source to larger heat spreading area over a shorter working distance in vapor chambers is limited by the critical heat flux. Evaluating the ebullition cycles and critical heat flux for IOs with various structural characteristics is essential to optimizing the porous architecture for enhanced cooling performance in a low-profile packaging design.

In Chapter 1, the importance of two-phase thermal management devices are highlighted, and an overview of heat pipes and vapor chambers as well as their design functionalities are briefly discussed. Chapter 2 provides fundamental insights into understanding and characterizing engineered porous media for fluid transport. In addition, the current state of manufacturing porous materials with amorphous as well as crystalline characteristics is briefly reviewed. Chapter 3 discusses the microscopic wicking behaviors in the presence of grain boundaries in polycrystalline IOs. Chapter 4 presents the boiling limits and ebullition behaviors of IOs with varying pore sizes and wick thicknesses in order to providing engineering guidance in optimizing the porous structure for high heat flux removal. Chapter 5 concludes the work and presents remarks on proposed future works.

Chapter 2

Understanding Engineered Surfaces and Porous Media

As a wetting liquid wicks through an unsaturated porous medium, the capillary phenomena occur based on the energetic state and physical interaction between the liquid and the structural material as well as the internal pore geometry of the porous architecture. Therefore, not only do both the physical properties of the porous skeleton and the percolating liquid (or gas) contribute to the transport behaviors in the system, but they are also influenced by the interaction between these constituents. These interactions are based on surface phenomena that can be described in terms of surface wettability and morphology of the porous media. By rationally engineering the porous structures and their surfaces with desirable physical properties, we can tune and enhance their functionalities and thus, enlarging the spaces for more application-driven solutions. This chapter reviews fundamental understandings of surface wettability, capillary-assisted hydraulic transport, traditionally amorphous porous media, and the creation of highly-ordered porous structures.
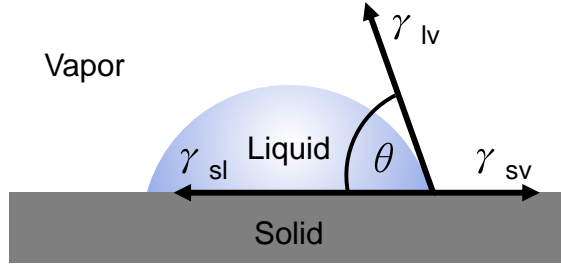
Figure 2.1: Schematic of a Liquid Drop with Denoted Forces from Young's Equation.

2.1 Surface Wettability

2.1.1 Static and Dynamic Wetting States

The dynamics of liquid when in contact with surfaces are often described by their surface wetting characteristics, which vary depending on the surface chemistry and topography as well as the liquid properties. [62–66] On ideal surfaces (i.e., smooth and chemically homogeneous), the interaction between the liquid droplet and the surface represents the minimization of the total energy of the liquid-solid-ambient gas system, described through an apparent contact angle θ_{app} which possess a unique equilibrium value in Young's relation [67]: $\cos \theta_{app}$ $= (\gamma_{sv}$ - $\gamma_{sl})/\gamma_{lv})$, where γ_{sv}, γ_{sl}, and γ_{lv} are the solid/vapor, solid/liquid, and liquid/vapor surface tensions, respectively (Figure 2.1). During static measurements, surfaces with an apparent contact angle $\theta_{app} > 90°$ are considered to be hydrophobic, and superhydrophobic with $\theta_{app} \approx 150°$. Hydrophilic and superhydrophilic surfaces are discerned when $\theta_{app} < 90°$ and $\theta_{app} \approx 0°$, respectively.

However, surfaces are rarely ideal, and understanding both the static and dynamic wetting behaviors on real surfaces that are not atomically smooth and chemically homogeneous can provide new insights for surface engineering and prediction. For instance, on real surfaces, θ_{app} can vary between the range of advancing θ_{adv} and receding contact angles θ_{rec}, which represents the maximum and minimum contact angles, respectively. This hysteresis in con-
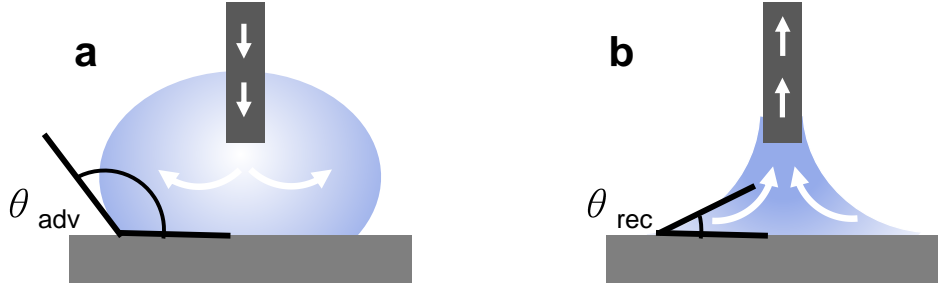
Figure 2.2: Schematic of Dynamic Contact Angle Measurement through Needle Method. A syringe needle is brought into close contact with the surface and slowly dispenses liquid to increase the volume of the drop. The advancing contact angle is measured once the contact line between substrate and drop increases. By retracting the liquid slowly from the surface, the receding contact angle is measured once the contact line withdraws.

tact angles is influenced by the deposition parameters and can be associated with the surface inhomogeneities, caused by contaminants, surface roughness, or time-dependent surface energy changes. Therefore, determining the advancing and receding contact angles can reveal dynamic wetting states where droplets or liquid bridges are in movement.

2.1.2 Common Measurement Techniques

Measuring the apparent contact angle is commonly achieved using static sessile drop method, which utilizes a contact angle goniometer in conjunction with an optical system that captures the profile of the liquid drop on the solid surface. The angle between the liquid-solid and liquid-vapor interfaces denotes the apparent contact angle (Figure 2.1).

To understand the potential contact angle hysteresis on real surfaces, dynamic sessile drop method can be employed. Similar to static sessile drop, the liquid is dispensed onto the surface, but the volume of the drop is slowly increased to achieve the largest possible contact angle without increasing its solid-liquid interfacial area (i.e., θ_{adv}), as shown in Figure 2.2. Conversely, the liquid volume is removed to induce the smallest possible angle (i.e., θ_{rec}). The difference between θ_{adv} and θ_{rec} is the contact angle hysteresis.
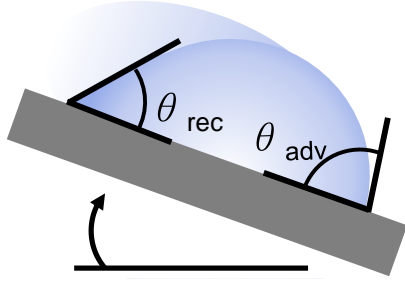
Figure 2.3: Schematic of Dynamic Contact Angle Measurement through Tilting Method. A drop is placed onto the substrate, which subsequently begins to slowly tilt. The advancing and receding contact angles are measured once the drop begins to slide, and the roll-off angle can be determined simultaneously.

Another common approach to measuring the dynamic contact angles derives from determining the droplet's sliding angle. After initially dispensing the drop on a level surface, the surface is then slowly tilted to increase its angle of inclination. While the drop may not move at first, its shape can deform based on its density, volume, and surface tension. Once the inclined surface reaches a particular angle, the drop begins to slide or roll. The contact angle on the left (θ_{rec}) and right (θ_{adv}) side of the drop at the moment of movement describes its dewetting and wetting process, respectively, as illustrated in Figure 2.3. Drops that remain pinned despite the tilting angle reaching 90° exhibit enormous contact angle hysteresis and follow Wenzel wetting behaviors.

The wetting on rough or structured surfaces can often be described using Wenzel or Cassie-Baxter's model. In the Cassie-Baxter state, the liquid bridges between asperities of the rough features while pockets of air remain below (Figure 2.4a). The limited pinning of the liquid to the surface is demonstrated through little to no contact angle hysteresis. Whereas in the Wenzel wetting state, liquid follows the contour of the surface topography and fills in the available cavities (Figure 2.4b). This causes the liquid to exude strong liquid pinning and therefore large contact angle hysteresis. While structured surfaces can exhibit superhydrophobic characteristics, by chemically functionalizing such surface to be hydrophilic, liquid can completely wet the topography by capillary forces through an effect known as hemiwicking. [68, 69]

13
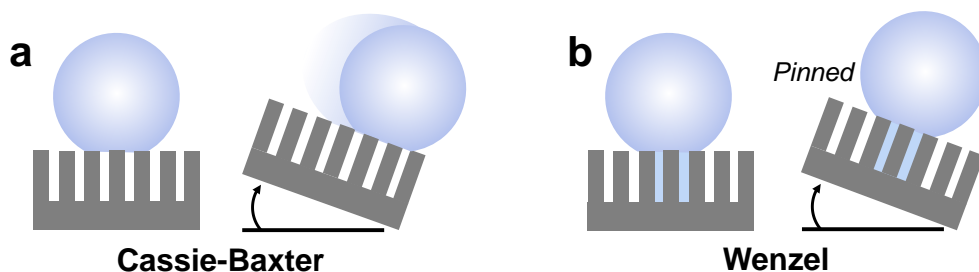
Figure 2.4: Dynamic Wetting States. Hydrophobic droplet contact angle on a textured surface can be exhibited as a (a) Cassie-Baxter or (b) Wenzel state. (a) The hydrophobicity of the surface can cause the droplet to be suspended on top of the surface asperities. At relatively low tilting angles, the limited droplet adherence to the surface allows the droplet to slide with low contact angle hysteresis.(b) For the Wenzel wetting state, the liquid wets the entirety of the surface textures while displaying hydrophobic characteristics. The impingement of the liquid into the textures often pins the droplet from sliding when being tilted, forming a high contact hysteresis.

2.1.3 Effects of Droplet Size

When measuring the liquid contact angle, the droplet volume significantly influences the contact angle results. In the case of static sessile droplet measurement, the liquid is slowly dispensed from a hydrophobic capillary tip. With the droplet being significantly below the capillary length scale, the droplet remains in a nearly spherical shape because gravity can be neglected while capillary forces dominate. When the drop comes in contact with a hydrophobic surface, it rests on the solid. For nano- and microscale drops, the droplet maintains its nearly spherical shape and exhibit higher contact angles than its macroscale counterpart. [70] For larger volumes of droplets (between 1 and 100 μL), the droplet shape becomes distorted by gravity, while contact angles are shown to remain consistent for the large droplet sizes. [71] When surface tilting is used to determine the dynamic contact angle of the drop, larger droplet volume will also experience more gravitational force along the tilted direction, causing the drop to slide at lower angles of inclination and therefore influence the advancing and receding contact angles.

The effect of droplet volume on contact angle measurements can be minimized by maintaining a consistent volume among all experiments performed for comparability reasons. Therefore, unless noted otherwise, the contact angle measurements presented in this work are conducted using deionized water with a liquid volume of ~ 15 nL. In addition, the contact angle profile of the drop is determined using half-angle method, which is appropriate for microscale drop that retains its spherical shape (due to minimal gravitational effect).

2.2 Hydraulic Transport across Textured Surfaces and through Porous Media

2.2.1 Governing Parameters

Mass transport through capillary-assisted wicking is considered one of the most significant phenomena in surface sciences and engineering that was first classically investigated around 1700 before being developed into fundamental principles by Young and Laplace in 1805. [72] In a classical demonstration of one-dimensional viscous imbibition, a capillary cylindrical tube (Figure 2.5) with a known radius b comes into contact with a reservoir of a wetting liquid (of surface tension γ and dynamic viscosity μ). Imbibition occurs immediately within the tube to minimize energy, and the dynamic capillary rise can be described using Darcy's equation by balancing the viscous friction with the pressure gradient that drives the fluid propagation. [62]

$$\frac{\mu u}{K} = -\frac{\partial p}{\partial h} \tag{2.1}$$
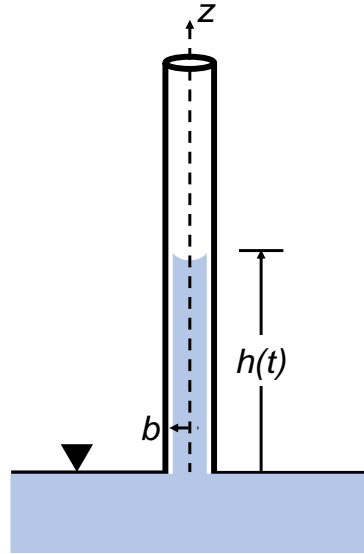
Figure 2.5: Capillary Tube. The imbibition of liquid inside a capillary tube once in contact with the reservoir of the wetting liquid. The meniscus position (or propagated height) is indicated by h at time t. The capillary tube possesses a radius of b.

where $u(h, t)$ is the average liquid rise velocity as a function of propagation height and time, K is the permeability of the tube ($K = b^2/8$). The pressure gradient derived from the Laplace pressure at the meniscus over the length can be expressed as

$$l(\frac{\partial p}{\partial h} = -\frac{2\gamma \cos \theta}{bl})$$ (2.2)

where θ is the droplet contact angle on the solid.

By quantifying the liquid rise velocity as $u = \mathrm{d}l/\mathrm{d}t$, Equation 2.1 becomes the classical Washburn law, which states that the propagation height (or meniscus position in a capillary tube) increases as the square root of time. [73, 74]

$$h \propto t^{1/2} \tag{2.3}$$

For centimetric samples, the effect of gravity can be neglected in the force analysis of liquid propagation. The dynamics expressed in Washburn law have also shown robustness in describing liquid spreading on rough and micropatterned surfaces as well as wicking in homogeneous porous media (e.g., paper, fabric, and sand bed).

For engineered surfaces with micropatterns or porous coatings, the wetting liquid spontaneously wicks into the capillary spaces similar to the imbibition event with the capillary tube. The liquid film propagates across the patterned surfaces, matching the film thickness to the height of the engineered features in order to minimize the surface energy.

Aside from mass transport through wicking, textured surfaces (e.g., silicon post arrays) can also be used to speed up liquid spreading on a large scale. For instance, Ishino et. al. [72] demonstrated that a millimeter-scale droplet with a viscosity similar to that of water requires 10^6 s (approximately 10 days) to spread by 2 cm on a homogeneous surface. Meanwhile, dropcasting a similar droplet on a surface decorated with micropillars induces the liquid film to propagate the same distance within 10 s.

Wicking dynamics can be predicted based on the internal geometry of the structured surfaces or porous media. With capillary force scaling inversely with pore diameter while viscous resistance scaling inversely with the square of pore diameter, modulating the cavity dimensions yield different wicking performances. In addition, balancing the capillary force and viscous

17

resistance results in a net capillary performance denoted as permeability, which describes the ability of a porous medium to allow fluids to pass through and is highly dependent upon the structure porosity. [75]

In addition to the geometric architecture of porous media playing a role in determining the mass transport performance, the surface wettability remains a significant factor in influencing the capillary-assisted permeation through the structure. For passive wicking to initiate, the surface of the porous media must be hydrophilic to facilitate complete wetting induced by capillary forces in two dimensions. [68] The degree of hydrophilicity has also been shown to affect the capillary performance during wicking events. [76]

2.2.2 Measurement of Capillarity

A common approach to measuring the capillary performance of a wick is to perform a capillary rate-of-rise experiment inside an enclosed environmental chamber to decrease evaporation effect.[9, 76–79]. A hydrophilic porous medium is slowly lowered to come in contact with a liquid reservoir. A capillary pressure gradient immediately causes the liquid to wick through the pores. The propagating liquid front is often recorded using imaging techniques, and the capillary performance (K/R_{eff}) is estimated from the measured height of the wicking front as a function of time (rate of liquid propagation), using the following equation [73]

$$h^2 = \frac{2\sigma}{\varphi\mu}\frac{K}{R_{eff}}t \tag{2.4}$$

2.3 Engineering Design Space of Porous Media

The effective physical adsorption and fluid transport properties in porous media directly depend on the internal pore geometry. By modifying the pore geometry, not only the structural characteristics (e.g., porosity, specific surface area, and tortuosity) are changed, but the behaviors of the fluid and movements of species through the media can be influenced. Since the majority of applications rely on efficient mass transport for high-throughput, high-speed, and high durability, it becomes essential to understand relevant transport properties (and limitations) in order to engineer and optimize the performance of porous media.

2.3.1 Porous Metals

Naturally occurring porous structures can be found in but are not limited to biological materials, such as bones, wood, plant leaves, and coral. The internal structures of these materials have evolved using design principles from nature to optimize their transport properties. [80–84] By engineering and designing artificial porous media, relatively new classes of functional materials can be created to combine certain properties from both the porous structures and their derivative bulk (solid) materials. For instance, a classification of engineered porous media that has garnered significant interest over the past three decades is porous metals owing to their attractive bulk properties (heat capacity, malleability, ductility, thermal/electrical conductivity) and porous capabilities (permeability, reduced weight, high mechanical strength at low density, and high specific surface area). Leveraging the desirable characteristics, the properties of the porous metals can be rationally designed to address numerous engineering and scientific applications. This is evident when their high active surfaces are used surface interactions, such as phase separation, gas mixture separation, or ion exchange and capture, and the conductivity of porous metals is used for thermal, electrical, and fluidic

19

transport performance breakthroughs, such as in electrode-electrolyte interfaces in batteries to capillary-fed heat pipes and vapor chambers. [40, 85–92]

The nano- and microscopic structural characteristics of metallic porous structures can be tuned through common manufacturing techniques, such as powder sintering and metal deposition through atomic deposition or electrodeposition. [31, 35, 63, 93, 94] However, some of these manufacturing techniques often produce stochastic pore characteristics with no deliberate designed morphologies. While the percolating pore network may be continuous, their permeable pathways are tortuous and foam-like. The disordered pore arrangement and limited range of accessible volume fraction reduce the effective electrical, thermal, and mass transport capability of the materials. [95–97] Conversely, porous materials with deterministically designed architectures promise significant enhancement as well as the opportunity for optimization in functional performance. The wealth of available engineered porous media provides ranges of structures that have varying degrees of heterogeneity, regularity, and periodicity, and the attributes of these amorphous and highly-ordered porous structures are briefly reviewed in the following subsections.

2.3.2   Amorphous Porous Structures

Conventional manufacturing techniques for porous media such as emulsification, [98, 99], particle sintering, [100] layer-by-layer deposition, [101] electrodeposition, [102] and electrospinning [103] tend to produce disordered morphologies with minimal long-range order. This can exemplify by considering a bed of packed spheres; countless sphere jamming configurations can exist based on the degree of freedom in the system. For a bed of monodisperse spheres, this bed porosity can range between approximately 36% and 46%. Higher bed porosity can be realized by arranging the spheres in a more crystalline packing formation or by using polydisperse spheres. [104] These amorphous porosities are generally approximated

using statistical descriptors of polydisperse structural features and can vary widely between samplings as well as localized regions *within* each sample. The inaccuracy and variances in describing the porous medium and its constituting features create challenges in modeling transport behaviors and establish the rigorous structure-property relations necessary for material optimization. This significantly reduces the accessible engineering design space for porous media and limits the accuracy and utility of predictive transport models.

While the advancement of computer-generated models (e.g. through tomography) can provide representative glimpses to the transport properties for the given reconstructed structure, the heterogeneity in the structure characteristics (e.g., localized porosity, pore size distribution, and pore network arrangement) can limit the capability to precisely tune the holistic morphology for optimized effective performance with high reproducibility. The reproducibility of this reconstruction-modeling technique can be improved only when the random sphere packing densities approach the random-close packing limit. [104] Only then can the effects of porosity-scaling on transport parameters (e.g., hydraulic permeability, effective diffusion, and hydrodynamic dispersion) be studied and predicted with improved accuracy. [105] The random pore networks also pose severe limitations to their performance efficiency due to their intrinsic tortuous permeable pathways and high mass transport resistance.

Despite the numerous drawbacks and limitations associated with amorphous porous structures, they remain the most commonly used materials in adsorption- and transport-based applications. This can be attributed to their low cost and convenience in manufacturing combined with decades of expansive research activities into their hydrodynamic transport properties. However, in order to realize the high performance and transport efficiency promised by well-defined porous media, we are impelled to develop and utilize advanced fabrication techniques to create porous architectures with deliberate designs and evaluate their theoretical and experimental structure-transport relationships with high reproducibility and efficacy.

2.3.3 Creating Ordered Porous Structures

With advancements in manufacturing techniques beyond traditional microfabrication, processes such as self-assembly, [106–109] stereolithography, [110–113] selective laser sintering, [114, 115] and advanced additive manufacturing [116, 117] can create porous architectures with complex and crystalline-arranged internal geometries. A crystalline porous medium is a material with an ordered morphology defined by a lattice of repeating porous unit cells. The intrinsic pore shape and size of the base unit cell can be systematically engineered to achieve predictable and tunable transport properties in the macroscale crystalline porous superstructure. This level of precise structural definition is often inaccessible to conventional amorphous porous media with a stochastic distribution of features, dimensions, and fluid pathways.

These well-ordered porous structures can often be categorized as 2.5D (e.g., micropillar or structural arrays) or 3D porous architecture (e.g., microscale woodpiles) based on the dimensionality of possible structural modulation (i.e., in the x-, y-, and z-directions). [113] The spatial modulation of the features is limited based on the implemented manufacturing technique. For instance, the classic lithography process (while can produce high-resolution features) cannot create complex structures beyond those with high-aspect-ratio two-dimensional characteristics. By transitioning from stochastic to deterministic porous architectures, crystalline porous media can be rationally designed to achieve significantly higher rates of thermal and electrical conduction, capillary and forced mass flow, interfacial exchange, and liquid-vapor heat transfer compared to conventional porous media.

2.3.4 Inverse Opals as a Class of Polycrystalline Porous Media

Among the classification of three-dimensionally ordered pore-matrix architecture, inverse opals (IOs) remain widely studied porous materials, whose thin films composed of a lat-
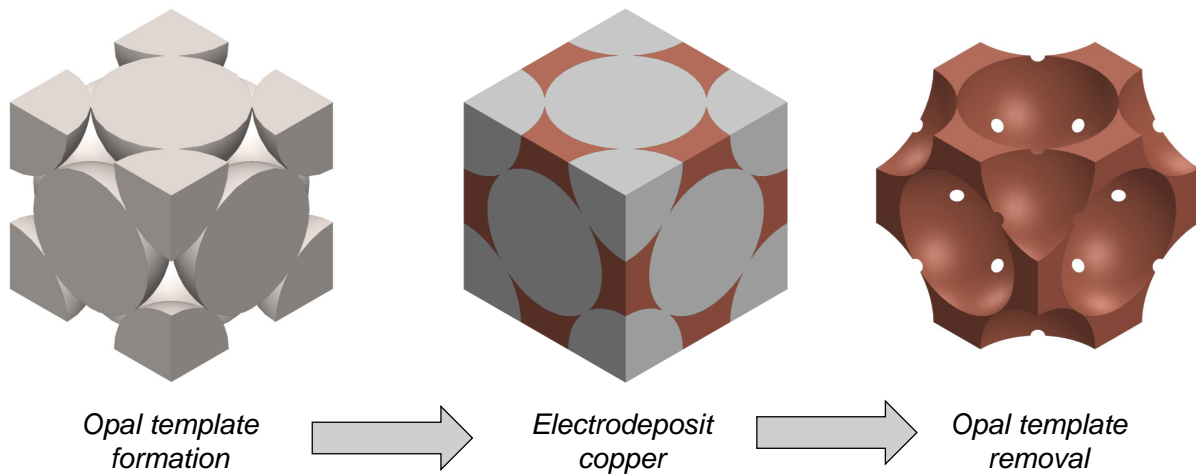
Figure 2.6: Creation of Inverse Opals. Representative process for creating copper inverse opals.

tice of close-packed, interconnected spherical voids that create a continuous, fluid-permeable network of pores. [118–125] The combination of pore periodicity, interconnectivity, and enormous surface areas of IOs have been used for enhanced heat and mass transport in applications, including catalytic surfaces, [126, 127] membranes, [98, 128] supercapacitors, [90] sensors, [129] battery electrodes, [89, 130] sensors [131] and microfluidic heat exchangers [132–135]. Due to the unit cell-based pore packing arrangement of IOs, their fluid transport physics has been modeled through computational fluid dynamics (CFD) or finite element method (FEM). [63, 75, 136–138] The microscale crystalline arrangement of pores and well-ordered structural features are visually apparent when examined under white light, reflecting brilliant monochromatic colors, as shown in the optical images of Figure 2.7a. From microscopic inspection of the IOs, the spherical pores are packed at well-defined points in a crystalline lattice (Figure 2.7b).

Inverse opals are created by template-assisted deposition, where the structural materials are deposited between a 3D colloidal crystal (referred to as an "opal") that serves as a sacrificial template (Figure 2.6). [119, 139–144] The opal is synthesized by self-assembly of suspended nanospheres ($\sim 10^{-1}$ to 10^{-1} μm) to form a close-packed, periodic arrange-

23

ment of monodisperse nanospheres. Once the sacrificial opal template is removed, the IO reveals a continuous scaffold with periodic arrangement of spherical pores where the spheres once remained and interconnected windows between pores (denoted as the "via") where the sphere-to-sphere contact area previously existed (Figure 2.8). The structural characteristics of IOs can be widely tuned through the self-assembly parameters. For instance, the porosity can be modulated with the opal template (e.g., by sintering the opal) [142, 145] or through post-fabrication materials processing (e.g., electroetching). [63] The pore diameters can be controlled by dictating the templated sphere diameters, which can range from 100 nm to several microns; The self-assembly of opals can be achieved through vertical deposition, [86, 145–148] sedimentation, [149] flow cells, [150] and spin coating [151]. Various materials have been used as the scaffolds in IOs, including metals, [146, 152–155] oxides, [52, 120, 126, 156] and polymers, [157, 158] which can be deposited through electrodeposition, [75, 146] electroless deposition, [159] chemical vapor deposition, [160] and capillary infiltration. [129] The thickness of the resulting IO and opal template can be well controlled up to 100 μm and cover an area as large as a 4-in. silicon wafer. [148]

Despite the opal's natural tendency to self-arrange into crystalline formation, [161] long-range periodicity ($>10^2$ periods) is often disturbed by the introduction of nanoscopic defects and perturbations during the fabrication process. These defects include nonuniform intrinsic characteristics (e.g. sphere polydispersity) and extrinsic conditions (e.g. solvent evaporation rate), which facilitate the formation of macroscopic defects between ordered domains and often manifest as propagated cracks in the crystal. [162] By backfilling these cracks in the opal templates with a structural material (i.e., polymer or metal) during inversion, these cracks become solid barriers.

While there have been tremendous efforts to approach defect-free crystallinity (e.g., the formation of single-crystal opal through evaporative self-assembly and the subsequent inverse opal microstructure after structural material infiltration) [147, 148, 163–166], most

24
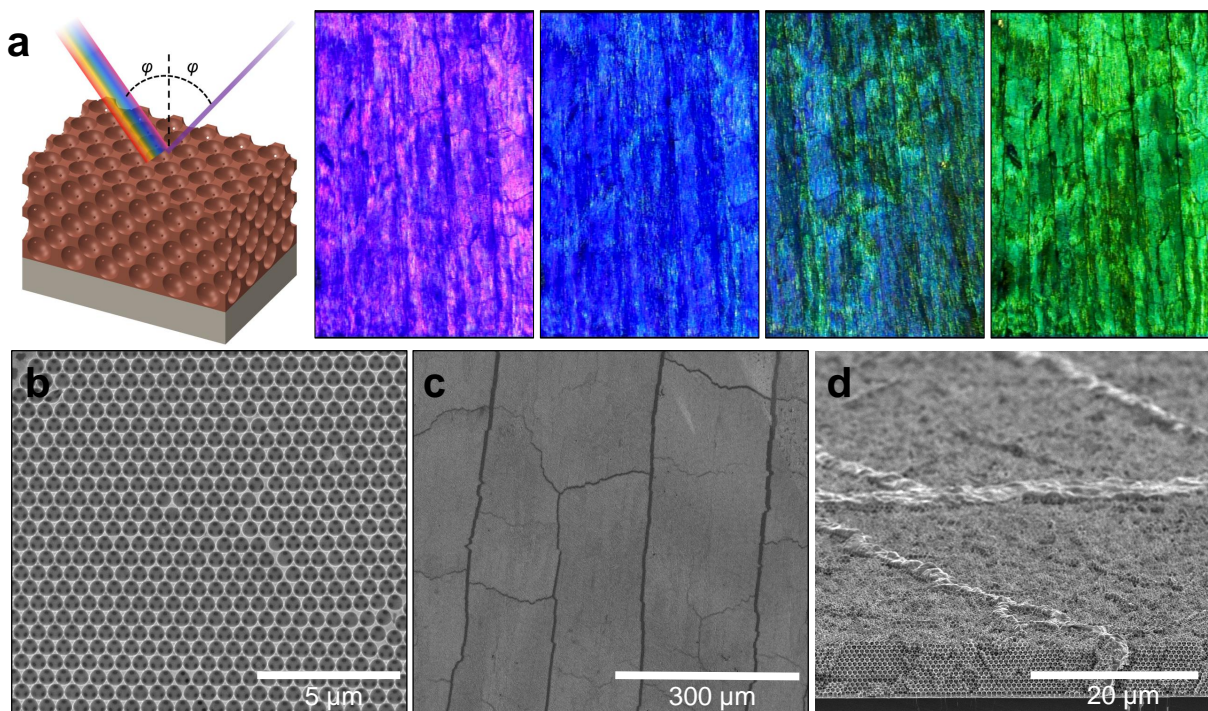
Figure 2.7: Inverse Opals as Porous Polycrystals. (a) The crystalline-arrangement of pores and periodic structural features allows IOs to reflect brilliant monochromatic colors under white light due to the pore-size-dependent and angle-dependent Bragg diffraction of visible light. (b) Top-view SEM image of IOs showcases the uniformity and periodicity of the media; (c) top overview and (d) angled cross-sectional SEM images reveal polycrystalline characteristics with boundary-like barriers separating porous crystal domains.

engineered porous media with long-range order contain a nonzero defect density due to nanoscopic perturbations, variance, and imperfections in the fabrication process. [162] These materials are categorized as polycrystalline porous media and are defined by morphologies with discrete domains of porous crystallinity, or "grains", that intersect at "grain boundaries" (see Figure 2.7c,d and Figure 2.8). [9, 146]

Much like solid-state transport in an atomic polycrystal, hydraulic transport in a polycrystalline microporous medium is determined by the summative effects of transport within the
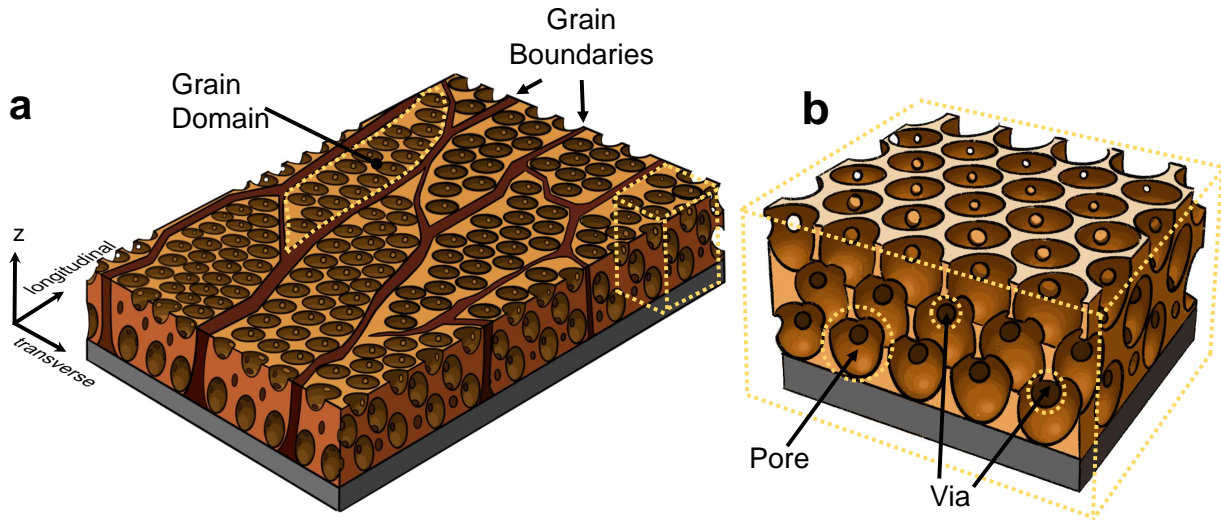
Figure 2.8: Polycrystalline Inverse Opal, an Example of Polycrystalline Porous Media. (a) Illustration of inverse opals (IOs) with naturally occurring boundary barriers separating (b) crystalline domains of uniform spherical pores, interconnected in a three-dimensional lattice superstructure by adjacent windows (denoted as "via").

crystalline domains and transport across the grain boundaries. While hydraulic transport in well-defined geometries can be predicted with relatively high accuracy using numerical simulations, [75, 136–138, 145] grain boundaries introduce flow field complexities that are significantly more challenging to model while potentially having a significant impact on the collective transport characteristics of the porous medium.

2.4 Summary

Capillary infiltration of microporous media leverages the enormous surface area for enhanced solid-fluid interactions in interfacial transport applications such as separation, catalysis, and heat exchanger. While significant efforts have contributed to the understanding of fluid behavior in amorphous or 2.5D ordered porous structures (e.g., microchannels or micropillar arrays), undergoing investigation in the hydraulic transport in three-dimensionally or-

dered microporous network media is still limited. Crystalline-ordered porous media created through self-assembly templating process may prove superior alternative test material, but such structures often exhibit naturally forming defects such as grain boundaries that separate domains of crystalline pore domains. The grain boundaries in the polycrystalline porous media act as impermeable walls that slow and often inhibits hydraulic transport. Despite the presence of grain boundaries as hydraulic resistance in the porous media, previous studies observed that the propagated liquid often overcomes such obstructions through the presence of adjacent grain domains or after an elapsed amount of time. [75, 145] Similar to energy transport in polycrystalline solid materials at grain boundaries, the fundamental physics of hydraulic transport across grain boundaries in polycrystalline porous material need to be further understood for optimal wicking performance through defect-based microstructure.

Chapter 3

Microhydrodynamic Transport in Polycrystalline Porous Media

3.1 Introduction

In previous studies, grain boundaries are attributed to the dominant hydraulic resistance in polycrystalline inverse opals. [9, 145, 155] These grain boundaries reduce the capillary performance parameter by an order of magnitude due to the hydraulic resistance of the structural defects, [9] suggesting that the engineering advantages of a carefully designed porous architecture can be overwhelmed by the presence of defects in the fabricated material. While grain boundaries in polycrystalline porous media impede capillary flow, the propagating liquid front is observed to ultimately overcome these obstructions such that the boundaries can be treated as hydraulic resistors connecting Darcian regions of high permeability. For example, the liquid front propagates across the crystalline grains of porous media and momentarily pins at each grain boundary before the adjacent capillary-filled domains enable the liquid front to overcome the boundary resistance. In other cases, the liquid front remains
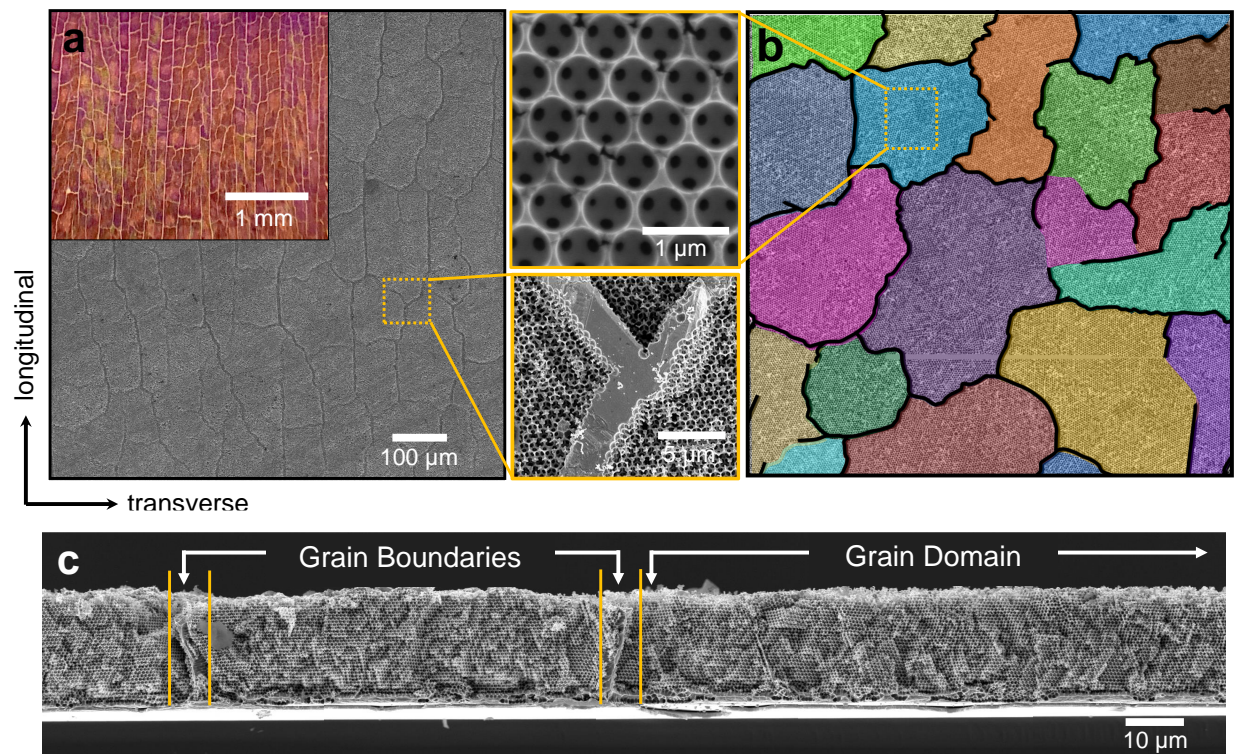
Figure 3.1: Copper Inverse Opal as a Porous Medium Exhibiting Polycrystalline Characteristics. (a,b) SEM stitched images of IOs from plan view, displaying grain boundaries and regularity of pore arrangement. The polycrystalline nature of copper IOs can be optically observed in the inset of (a). (b) The false color overlay indicates the polycrystallinity of IOs. (c) Cross-sectional stitched SEM images shows that the grain boundaries fully extend along the thickness of the IO, demarcating each IO domain.

pinned behind the grain boundary but is able to overcome the barrier after a certain amount of time has elapsed, wicking in a discretized stop-and-go manner across multiple polycrystalline porous domains. To understand these microscopic liquid propagation behaviors in polycrystalline porous media, the capillary driving forces within the intrinsic porous crystals must be dissociated from the effects of the grain boundaries. While we explore these effects using inverse opals as a model porous medium, it is expected that the same fundamental transport physics and interpretations would apply to other periodic porous media for capillary flow.
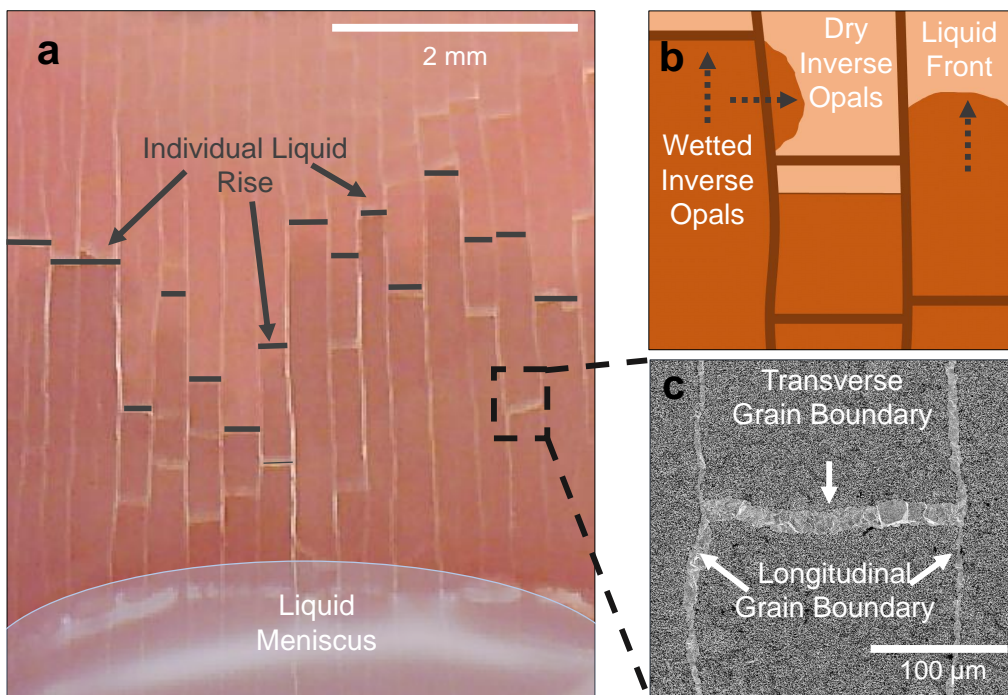
Figure 3.2: Microhydrodynamic Transport in Polycrystalline Copper Inverse Opals Showing Individual Grain Domains and Grain Boundaries. A still photo of a vertically placed copper IO wicking up the liquid from a reservoir. Due to grain boundary defects, propagated height through each grain column varies across the width of the sample. (b) The illustration of individual grain domains and grain boundaries, demonstrating that the wicked liquid can transverse around the micro-obstruction defects. (c) Microscopic image showing individual crystalline domains separated by a set of transverse and longitudinal grain boundaries.

Historically, to examine the nature of liquid propagation through porous media, research groups have utilized conventional stereomicroscopy [9, 78, 167] or high-speed imaging, [49]
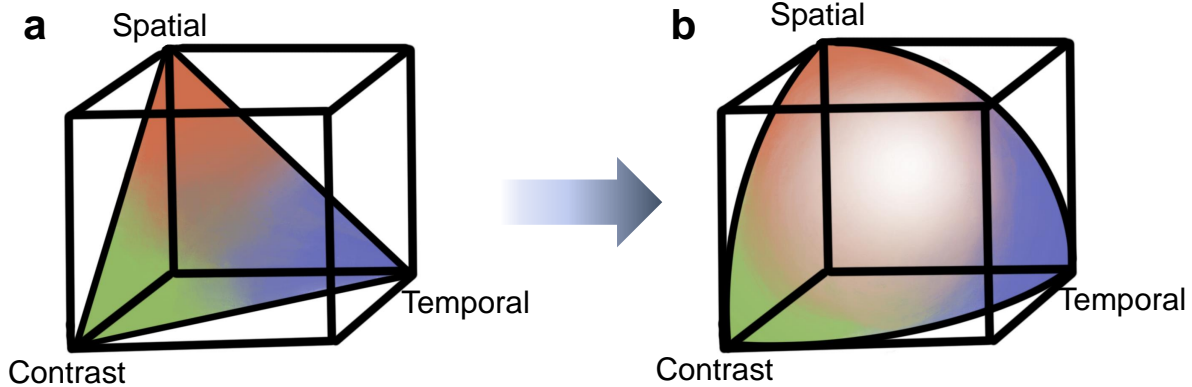
Figure 3.3: Triad of Critical Resolutions Required for Observing Microscopic Transport. (a) In typical stereomicroscope or high-speed imaging, only two of the three resolution criteria are met. (b) In fluorescence microscopy, all three criteria can be optimized and exploited.

which provide high-spatial and high-temporal resolutions needed to observe transport through opened 2.5-dimensional structures (e.g., microchannels, micropillar arrays, nanowire forests, or nanostructured surfaces) [49, 167, 168] or transparent enclosed channels (e.g., glass bead packing or transparent polymer porous structures). [169–171] However, the complex liquid flow field through three-dimensional network-based architectures also requires strong spatial contrasts to discern the transition from liquid saturated-to-unsaturated regions, which are not readily available with traditional optical microscopy. To visualize the liquid saturation dynamics inside complex heterogeneous pore spaces with high spatial resolution and stark fluid-phase contrasts, some have employed X-ray microtomography. [172–175]

However, each tomogram is reconstructed from hundreds of projections, which requires a total acquisition time in the range of tens of seconds, and thus are temporally limited in capturing the dynamic fluid displacements occurring in real-time. The drawbacks of each visualization technique utilized thus far can provide incomplete descriptors of relevant mass transport behaviors at the microscopic level (spatial resolution) with rapid dynamic displacement (temporal resolution) of fluid and air (contrast resolution) in complex microporous

architectures (Figure 3.3a). In the field of biology and biomedicine sciences, fluorescence microscopy has become an essential tool in detecting cells and nanoscopic cellular components with high degree of specificity and contrast intensity and the temporal resolution of traditional microscopy (Figure 3.3b). The high spatial-contrast fidelity of fluorescence microscopy enhances visualization of the wetting behavior dynamics in three-dimensional porous media. The luminescent intensity of the fluorescing fluid provides insights into the degree of fluid saturation within the three-dimensionally microporous networks. Rather than tracking the optical changes induced by the wetting of the fluid, we track the spatial-temporal signature of fluorophore markers contained in the liquid, foregoing the need to resolve the subtle optical changes induced by the carrier fluid. By leveraging the high spatio-temporal resolution of the instrument as well as the strong spatial-contrast of the fluorescent wetting fluid, the evolution of liquid propagation front through capillary saturation can be precisely distinguished and tracked. We then correlate the two-dimensional liquid propagation profile to the microstructural map of the polycrystalline inverse opal to elucidate the underlying physics of defect-limited transport through polycrystalline porous media.

This chapter presents fundamental physics governing the liquid propagation in polycrystalline inverse opals through capillary-assisted transport. The periodic architectural arrangement and homogeneous structural characteristics of each crystal domain is modeled using established structure-property relations. Using high-fidelity fluorescence microscopy, we demonstrate and quantify the impact of grain boundaries on the rate and directionality of capillary-driven liquid flow, both of which are influenced by the characteristics, density, and orientation of the grains and grain boundaries.
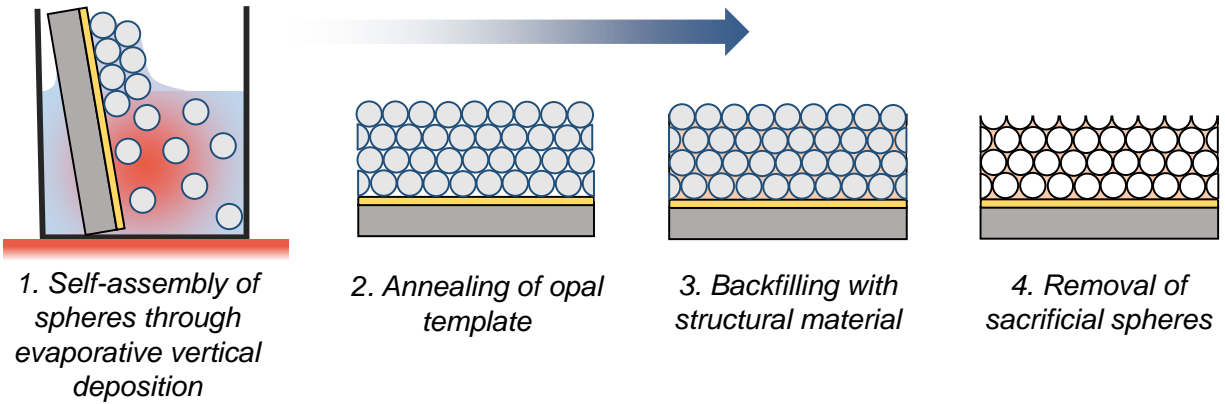
Figure 3.4: Schematics of Inverse Opal Fabrication. Suspension of nanospheres self-assemble onto the hydrophilic vertical substrate to form an opal. After annealing the opal template, a structural material fills into void spaces between spheres and subsequent removal of the template reveals an inverse opal scaffold.

3.2 Experimental Methods

3.2.1 Copper Inverse Opal Fabrication

Copper-based inverse opals IOs are fabricated using a combination of self-assembly of monodisperse polystyrene microspheres to form an opal template, electrodeposition of copper between the void volumes of the opal, and subsequent selective removal of the template, as highlighted in Figure 3.4. [9, 133, 146] A gold-coated silicon substrate is rendered hydrophilic through submersion in a 1mM aqueous solution of sodium 3-mercapto-1-propanesulfonate (3-MPS) for a minimum of 24 hr. The substrate is then near-vertically submerged into a well of the colloidal suspension of monodispersed polystyrene spheres (600 nm sphere diameter, 0.6%w concentration, Thermo Fisher). The thin liquid meniscus on the hydrophilic substrate pulls polystyrene spheres toward the liquid-vapor-solid interface to self-assemble into crystalline arrangement as the solvent evaporates. A base heating of $\sim$55 °C promotes gentle convective mixing and prevents sphere sedimentation. The resulting opal template is annealed in an

oven (Lab-Line) at 97 $\pm$ 0.5 °C for 2 hr to increase sphere-to-sphere contact area. Copper fills the empty spaces between spheres as the structural material through electrodeposition, using an aqueous electrolyte solution of 0.5 M $CuSO_4$ + 0.1 M H_2SO_4. A bulk copper electrode, an opal-covered substrate, and Ag/AgCl serve as the counter, working, and reference electrode, respectively. An effective current density of $\sim$7.5 mA/cm^2 (i.e., a constant current of 0.875 mA over a total conductive layer area of 0.115 cm^2) is applied in a galvonstatic mode (SP-300, Bio-Logic). The copper-polystyrene composite immerses in two sequential baths of tetrahydrofuran during which the polystyrene opal template is dissolved. This reveals a copper inverted scaffold of the original opal matrix and template cracks become wall-like boundaries. The copper IO is further functionalized in 3-MPS for 24 h to render the structure hydrophilic for capillary wicking. [9]

3.2.2   Varying Domain Anisotropy in Polycrystalline Inverse Opals

The experimental parameters employed in IO preparation process directly influence the final IO morphologies and thus can be systematically tuned to vary their physical construction and explore their associated transport properties. In this study, the copper IO superstructures possess uniform spherical pore diameters of 0.6 μm are periodically and fully interconnected by adjacent windows (via); from which, we fabricate five sets of IOs with varying structural characteristics (i.e., degrees in polycrystallinity, porous domain anisotropy, and porosities) by exploiting the self-assembly of the microspheres during the templating process. Table 3.1 summarizes the characteristics of each sample, and the following is the variation in the preparation process associated with each sample: Sample 1) fabricated using the prescribed conditions above; Sample 2) extended the annealing time to 3 hr; Sample 3) increased the base heating temperature to 80 °C; Sample 4) instead of using the vertical deposition technique described above, the colloidal suspension (with higher nanosphere concentration of 5%w) was dropcastted onto a substrate heated at 80 °C, which causes rapid self-assembly

Sample	Crystallinity	Domain	Porosity (%)
1	Polycrystalline	Anisotropic	Low (78.0 ± 5.8)
2			High (90.9 ± 2.4)
3		Elongated	Low (80.3 ± 3.2)
4		Isotropic	Low (79.0 ± 6.3)
5	Amorphous	Amorphous	52.7 ± 8.7

Table 3.1: Inverse opal samples and their associated characteristics used in the microscopic wicking measurements.

through sphere sedimentation [176]; Sample 5) dropcast 5%w colloidal suspension on an unheated substrate (room temperature).

3.2.3   Structural and Surface Characterization

We characterize the structure regularity, grain boundary, and domain characteristics of the copper IOs with scanning electron microscope (SEM, FEI Quanta 3D). Stitching high-resolution top-view SEM images of the sample provides a map that can be correlated with the fluorescent map (during capillary saturation). Figure 3.5 displays the stitched SEM images, and the outlines of grain boundaries highlight the layout of defect and grain domains. Cross-sectional SEM imaging confirms that the IO thickness is approximately 15 μm for all samples (Figure 3.1). We assume the self-assembled sphere size is equal to the pore diameter, which we corroborate by measuring the pore diameter using high-resolution SEM images from at least 150 measurements; we also measure the diameter of the interconnected windows (via) between pores. We then compute the porosity which, for a face-centered cubic (FCC) IO, is uniquely defined by the relation: $\phi = 0.5833(d_{via}/d_{pore}) + 0.6633$, where d_{via} and d_{pore} are the diameter of the interconnected windows ("via") and the pores, respectively. [63]. The resulting porosities are presented in Table 3.1. See Figure 3.6 for detailed statistical results. We measure the widths of grain boundaries incrementally along their lengths from plan view SEM images (see Figure 3.7) as well as grain domain areas (see Figure 3.8) to provide structural descriptors that are correlated to the transport properties. The surface
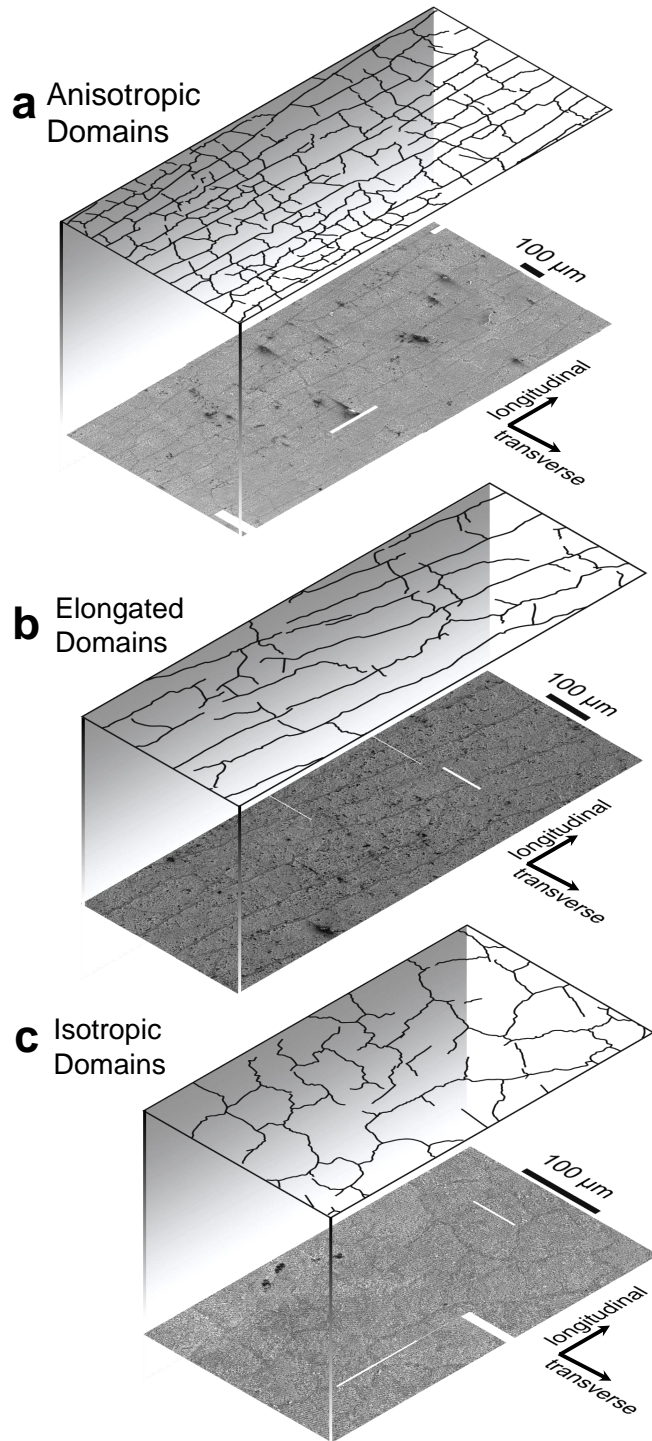
Figure 3.5: Grain Boundary Projection from Inverse Opals. Schematic outlines of grain boundaries projected from plan view SEM image stitching of IOs with (c) anisotropic, (d) elongated, and (e) isotropic domains.

36
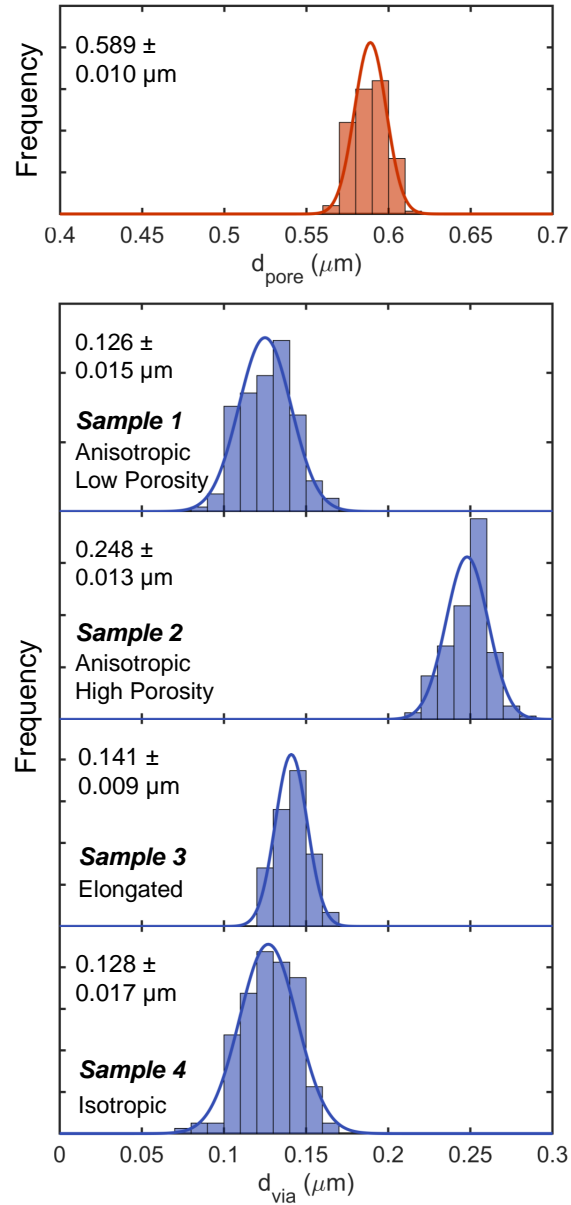
Figure 3.6: Statistical Distribution of Pore and Via Diameters. Pore diameter (orange bar graph) and via diameter (blue bar graphs) distribution collected from at least 100 measurements for Sample 1 through 4.
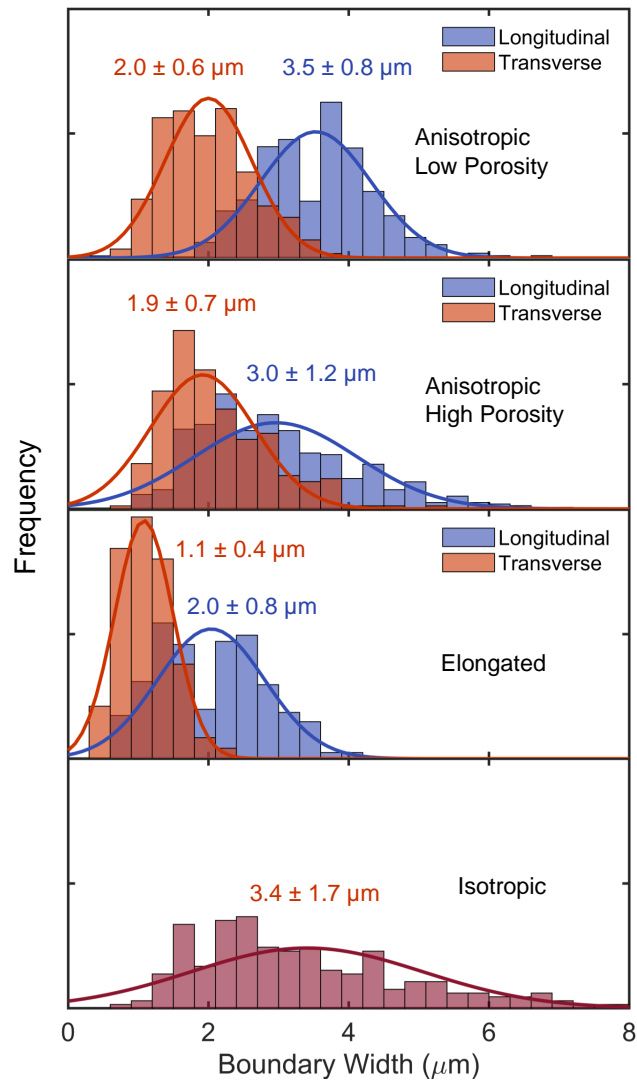
Figure 3.7: Grain Boundary Characteristics. (a) Normalized frequency distribution of grain boundary widths as collected from a minimum of 500 measurements.
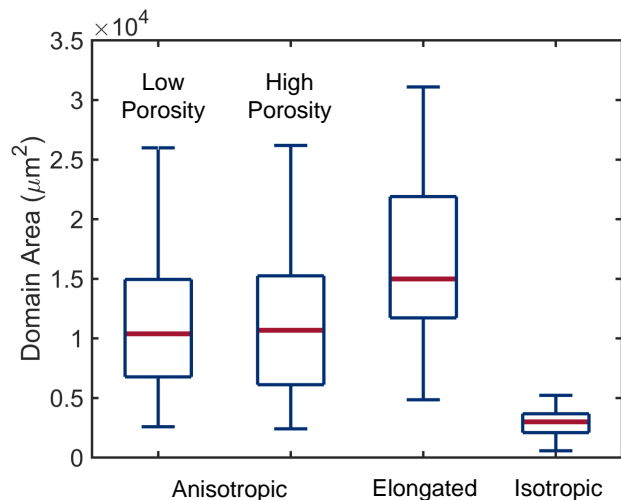
Figure 3.8: Porous Inverse Opal Domain Characteristics. Boxplot of grain domain area for IOs with various domain characteristics and porosities.

wettability of the functionalized copper IO with DI water and fluorescein fluid is $23.6° \pm 5.8°$ and $26.1° \pm 3.2°$ in static contact angle, respectively.

3.2.4 Liquid Surface Tension Measurements

The interfacial tension of the liquid in air γ_{al} is measured using the pendant drop method (Camera, WPI-UMP3). A microsryinge pump dispenses droplets from the liquid of interest from a syringe connected to a needle tip in ambient air at 22 °C (Figure 3.9). A high-speed camera records the formation of the pendant drop at 2000 fps, and the shape of the pendant droplet is analyzed using ImageJ software.

The interfacial surface tension of DI water is 72.75 ± 0.24 mN/m, which is similar to expectation. The introduction of fluorescein salt to DI water (1 mg/mL concentration) slightly increases the surface tension to 75.35 ± 0.54 mN/m, and the mixture of dextran (2.6 mg/mL concentration) and fluorescein salt in DI water further increases the surface tension to $79.66 \pm 1 \ 0.45$ mN/m.
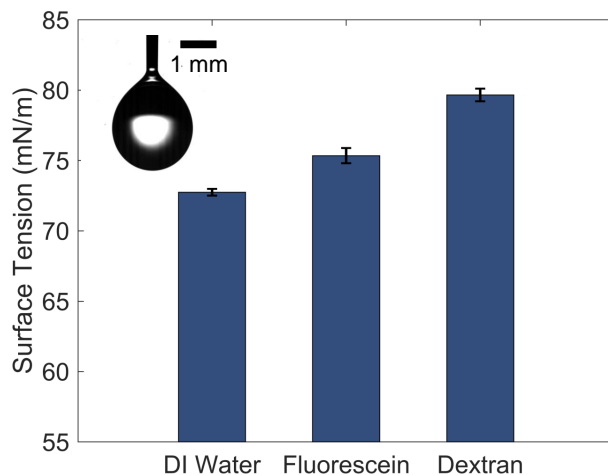
Figure 3.9: Surface Tension Measurements. Using pendant drop method in air (representative drop capture in inset).

3.2.5 Liquid Viscosity Measurements

The shear liquid viscosity is measured using a rheometer (Physica MCR 301, Anton Paar) equipped with a 2° cone and plate geometry (25 mm in diameter) and a truncation gap of 52 μm. The viscosities are measured at a controlled 22.5 °C during the shear ramp test from 0.5 to 100 s^{-1}. Figure 3.10 displays the liquid viscosity with varying shear rate. DI water as well as an aqueous solution of fluorescein sodium (1 mg/mL in concentration) possess a viscosity of 0.82 ± 0.04 and 0.87 ± 0.03 mPa*s, respectively, and are shown to be independent of shear rate as expected from a Newtonian fluid. Within the plotted data, the similarities between these viscosities make them difficult to be distinguished. This also indicates that the fluorescent dye has negligible effect on the viscosities of the DI water. With the additive of dextran (2.6 mg/mL in concentration) in the aqueous solution of fluorescein sodium (1 mg/mL), the liquid viscosity becomes two orders of magnitude higher than the previously examined fluids and increases with shear rate. Although the liquid viscosity depends on shear rate, the appropriate shear rate can be determined by the flow velocity of the fluid through the porous media as well as the intrinsic pore sizes and pore configurations of the media. [177] For calculation purposes, with a typical flow speed of 150 μm/min through an
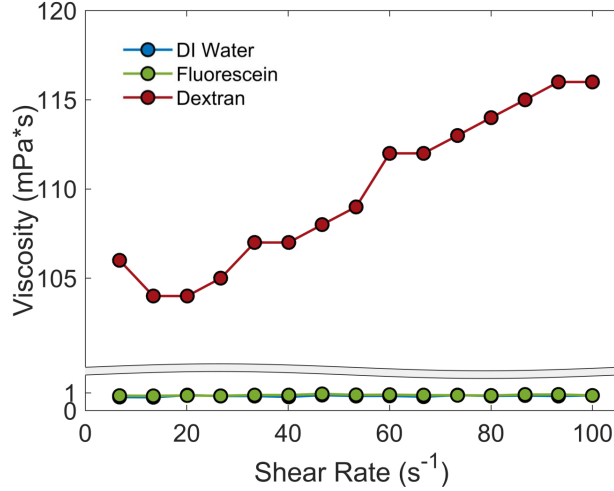
Figure 3.10: Shear Liquid Viscosity Measurement. Liquid viscosity as function of shear rate for DI water, aqueous solution of fluorescein sodium (1 mg/mL), and aqueous solution of dextran (2.6 mg/mL) combined with fluorescein sodium (1 mg/mL).

inverted bed of packed spheres with pore diameters of 0.6 μm, we can estimate the shear rate on the flow field to be approximately less than 10^{-1} s^{-1}.

3.2.6 Fluorescent Microscopy Imaging of Capillary Transport

The dynamics of in-plane liquid propagation through the polycrystalline IOs is microscopically monitored using a custom-designed setup compatible with the fluorescent microscope (Zeiss LSM700 inverted confocal laser scanning microscope). The moving liquid front is recorded across an area of 1080 μm $\times$ 1080 μm with a resolution of 3.56 μm $\times$ 3.56 μm per pixel at $\sim$2 Hz. Fluorescein signal is excited at the 488 nm wavelength, and the autofluorescent of the polycrystalline porous copper IO is excited at 639 nm. Figure 3.11 depicts the schematics of the inverted fluorescent microscope used to observe liquid propagation.

A customed fixture seals the IO for capillary saturation and is compatible to be observed with the inverted fluorescent microscope. The fixture consists of a top and bottom acrylic plate that encloses the PDMS gasket components (PDMS-coated glass coverslip and a molded
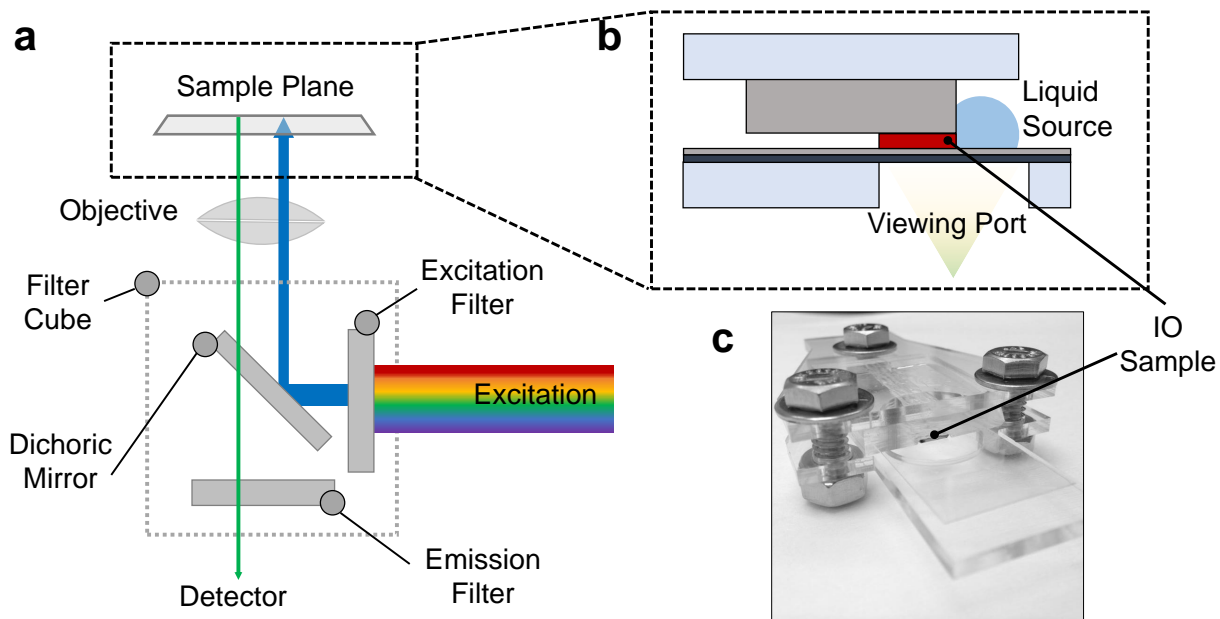
Figure 3.11: Fluorescent Imaging Setup. (a) Schematic operation of an inverted fluorescent microscope to detect fluorescein trackers on the sample plane, which uses a custom-built sample holder and sealer as shown (b) schematically and (c) optically.
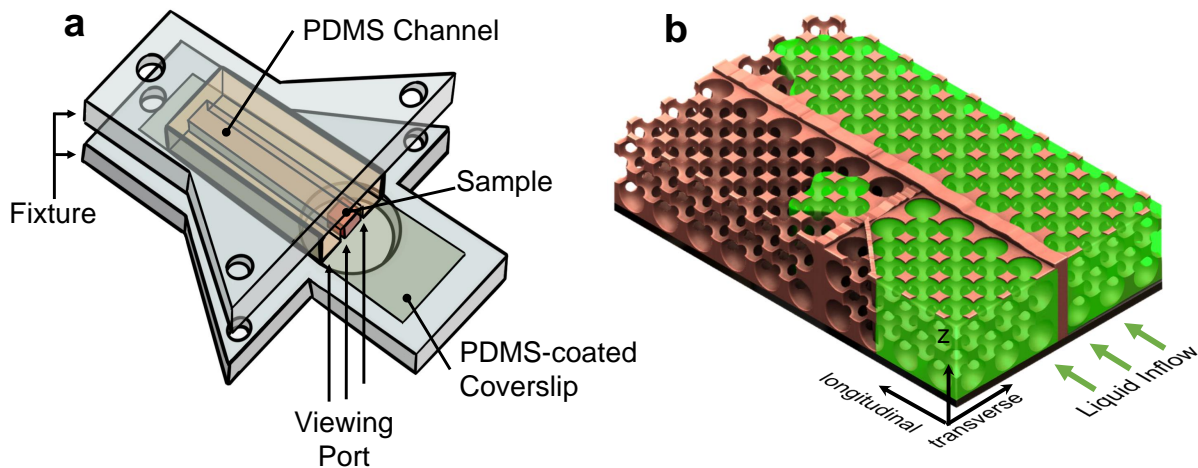
Figure 3.12: Fixture Setup Details for Fluorescent Imaging. (a) An acrylic fixture sandwiches the IO sample (flipped upside-down) between a PDMS-coated glass coverslip and a PDMS channel. The fixture is placed onto an inverted confocal microscope equipped with fluorescent imaging. (b) The liquid propagation through the IOs is observed through the viewing port, with liquid inflow occurring from the right to left.

PDMS top gasket sealer with a channel) and IO samples, as secured by fasteners. The PDMS gasket is prepared by mixing SYLGARD-184 base and curing agent at a 10:1 ratio, followed by degassing in vacuum desiccator for 1 hr. A thin film of PDMS coats the glass coverslip using a spin coater at 2000 rpm for 90 s to produce a film with thickness of ∼50 μm. The molded PDMS top gasket sealer is produced by pouring PDMS into a mold with a 0.65 mm thick raised slab (similar to the combined height of the IO and its carrier substrate); once cured and removed from the mold, it possesses a rectangular channel that fits the IO sample, and the channel allows the displaced air inside the IO to evacuate during liquid saturation. Both PDMS gasket components (glass coverslip and top gasket sealer) are cured in a lab oven (Lab-Line) at 70 °C for 3 h, and the top sealer is peeled from the mold afterward.For the inverted confocal fluorescent microscope, the top of the IO surface is flipped to face downward and meet the PDMS-coated glass coverslip. The PDMS top sealer aligns its rectangular channel over the IO sample and encapsulate it with the coverslip. The PDMS gasket and IO sample are then sandwiched between a top and bottom acrylic fixture plate. Tightening of the screws across the fixture provides uniform compressive forces to ensure adequate sealing of the IOs. Fluorescein sodium (Sigma Aldrich) is diluted in DI water by 1 mg/mL. Additionally, fluorescent fluid with higher viscosity is prepared by adding in dextran (2.6 mg/mL) to examine the role of viscosity in porous media liquid propagation. See Figure 3.12 for schematics of the customed fixture setup.

To initiate liquid propagation, ∼20 μL of the wicking fluid is pipetted onto the PDMS-coated coverslip adjacent to the IOs. The liquid droplet quickly latches onto the sample and is wicked in-plane through the porous medium. The hydrophobicity of the PDMS-coated coverslip prevents liquid wicking across the sealing surface and confines the capillary flow to within the IO and prevents evaporation. Similarly, the hydrophobicity of the PDMS top gasket sealer with rectangular channel prevents liquid from flooding the IO while the open channel allows air to be displaced from the IO as its space becomes occupied with liquid.

43

3.2.7   Liquid Propagation Analysis

From the fluorescent imaging of liquid propagation, the fluorescein-infused water (observed as green fluorescent signals when excited with a 594 nm wavelength laser) wets the copper IO media (observed as red signals from its autofluorescent when excited with a 639 nm wavelength laser) and displaces the entrapped air through capillary saturation with liquid inflow occurring from right to left across the media, as indicated in Figure 3.12b. The capillary wicking dynamics across porous grain domains and mass transport throttling across grain boundaries are monitored at ~2 Hz. By isolating the individual fluorescing channels (i.e., the fluorescent channel for the propagating liquid and the autofluorescent channel for the copper IO structure, as respectively shown in Figure 3.13a,b), the liquid propagation front is clearly discernable. Within the captured frames, the capillary saturated regions are highlighted with strong spatial contrasts, and the images are binarized to identify saturated and unsaturated regions for each frame to measure the time-varying propagation distance. To observe individual defect-mediated transport behavior at boundaries, the propagation of liquid over time is measured using post-processing computer detection conducted in two steps. First, to observe the stop-and-go liquid propagation motions along discretized boundaries, the detection follows the fluorescent propagation along 5 horizontal lines equidistant apart (see Figure 3.13c,d for representative post-processed images). Second, to characterize the nonuniform spatiotemporal distribution of the liquid front at high resolution at a given time, the liquid propagation is measured along ~1000 horizontal detection lines (i.e., one line per pixel across the video frame).

During image acquisition, the liquid flow is monitored from the inlet (i.e., from the right of the frame) and through its continued propagation across the frame (i.e., to the left). Once the propagating front approaches toward the end of the frame (left side), the stage is mechanically translated laterally to follow the moving front and keep it within the frame.
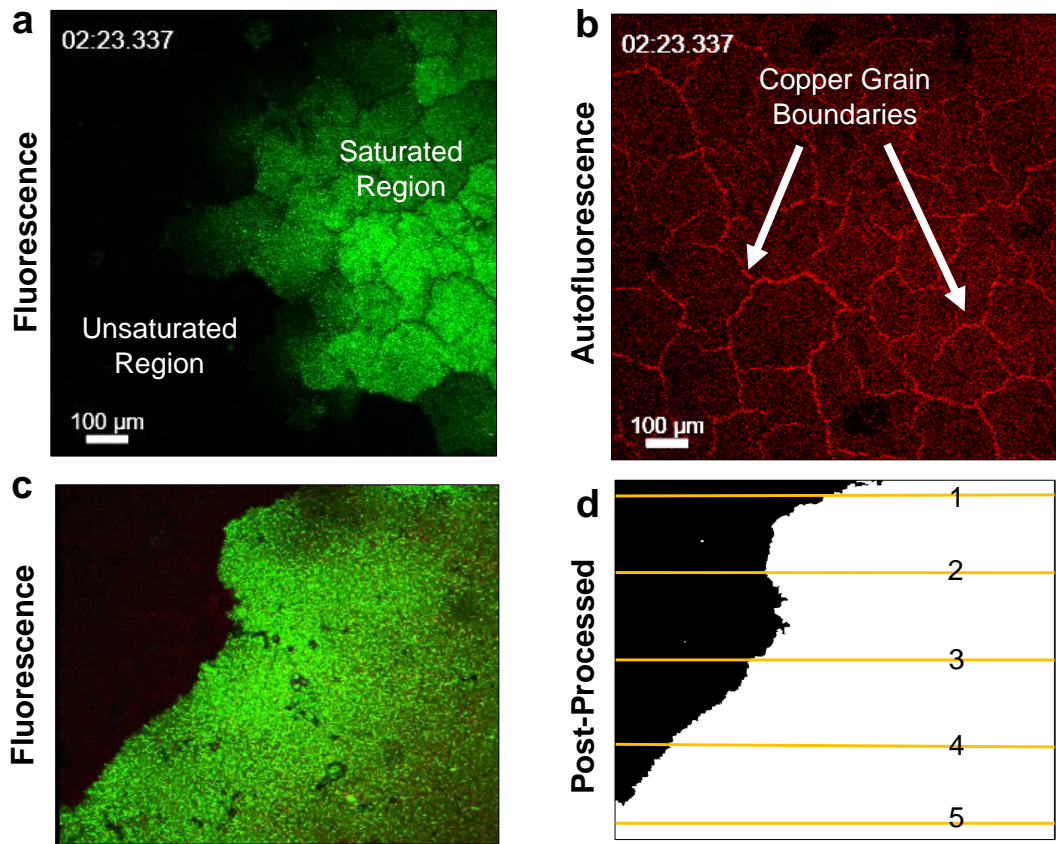
Figure 3.13: Fluorescent Liquid Propagation Analysis. Fluorescent microscope captures depict liquid flowing through the porous medium (from right to left of screen). Representative frame captures from (a) fluorescent channel selectively displaying liquid (green) saturating the porous medium and (b) autofluorescent channel showing the copper porous medium and its grain boundaries for IOs with isotropic-dominated domains. (c) A representative fluorescent frame capture and (d) its associate post-processed image with the propagated front being detected along five equidistant markers (yellow lines) for IOs with amorphous pore packing.

The translation distance and time are noted and incorporated into the propagation distance calculation (Figure 3.14).

The fluorescence images are then aligned and overlaid onto the stitched SEM map of each polycrystalline IO to correlate the high contrast liquid transport with the high-fidelity microstructural map. The relationships between the localized physical boundary structure and the concurrent liquid propagation dynamics are correlated to elucidate underlying structure-
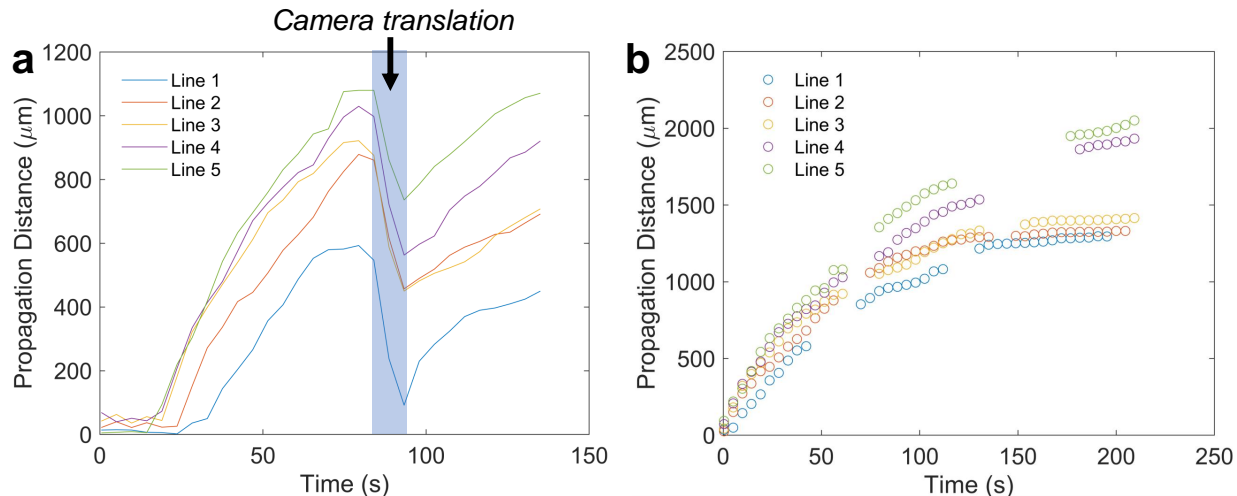
Figure 3.14: Wicking Image Post-Processing. (a) After the liquid front is detected, the propagation distance is measured along five equidistant lines. The plotted result shows a significant decrease in propagation distance due to camera translation to maintain the liquid front within the view of the frame. (b) The plotted propagation distance can be corrected by accounting for the time and distance taken during camera translation.

transport properties. For instance, a propagating front may saturate an entire domain but can be stopped at a grain boundary before eventually proceeding to circumvent it. By correlating such grain-scale events with a microscopic mapping of the IO, the observed transport characteristics of each grain boundary can be determined with specificity and locality.

3.3   Microhydrodynamic Transport in Inverse Opals

Due to the defect-prone and evaporation-dominated nature of the opal self-assembly during the vertical deposition process, grain domains often exhibit anisotropy in shape that are separated by prominent longitudinal (aligned to the direction of the moving meniscus) and transverse boundaries (orthogonal to the direction of the moving meniscus). By varying the sample preparation parameters, we can create IOs with differing degree of domain anisotropy, which we exploit to explore the directional-dependent transport behaviors. The anisotropic polycrystalline IOs are first positioned for liquid inflow to occur in the transverse

direction (i.e., flow following the general orientation of the transverse grain boundaries and thus having to predominantly crosses longitudinal grain boundaries). The samples are sequentially cleaned and dried before being rotated by 90° within the fixture to provoke flow in the longitudinal direction (i.e., flow following the general orientation of the longitudinal grain boundaries but predominantly crosses transverse grain boundaries).

3.3.1 Directional-dependent Wicking Behaviors

To explore the influence of domain anisotropy on direction-dominated flow, we measure capillary flow through IOs that are anisotropic with low porosity (78.0 ± 5.8%), anisotropic with high porosity (90.9 ± 2.4%), and elongated (defined as extremely anisotropic, 80.3 ± 3.2% in porosity), see Samples 1-3 in Table 3.1. The sample orientation illustration, top-view SEM image of representative samples, and associated fluorescent evolutions are shown in Figure 3.15a for *anisotropic* IO domains. In tracking the propagating front (Figure 3.15b-d), the domain anisotropy induces preferential directional flow along the prescribed longitudinal direction (blue lines) compared to the transverse direction (green lines). The faster liquid propagation along the longitudinal direction is indicative of the lower hydraulic resistance expected for a reduced linear density of grain boundaries.

We observe similar propagation rate along the longitudinal direction for Anisotropic Low Porosity and Anisotropic High Porosity (blue spatiotemporal plots in Figure 3.15b,c, respectively), reaching a traveling distance of ∼3 mm by 200 s. This can be attributed to longitudinal flow direction predominantly crossing transverse boundaries, which are comparable in width (Figure 3.7). In comparison to its Low Porosity counterpart, High Porosity possesses smaller longitudinal boundary widths, which allows it to propagate at a faster rate in the transverse direction (green spatiotemporal plot in Figure 3.15b,c). This suggests that the widths of grain boundaries correlate to the amount of hydraulic resistance posed by the
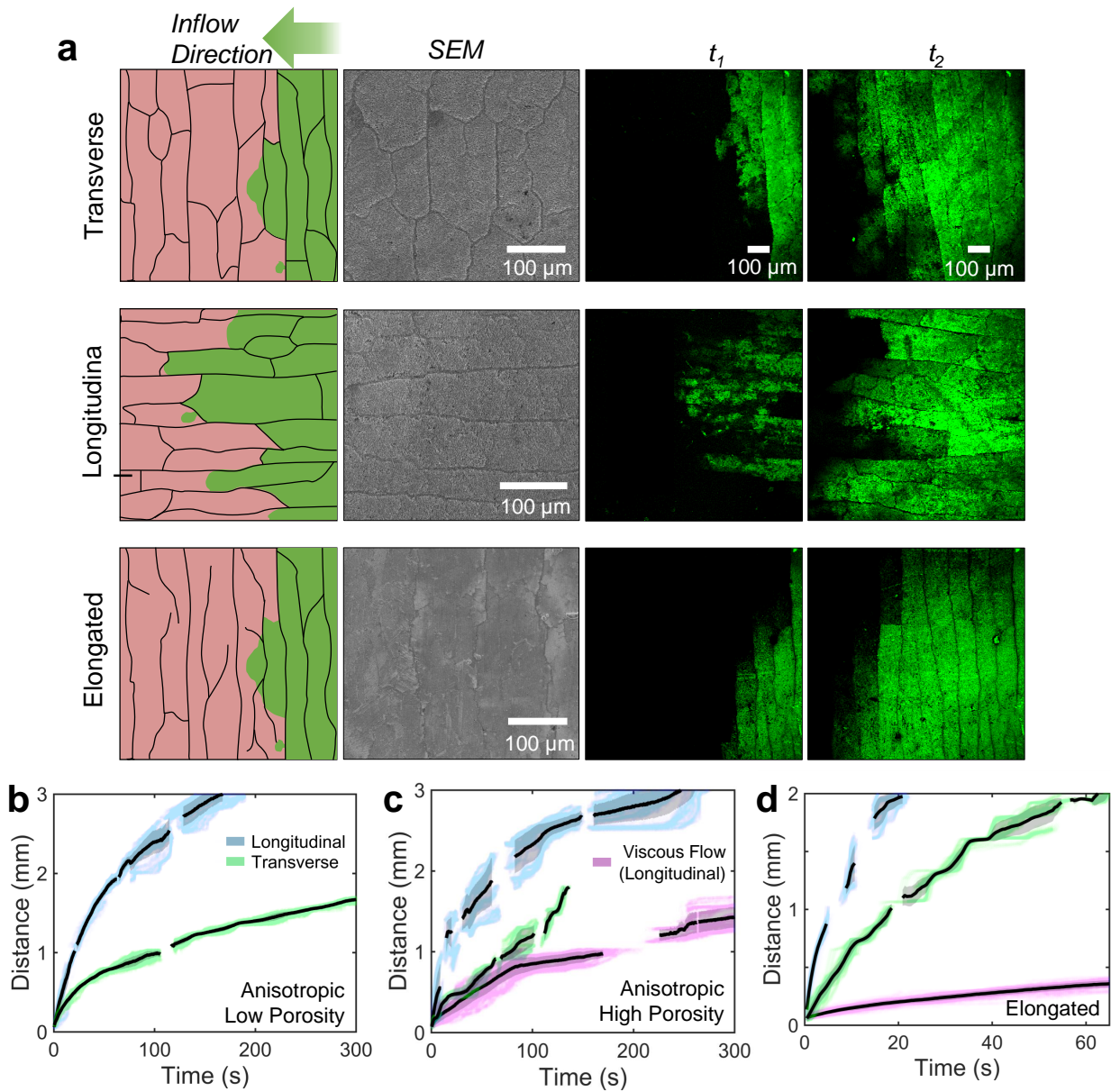
Figure 3.15: Directionally Dependent Liquid Propagation across Inverse Opals with Various Flow Configurations and Degrees of Polycrystallinity. (a) The different flow configurations are represented through schematic illustrations, representative plan view SEM images of the associated IOs, and fluorescent frame captures of liquid propagation over time. The propagation front is detected with pixel-based resolution and plotted for (b) anisotropic with low porosity, (c) anisotropic with high porosity, (d) elongated domains (b-d) The propagating liquid front monitored at pixel-based resolution are displayed as a culmination of overlapping colored lines that display a band range based on the flow directions (blue: longitudinal, green: transverse, magenta: longitudinal for high viscous fluid). The plotted black lines represent the mean of the pixel-based data, and the translucent gray bands represent the standard deviations.

barriers in throttling the fluid propagation. It should be noted that High Porosity has a terminal propagating distance of $\sim$2 mm, which is limited by the sample size ($\sim$3 mm $\times$ 2 mm). Furthermore, while we expect that structural porosity controls the permeability of the fluid transport pathways, we observe minimal influence of porosities on propagation when dominant hydraulic resistance factors, such as polycrystalline boundaries, are present. Instead, the anisotropic layout of the porous domain has been demonstrated to significantly alter the nature of propagation, such as discretized and delayed stop-and-go motion, preferential directional transport, and wicking rate. Despite the differences in porosity, the statistical population of the porous domain area for both Anisotropic samples are almost identical (Figure 3.8). The outlines of the grain boundaries projected from High Porosity are shown in Figure 3.5a. Since Low Porosity exhibits similar polycrystalline characteristics in boundary width and domain area, its boundary projection is not shown.

The study of directional transport is extended to extremely anisotropic domains (denoted as Elongated). Compared to Anisotropic IOs, the boundary widths of Elongated are much smaller in either directions (Figure 3.7) while its domain areas remain the largest (Figure 3.8). The increase in domain areal coverage indicates a reduction in density of grain boundaries as visually corroborated with the boundary outline projection displayed in Figure 3.5b. The microstructural map also reveals that most boundaries are loosely connected such that domains have direct access between grains as opposed to being truly isolated, causing the effective permeability to remain high. The wicking fluid circumvents around boundaries by finding openings between domains with more ease, decreasing the resident time during fluid confinement behind grain boundaries. The combinations of lower grain boundary density, smaller boundary widths, and more grain-to-grain connections reduce the modes of hydraulic resistances and thus a three-fold increase in propagation rate over the previous Anisotropic IOs (Figure 3.15d).

3.3.2 Effects of Fluid Viscosity on Permeation through Polycrystalline Porous Media

Viscosity influences the nature of the friction associated with fluid transport and may impact transmission across grain boundaries. Dextran is added to the aqueous fluorescein tracking fluid to increase its viscosity by two orders of magnitude (Figure 3.10). Since wicking in the longitudinal direction presents lower hydraulic resistance, we measure the wicking in this direction using the viscous dextran-based fluid for the Anisotropic and Elongated IO domains, shown as magenta colored spatiotemporal propagation in Figure 3.15c,d. It should be noted that while we experimented with viscous wicking in Anisotropic Low Porosity, the propagation stops within less than ∼0.1 mm due to significant flow resistance and therefore is not plotted. Elongated IO previously demonstrated the fastest propagation rate with regular fluorescein fluid; however, its wicking rate under the highly viscous fluid is approximately half that of Anisotropic High Porosity.

We initially expect that the lower defect density and smaller defect size of Elongated promote it to wick faster with minimum hydraulic resistance, but it fails to do so under viscous wicking. Instead, viscous wicking is shown to be most efficient in media with higher porosity and open permeable pathways. Since the liquid viscosity induces friction between the moving fluid and the solid surface, higher permeability provides fewer opposing forces to the fluid movement. As previously noted from the pair of Anisotropic IOs, the effect of porosity may hold negligible influence on transport behaviors when domain and boundary resistances are present. However, as the fluid viscosity itself becomes the dominant mode of hydraulic resistance, the structural porosity significantly affects transport rate.
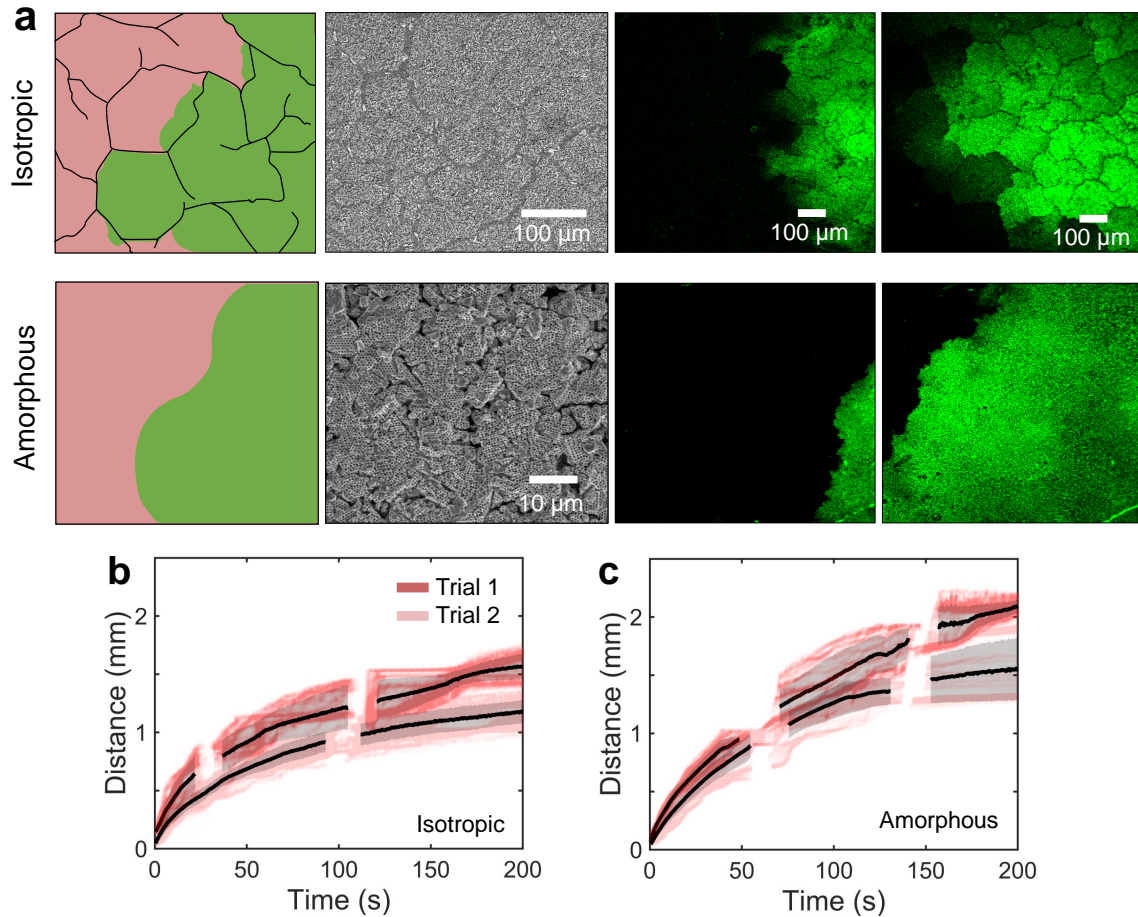
Figure 3.16: Nondirectionally Dependent Liquid Propagation across Inverse Opals. (a) IOs with isotropic domains and amorphous pore packing. To demonstrate the limited effect of directionality in flow behaviors, (b) isotropic and (c) amorphous samples are rotated by 90° between capillary-assisted transport measurements (red: 0°, pink: 90°). The plotted black lines represent the mean of the pixel-based data, and the translucent gray bands represent the standard deviations.

3.3.3 Nondirectional-dependent Wicking Behaviors

In the absence of domain anisotropy, we expect that transport exhibits limited preference in directional flow. To confirm, we rotate Sample 4 and 5 (simply denoted as Isotropic and Amorphous, respectively) by 90° between capillary-assisted wicking trials to examine the degrees in which propagation differ. Figure 3.16a conveys the observed wicking behaviors across Isotropic and Amorphous, and Figure 3.16b,c plots the propagation using spatiotemporal data. The two separate trials (pink and red lines) closely match with some overlapping spatiotemporal data, which demonstrates that these IOs closely exhibit nondirectional flow preferences. The minor disparities between trials can be contributed to the nonuniform degree in domain isotropy (Isotropic) and the heterogeneity in the randomly packed pores (Amorphous).

As observed from the fluorescent imaging (Figure 3.16a), the fluid propagation behaviors through Isotropic are still limited by grain boundaries but are less directionally oriented, while fluid in amorphous structure propagates and spreads in a diffusion-like manner. The boundary width of Isotropic widely ranges (Figure 3.7), and its domain area is at least five times smaller than the other IO samples (Figure 3.8), which also indicate a high defect density (Figure 3.5). Because the amorphous structure lacks crystalline characteristics, no grain boundaries or domain sizes are available for analysis. The capillary wicking of Isotropic in Figure 3.16b displays similar propagation rate to that of Anisotropic Low Porosity in the transverse direction, which is the slowest amongst all samples and directions for low viscous wicking. This is attributed to the high structural defect density of the Isotropic. In contrast, the Amorphous slightly outperforms Isotropic but still underperforms compared to all Anisotropic samples in the longitudinal direction. While fluid can wick with less resistance due to the lack of boundary defects in the amorphous structure, the randomly pack pores (often non-interconnected pores) create tortuous permeable pathways that leads to tremendous hydraulic resistance across the medium.

3.4 Analyzing Microscopic Transport across Boundaries

Traditional vertical rate-of-rise wicking measurements are often conducted in an enclosed environmental chamber to decrease evaporation effect, but the wicking medium remains exposed to the air within the chamber. As IOs wick from the liquid reservoir in this setup, we previously observed that the wicked liquid saturates the interconnected pore matrix before halting its progression at a grain boundary. [9] To minimize the surface energy of the polycrystalline IO and promote continuing propagation, a molecular liquid film coats the boundaries and eliminates the liquid-vapor interfaces across the physical obstructions, [72] given that the boundaries themselves are hydrophilic to support surface wetting. The molecular liquid film propagation across boundaries is driven by the energy obtained from the wicking liquid filling the porous domains between boundaries. Thus, we often observe that while the wicking front progression may be inhibited behind grain boundaries, after a certain amount of time as the liquid fills in more of the porous domain in three dimensions (as confirmed by the increasing intensity of the green fluorescent signals within the trapped domain over time), the liquid is eventually propelled to cross and diffuse into the adjacent domain.

In the present experimental configuration, the IOs are sealed and sandwiched between two hydrophobic PDMS-based fixtures. The open top of the IOs are pressed against a PDMS-coated glass coverslip, covering any protruding grain boundaries and allowing liquid to only propagate across boundaries where their localized heights are lower than the domain thickness (often at a slow rate). Otherwise, we deduce that the continual wicking across polycrystalline boundaries are possible through means of physical defects and nonuniformities along the grain boundaries themselves since thin liquid film cannot flow over the sealed boundaries. This is evident by inspecting the fluorescent imaging, which distinctly shows green
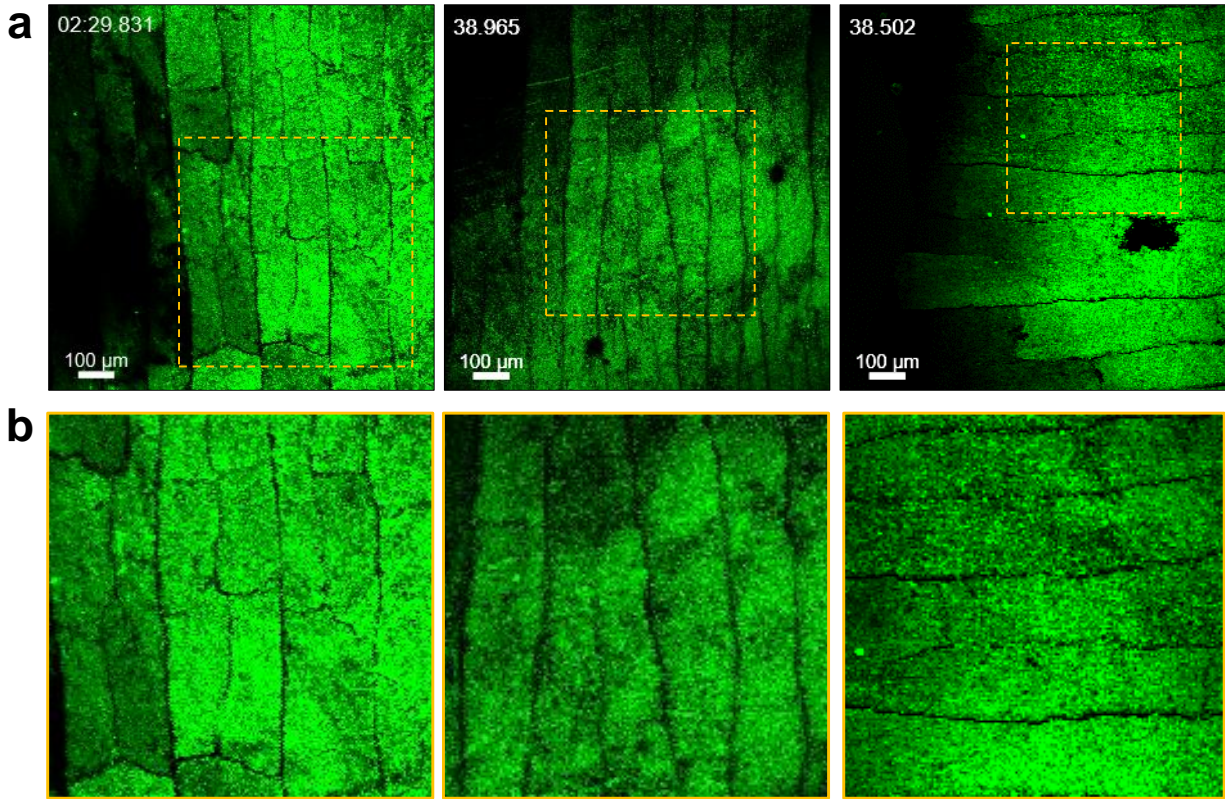
Figure 3.17: Wicking in the Presence of Grain Boundaries. (a) Fluorescent wicking images from various IO samples, and (b) close-up view of their respective region of interest (dashed yellow square), which shows liquid does not flood over grain boundaries since their features are still discernable. This suggests that majority of grain boundaries are sealed by the current experimental configuration (i.e., pressed against a PDMS-coated glass coverslip) such that liquid cannot propagate across them.

fluorescein signals incapable of flooding over grain boundaries the majority of the time, as repeatedly shown in Figure 3.13, Figure 3.15, Figure 3.16, and Figure 3.17. The prevention of thin liquid film flowing over grain boundaries significantly decrease the wicking rate in this current fluorescent-based experimental setup in comparison to the traditional vertical wicking configuration conducted in an environmental chamber. Previously reported the average vertical wicking rate of 0.6 μm diameter copper IOs is approximately 50 µm/s, [9] which is at least three times faster than with similar IOs (anisotropic domains) in a fully sealed configuration as presented in this work.

Using fluorescent-aided microscopic imaging to detect the propagating front, we monitor the movements of the fluorescent tracers at a microscopic level cross the boundaries. Overlaying the propagating fluorescent images over a microscopically detailed map of the wicking medium (e.g. top-view SEM images of IOs), we correlate and analyze the propagating front behaviors to the types of physical obstructions (and potential defects and nonuniformities along the boundaries) at high fidelity in spatial contrasts, spatial and temporal resolutions.

Through leveraging the capabilities of fluorescent imaging technique, we combine multiple filtered imaging channels, such as fluorescent (displayed as green signals for wicking fluid) and autofluorescent (red signals for grain boundaries), to track both the liquid front and the presence of grain boundaries. Representative captures are shown in Figure 3.18. The moment during which a liquid front reaches a boundary but cannot propagate across it, we denote it as t_{stop}, which is set to 0 s. Once the fluorescent tracer signals cross the boundary, we denote it as t_{cross}; we continue to observe as the wicking fluid diffuses into the adjacent domain, and this is shown in Figure 3.18 at an arbitrary time as $t_{diffuse}$ after the occurrence of t_{cross}. The time difference between t_{stop} and t_{cross} reveals the amount of hydraulic resistance poses by the grain boundary, which tend to increase with growing distance from the liquid source. The further away the liquid front is from its supply source, the more the fluid accessibility to its source becomes restricted due to the increasing number of physical obstructions along the wicking pathway, which negatively affects the wicking rate as well as resident time required to overcome a grain boundary. Through detailed SEM examination of the localized site where fluid crosses the grain boundary, we demonstrate that grain boundaries may also possess minor defects along their length, such as discontinuities along the barrier and nonuniform grain boundary width and height, allowing the liquid to propagate across defects with a finite flow resistance from the constrictions.

For instance, Figure 3.18a exemplifies the case in which the height of grain boundaries varies, causing the wicking fluid to predominantly traverses across boundary regions with
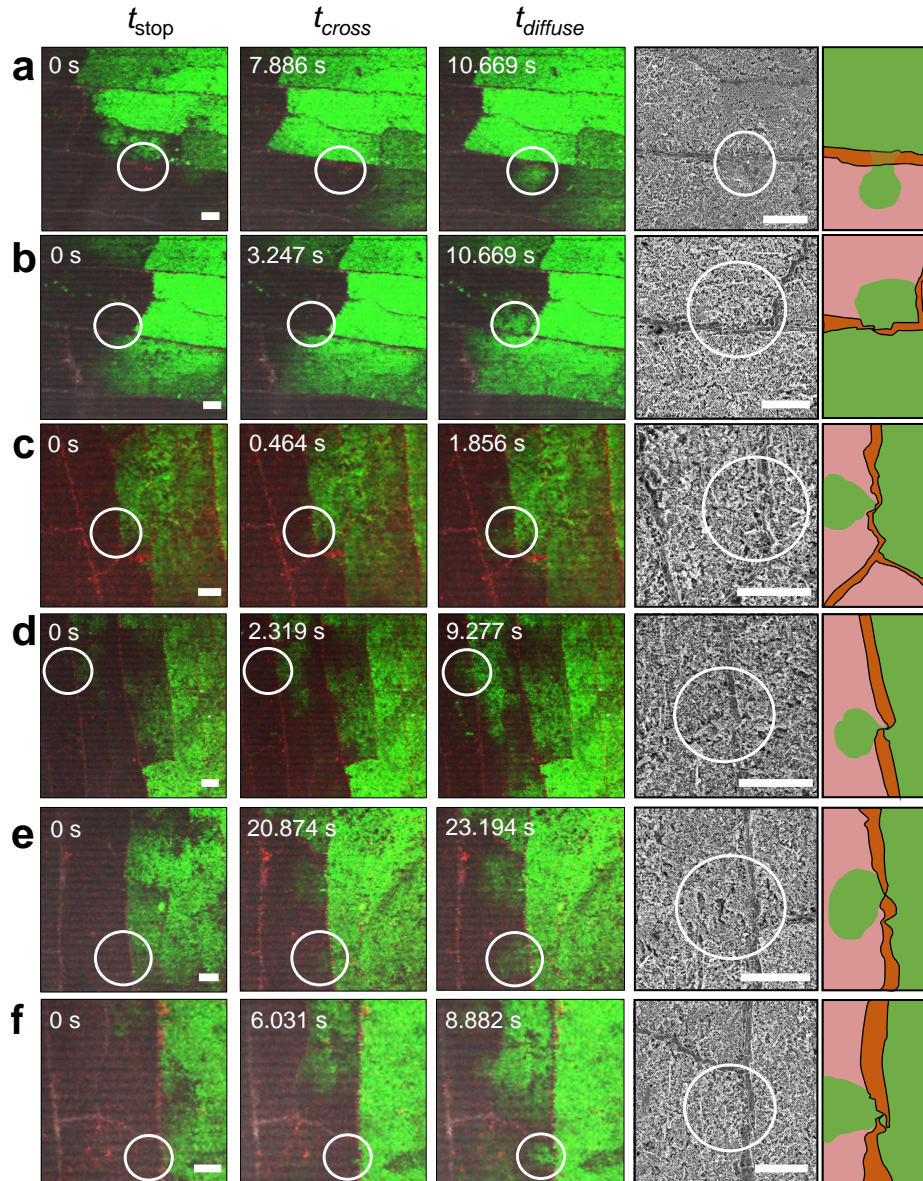
Figure 3.18: Detailed Microscopic Wicking across Grain Boundaries. When the liquid propagation is locally hindered by a grain boundary, the event is denoted as t_{stop} and is considered 0 s. The local liquid stoppage is monitored until the first fluorescent signal indicating that it crosses the boundary, and the time of this occurrence is determined as t_{cross} while the localized location in which the liquid crosses are circled. After crossing the boundary, the liquid propagates in a diffusion-like manner within the adjacent porous domain, which is observed during $t_{diffuse}$. SEM images showing the associated boundary regions in which the liquid crosses, and the illustration depicting the boundary characteristics and mode of liquid crossing. Row (a,b) displays wicking occurring the longitudinal direction, and row (c-f) shows wicking in the transverse direction. All scale bars are 50 μm
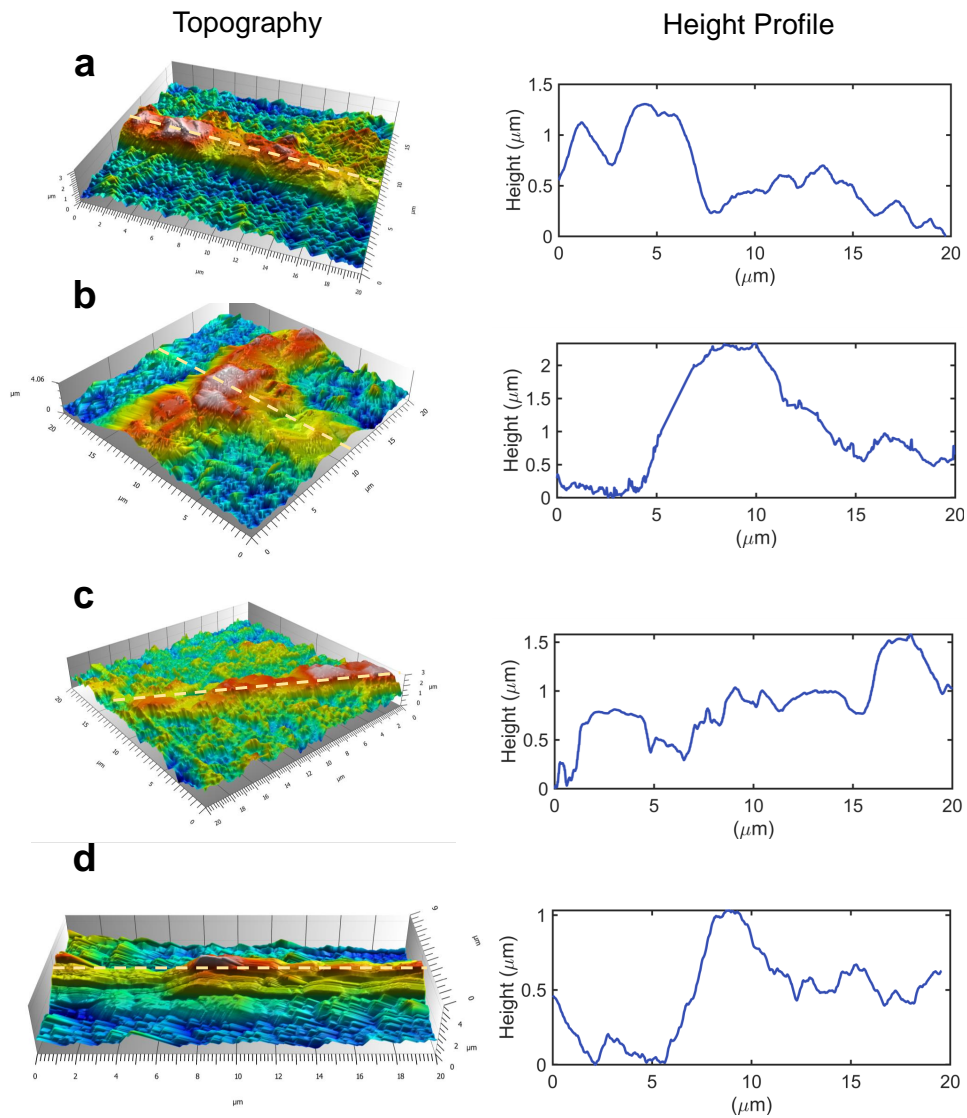
Figure 3.19: Atomic Force Microscopy Topography Scans of Grain Boundaries.
(a-d) Representative scans of various grain boundaries shown through 3D reconstructions and height profiles associated along the denoted yellow dashed lines.

lower heights to minimize hydraulic resistance. The changes in boundary height is evident from top-view SEM image by observing the contrast level in boundary definition and can be further corroborated with Atomic Force Microscopy (AFM), as presented in Figure 3.20. Reviewing cross-sectional SEM images of IOs, the typical boundary height can range from protruding ~ 2 μm above or remaining below the IO domains (Figure 3.1). AFM scans
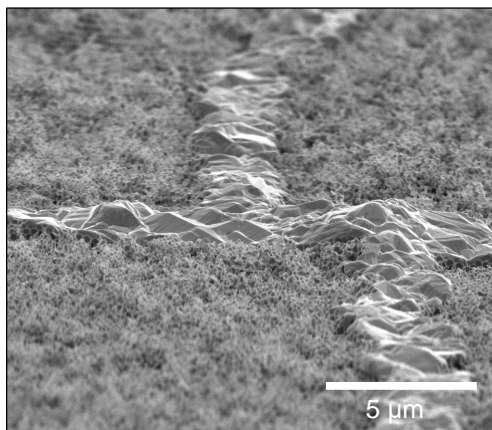
Figure 3.20: Angled Cross-sectional SEM Image of Copper Crystal Protruding along Grain Boundaries. Microscopic roughnesses of grain boundaries surrounded by porous domains.

shows that within a localized region of the grain boundary (20 μm × 20 μm region of interest), its height can fluctuate by 1 μm. While the majority of the protruding boundaries are sealed by the PDMS-coated glass coverslip, boundary heights can vary slightly during the electrodeposition of copper crystals. Slight decreases in boundary height provide gaps between the hydrophilic grain boundary and hydrophobic PDMS-coated cover for liquid to traverse across. However, the hydrophobicity of the PDMS cover will still induce significant resistance to wicking against its surface, which can contribute to a high t_{cross} before being able to wick across the localized boundary site.

Additionally, the widths of grain boundaries are nonuniform along their lengths. As representatively shown in Figure 3.18b-f, the liquid often wicks across boundaries where their width drastically narrows or pinches off as these defective sites offer potential nanoscopic openings for liquid to impregnate through. It is well known that the characteristic width of grain boundaries manifest from the inversion of the cracks formed during the crystalline self-assembly of microspheres. However, it is also of interest to note that these boundary defect sites often exist near regions where boundaries branch off the perpendicular direction

(Figure 3.18b,c,e,f). During the opal assembly process, cracks branch off to lower the energy of the crystalline opal template, [162] but such stark changes in the directionality of the crack may disturb the nearby crack formation characteristics, possibly causing the crack width to drastically widen or narrow.

3.5 Defect-Mediated Transport Parameters
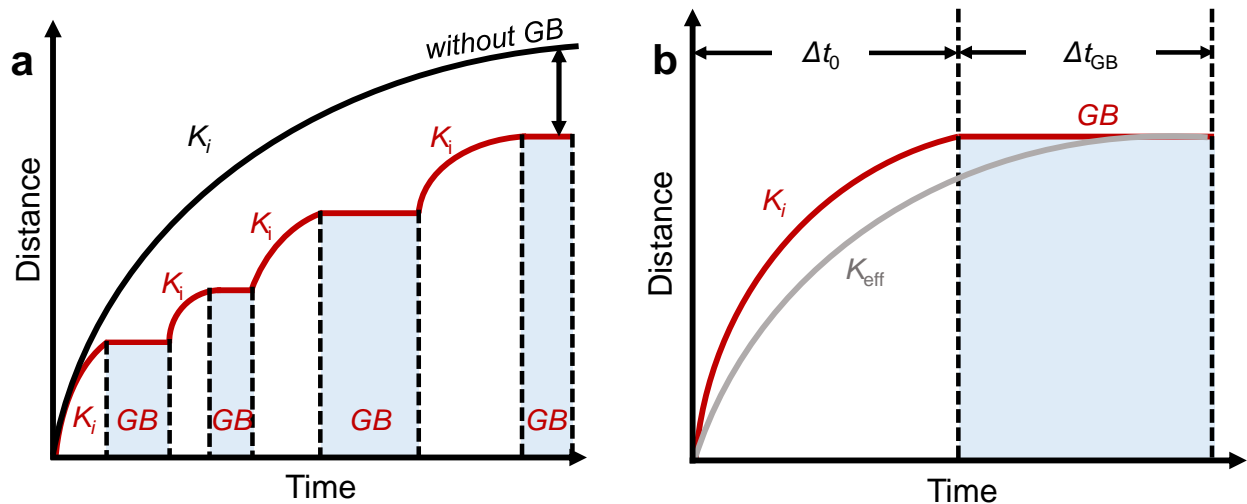
Figure 3.21: Schematic of Liquid Propagation in the Presence of Grain Boundaries. The liquid rise is periodically hindered by grain boundaries (denoted as GB). Using the Darcy equation, the effective permeability that takes into account structural defects can be determined; the ideal permeability (i.e., flow through defect-free structures) can also be estimated from the fluid transport through single porous crystals.

To construct generalized solutions to the effective transport model, the hydraulic resistance induced by grain boundaries must be ascertained, which can be revealed through the time impedance throttled by the defect-limited liquid propagation as compared to the propagation rate within ideal single crystals (Figure 3.21). Monitoring the discretized stop-and-go wicking motion across grain boundaries, the liquid rate-of-rise within individual domains is fitted to

59

model the Darcian flow through defect-free porous structures, as representatively shown in Figure 3.22, showing good agreement with the empirical results (colored circle markers). The residence time that the liquid remains pinned at the grain boundaries is denoted as Δt_{GB}, which is equal to t_{cross} - t_{stop}.
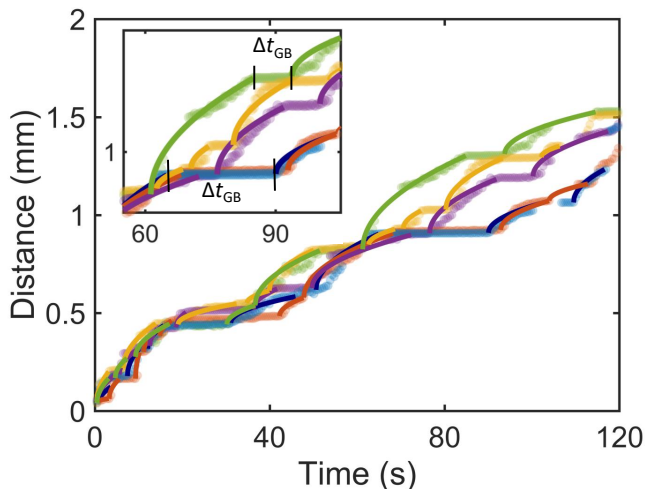
Figure 3.22: Data Fitting of Individual Liquid Rise within Single Crystalline Grain. Following the liquid propagation along five equidistant lines, the liquid rise is fit to Washburn Equation to derive intrinsic permeability within the individual grain. The inset shows a close-up view of the plotted data and the guided annotation showcasing the stoppage in liquid rise at grain boundaries, and the time delay is denoted as Δt_{GB}.

The extraction of Δt_{GB} for all polycrystalline IOs are presented as statistical distribution in Figure 3.23. The majority of grain boundaries permit liquid to percolate across within 3 s. However, by examining Δt_{GB} as a function of spatial and temporal coordinates, the time delay caused by grain boundaries generally increases with time and distance from the liquid source (Figure 3.24), which indicates throttling to fluid transport compounds with increasing number of defects along its working length. This also suggests that the intrinsic permeability of the IO structure varies across individual domains and deviates from the capillary driven flow Darcy type model. This is corroborated with the intrinsic permeability associated single crystalline domains K_i as derived from the Washburn equation in Figure 3.25a. Furthermore, the directionally-dependent flow significantly influences K_i, such that
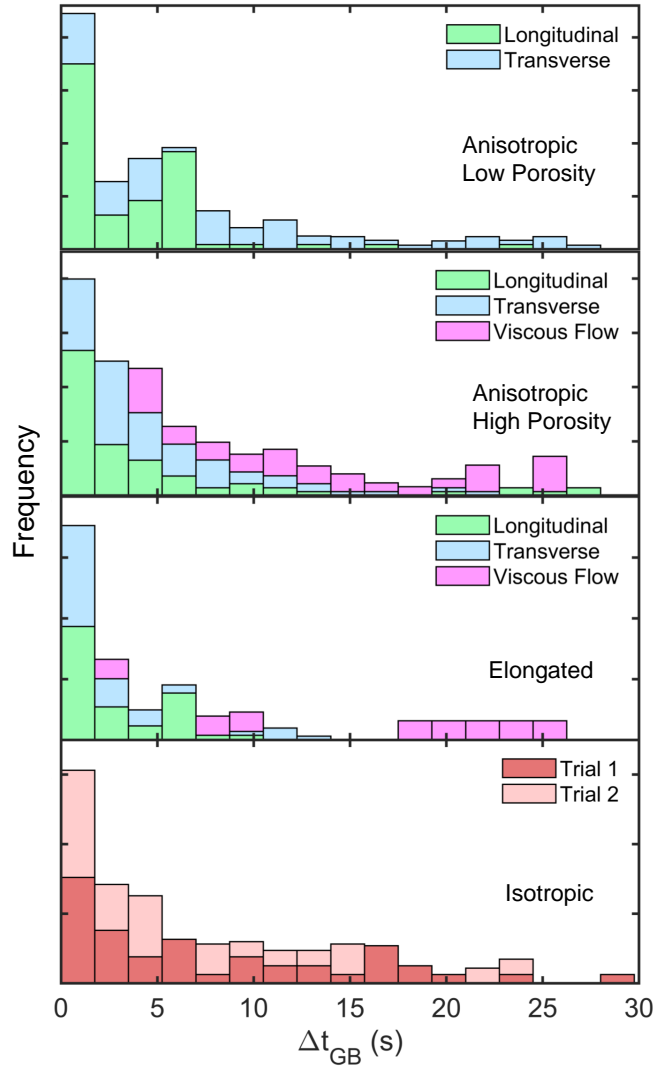
Figure 3.23: Statistical Time Distribution of Liquid Remaining Pinned at Grain Boundaries. Stacked histogram distribution based on the amount of time it takes to percolate across a boundary, shown for longitudinal (green), transverse (blue), and viscous flow (magenta) as well as nondirectionally-dependent flows (red and pink).

flow in the longitudinal flow (green circle markers) generally remains one order of magnitude higher in K_i than in the transverse direction (blue circle markers).

Examining the liquid propagation linearly along the expanse of multiple grain domains for Anisotropic High Porosity, K_i decreases inversely with the number of domain traveled across
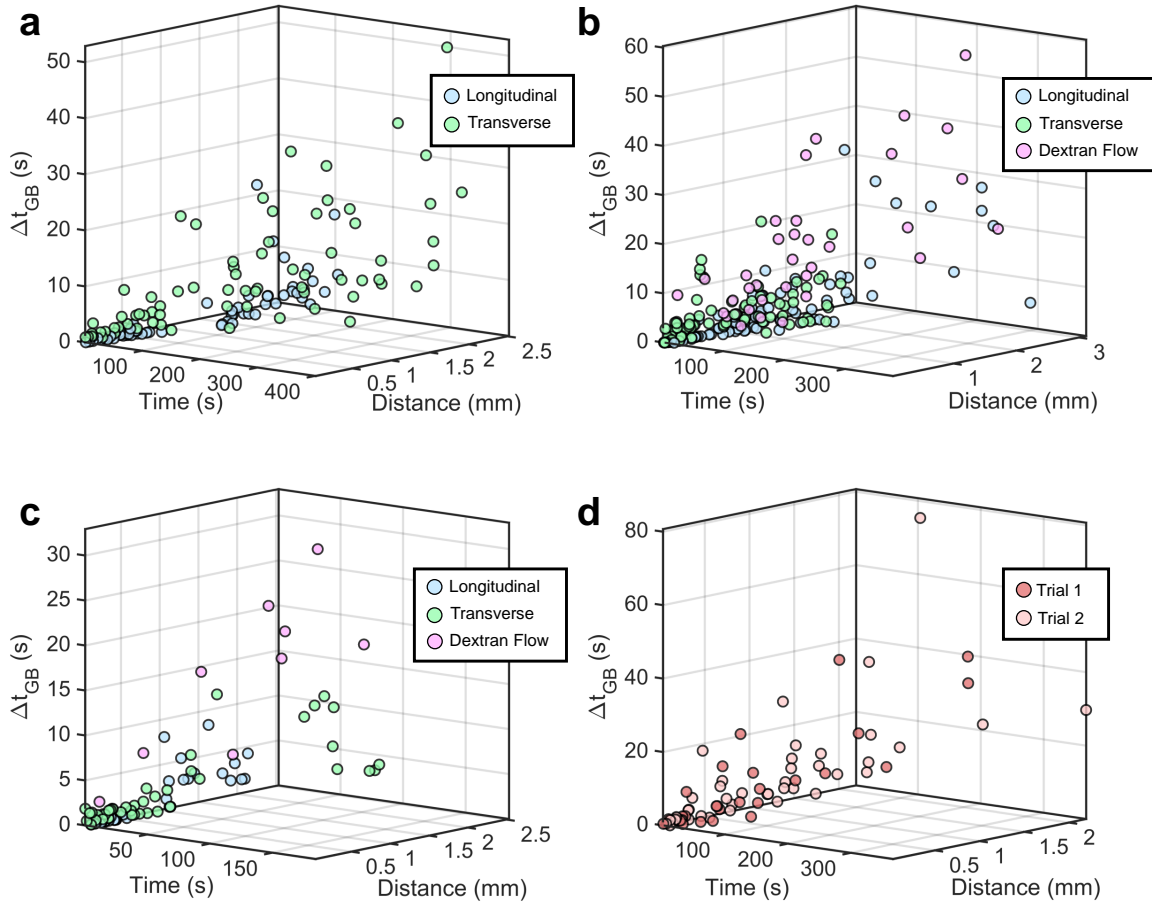
Figure 3.24: Spatial and Temporal Distribution of Δt_{GB}. The propagation time delay caused by grain boundaries for (a) Anisotropic Low Porosity, (b) Anisotropic High Porosity, (c) Elongated, and (d) Isotropic IO domains. The time impedance is monitored for flow in the longitudinal (blue), transverse (green), and viscous flow in the longitudinal direction (magenta) for (a-c) anisotropic and elongated domains. (d) Flow through isotropic domain is monitored through two separate trials (red and pink) by rotating the sample 90° in between.

(Figure 3.25b). It should be noted that while the flow across a linear array of domains provides simple and clear visualization of the flow behaviors, it fails to capture the complex 2D transport behaviors occurring between neighboring domains in the longitudinal- and transverse-coordinates.
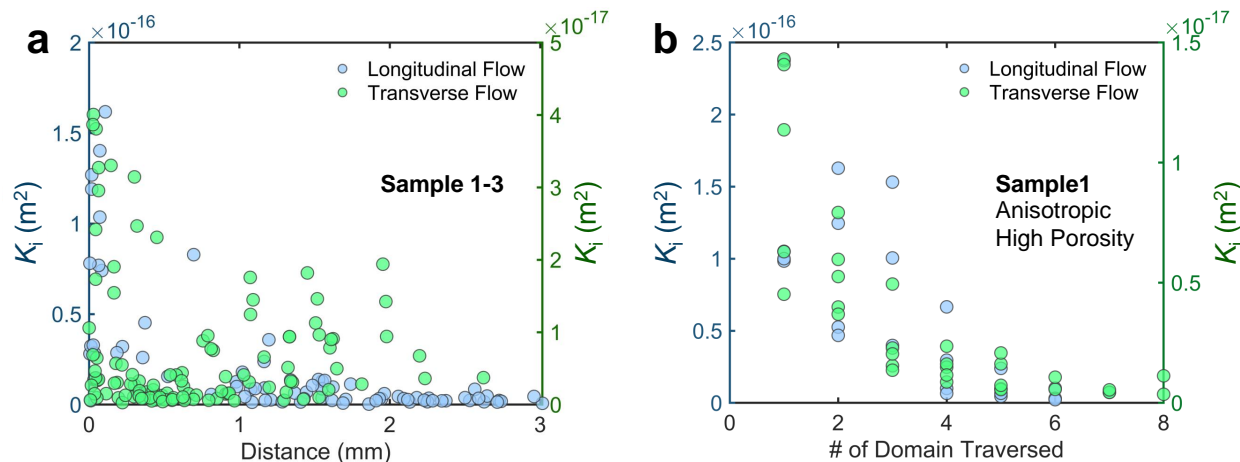
Figure 3.25: Estimated Permeability within Individual Grain over the Duration of Liquid Propagation. (a) Increasing the distance between the propagating front and the liquid reservoir induces a reduction in the intrinsic permeability within each grain K_i due to the throttling caused by increasing number of grain boundaries along the propagation pathway. (b) Similarly, K_i decreases with increasing number of porous domains the liquid traverses across. The K_i presented in during the longitudinal and transverse flow direction is plotted in blue and green, respectively. The left y-axis (blue) corresponds to K_i in the longitudinal flow direction while the right y-axis (green) corresponds to the transverse flow direction. (a) Showcases K_i obtained for Sample 1-3, excluding viscous flow, and (b) displays the data for Sample 1.

The ideal Darcian flow describes the upper-limit in capillary driven transport through continuum porous media, which can be closely estimated for crystalline IOs with nondefects by quantifying the intrinsic permeability within single crystals near the liquid source, which exhibit minimal effects from grain boundaries. Using the ascertained K_i from the first domain, the ideal liquid propagation for defect-free IOs are shown in Figure 3.26 for directional-dependent flow and in Figure 3.27 for nondirectionally-dependent flow as black lines. The gray lines represent fluid advancement due to the effective permeability K_{eff} associated with grain boundaries. For the majority of the wicking cases, projected K_i (black lines) slightly
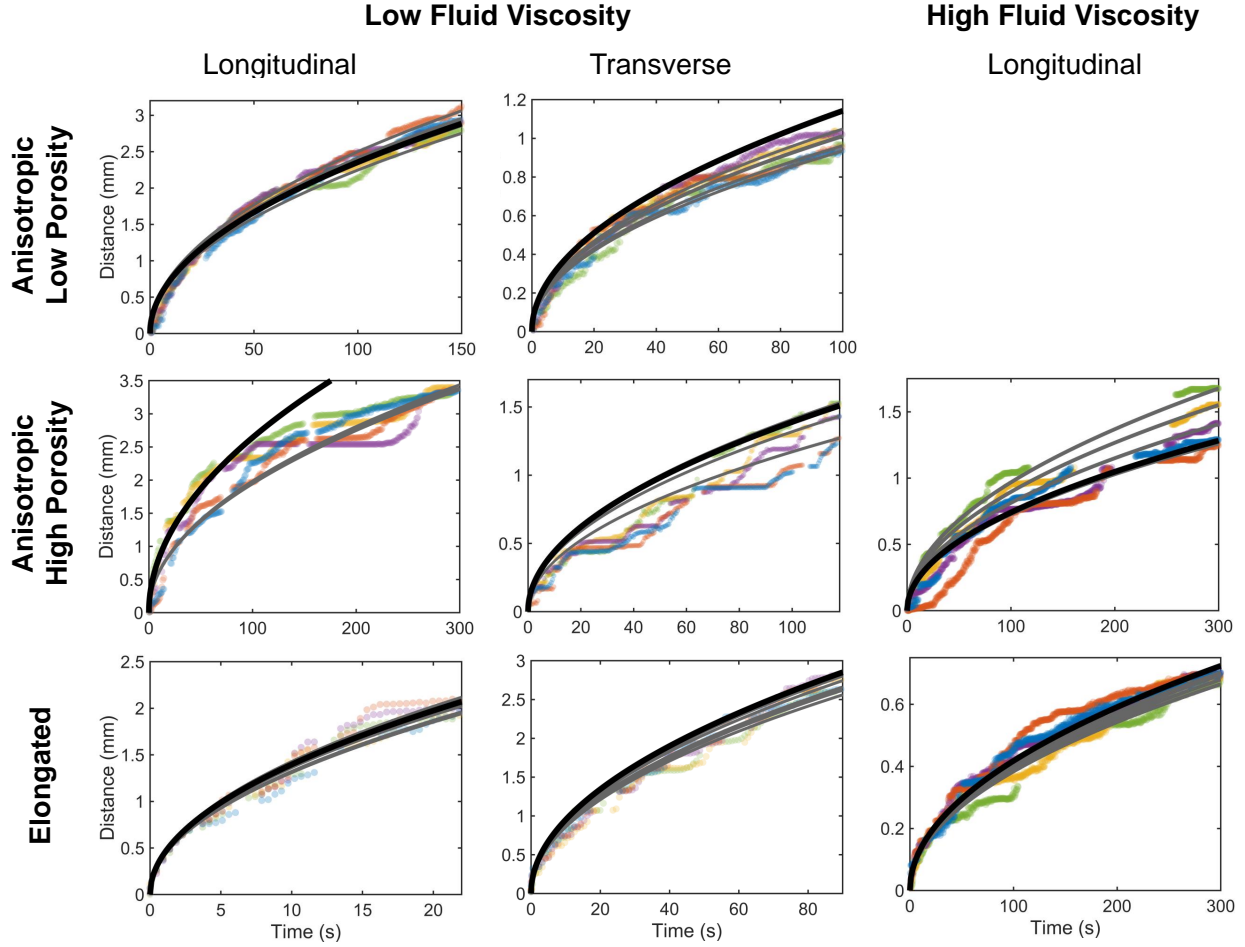
Figure 3.26: Fitting of Darcy Equation to Directionally-Dependent Flow for Anisotropic and Elongated Porous Structures. The colored markers display liquid propagation measurements; gray lines represent fluid transport considering the effective physical properties of the porous media, while the black line represents transport across-defect free structures.

outperform the wicking rate of experimental measurements while agreeing reasonably well in other cases. The similarity between K_i and K_{eff} can be attributed to exact location where the liquid advancement is measured. That is, while we consider the domain with the wicking distance closest to the liquid source (i.e., the most right of the fluorescent imaging screen), these domains are not in direct contact with the reservoir. Rather, they may be one to two domains away from the liquid source in order to prevent observing the fluorescent oversatu-
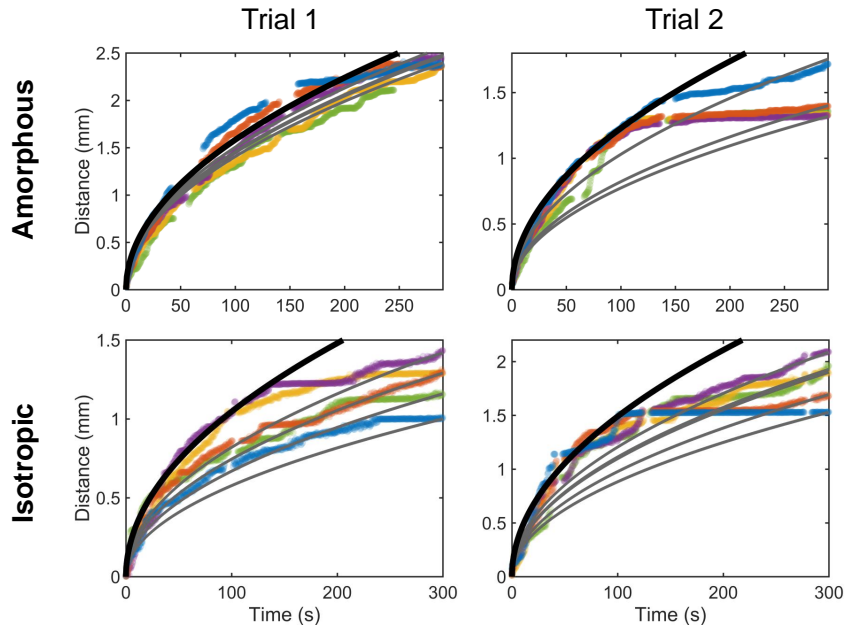
Figure 3.27: Fitting of Darcy Equation to Nondirectionally-Dependent Flow for Anisotropic and Elongated Porous Structures. The colored markers display liquid propagation measurements; gray lines represent fluid transport considering the effective physical properties of the porous media, while the black line represents transport across-defect free structures.

ration induced by the bulk liquid since the high pixel intensity from the aqueous fluorescein creates high noise-to-signal ratio, making discerning the discretized wicking behavior difficult. This lateral sample shift may cause the intrinsic permeability of the domain to be affected by a finite amount of hydraulic resistance contributed by the existing boundaries. Nevertheless, the reasonable agreement between the empirically derived propagation results and Washburn theory suggests that polycrystalline IOs also behave similarly to continuum porous media.
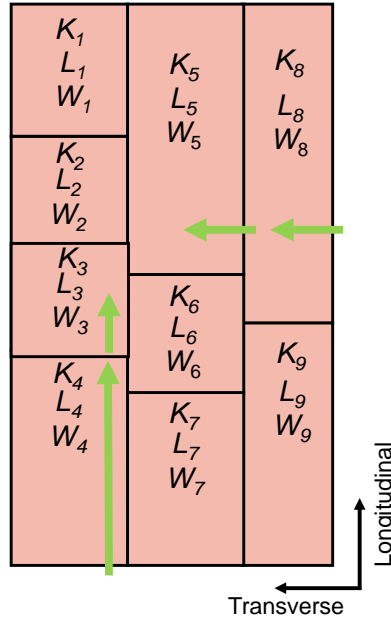
Figure 3.28: Simplified Polycrystalline Model. Individual crystalline domain comprises of an intrinsic permeability K_i and a crystalline travel distance, described as the length L_i or W_i of the domain depending on the flow orientation.

3.6 Boundary-limited Hydraulic Transport Model

While the Washburn equation models the capillary transport in media without the presence of grain boundaries relatively well, modifying the traditional equation can increase the accuracy and validity of its solution for a wider range of media, including porous polycrystals. To construct the generalized solution to predict defect-limited fluid flow, we create a simplified the model of polycrystalline porous media (Figure 3.28), such that individual domain possesses an intrinsic permeability K_i that varies as a function propagation distance h as well as a crystalline domain travel length between grain boundaries Λ that can be determined as the length L_i or width W_i of the IO domain depending on flow in the longitudinal or transverse direction, respectively. We then modify the Washburn equation to capture the

effective transport properties of porous polycrystals as described by the summation of their discretized fluid propagation events:

$$h_{tot} = \sum_{i=1}^{N} h_i = h_{i-1} + \Lambda_i + W_{GB} \tag{3.1}$$

$$t_{tot} = \sum_{i=1}^{N} t_i(h) = t_{i-1} + \frac{\mu\phi}{4\sigma} \frac{r_{eff}}{K_i(h)} \Lambda_i^2 + \left(\frac{W_G B \times \Delta t_{GB}(h,t)}{\bar{W}_{GB}} \right) \tag{3.2}$$

Where W_{GB} is the grain boundary widths. We apply the modified equation to the Monte Carlo simulation that randomly samples Λ from a normalized distribution of domain L_i or width W_i as well as W_{GB} from its normal distribution (Figure 3.7). Correlations are then fitted to the empirically derived $K_i(h)$ and $\Delta t_{GB}(h,t)$ (from Figure 3.24), which are used to determine their realistic values based on their spatial and temporal coordinates during the propagation.

The complex flow through porous media can be modeled and predicted using Monte Carlo simulations. The numerical simulation uses a stochastic and probabilistic approach to converge upon realistic liquid propagation behaviors, using the known characteristics of the pore structure geometry and fluid flow. We perform 100 Monte Carlo simulation trials to reveal various possible propagation outcomes, and the simulations closely resemble that of empirical behaviors (Figure 3.29) with errors ranging between 5% to 15% in most cases. This suggests that while the modified Washburn equations considers fluid flow only in one dimension across a three-dimensional porous polycrystal, the convergence of the Monte Carlo simulations obtains numerical solutions that can predict 3D propagation physics with relatively high level of certainty.
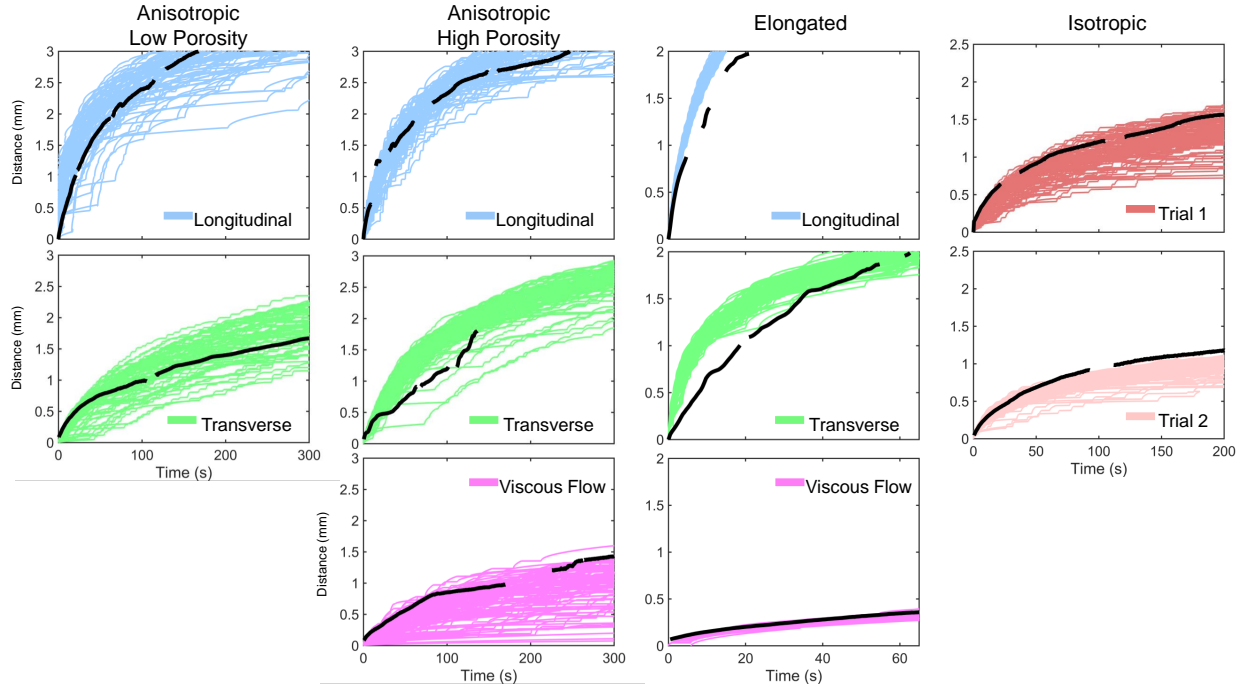
Figure 3.29: Monte Carlo Simulation Results. Using the derived characteristics of the grain domains and boundaries as well as typical hydraulic transport behaviors at the grain level, 100 Monte Carlo simulation trials provides various possible propagation results across the polycrystalline porous media. Empirical propagation results (black line) are shown in comparison to the numerical solutions (colored lines).

3.7 Conclusion

Capillary-assisted hydraulic transport through polycrystalline IOs visualized at the microscopic scale reveals the influence of domain anisotropy in facilitating preferential flow direction. This implies that the orientation of the anisotropic porous media leads to qualitative differences resulting in favorable flow patterns. Through the application of porous media in transport utility, capillary driven flow can be optimized and controlled by simply orientating the media accordingly. The grain boundaries present enormous hydraulic resistance that reduces the intrinsic permeability within individual domains in a compounding manner with increasing propagation across defects. The statistical population of grain boundaries and their associated characteristics are quantified with electron microscopy then correlate with fluorescent microscopy to determine their transport impedance behaviors at the microscale.

Using principles from Darcy and Washburn model, capillary driven transport through poly-crystalline IOs behaves similarly to that of continuum porous media.

Chapter 4

Boiling Heat Transfer Enhancement using Nickel Inverse Opals

4.1 Boiling of Three-Dimensional Microporous Structures

Phase change heat transfer is among the most effective strategies employed in applications ranging from power generation to desalination and thermal management for high-power electronics and nuclear reactors. [153, 178–182] The efficacy of two-phase cooling relies on the latent heat of vaporization associated with the working fluid. The utilization of the latent heat through nucleate pool boiling promises up to two orders of magnitude higher in heat flux dissipation in comparison to single-phase liquid cooling. [183] However, the enhancement in boiling heat transfer is interdependent upon several parameters, such as the working fluid and heated surface structure. For instance, common refrigerants, such as FC-72, possess a latent heat of vaporization of 88 KJ/Kg, which is optimal for dissipating
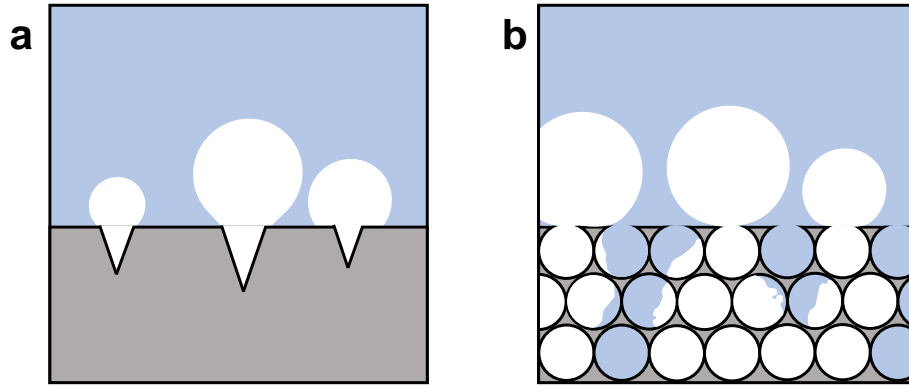
Figure 4.1: Effect of Surface Topography on Bubble Nucleation. (a) Bubbles nucleate from surface with localized cavities. (b) Porous medium induces more complex bubble nucleation process due to the interconnected pathways for liquid-vapor transport.

low heat fluxes. In contrast, water with a significantly higher latent heat of vaporization of 2400 KJ/Kg is ideal for cooling high heat flux applications.

Modification of surface features and characteristics additionally influences the boiling heat transfer performance. Extensive studies have explored various strategies to improve the boiling performance by examining different surfaces or structural architectures.[184, 185] These planar surface modifications include tuning the surface wettability,[186–190] roughness,[191] and microstructures,[192–194] which have demonstrated significant boiling heat transfer improvements by increasing the liquid-solid interfacial area where thermal energy is translated to fluid enthalpy and by controlling the bubble dynamics.[132]

A promising alternative to planar surface modifications for nucleate boiling enhancement is complex 3D microporous architectures, including metal/graphite foams and sintered particles.[55–57] These structures with highly-interconnected pores provide enormous solid-liquid interfacial area for enhanced thermal transport, microscopic pores for increased capillary pressure for passive liquid wicking, and permeable pathway for vapor to escape.[195, 196] The higher pore densities in those porous structures also provide an increase in potential bubble nucle-

ation sites. Each inherent structural characteristics of 3D microporous architectures (i.e., porosity, interfacial surface area, permeability, pore sizes, pore density) significantly affect pool boiling dynamics, but by tuning their structure features, their two-phase heat transfer can be optimized for performance breakthroughs. Figure 4.1 illustrates the representative nucleate boiling characteristics on a planar surface with discrete cavities in comparison to the 3D microporous structures with highly-interconnected pathways for liquid and vapor transport.

Despite intensive investigative efforts within the previous decades, the fundamental understandings of 3D microporous coatings on nucleate boiling behaviors remain limited.[197] The discrepancies between developed boiling theories are attributed to the porous coating's random pore packing arrangements and nonuniform pore distributions,[58] which makes it difficult to elucidate structure-property relations. Furthermore, the effects of pore sizes on the thermal and hydraulic instabilities in boiling remain unclear due to the lack of systematic investigation with uniform pore distribution. In the cases of sintered particle coatings, majority of investigations reports the ranges of particle size without mentioning the actual dimensions of the interstitial cavities.[1, 59–61] This is most salient since particle sizes are not translatable to cavity dimensions, which is needed to understand bubble nucleation dynamics in confined pore spaces. In the cases of highly-porous foam materials,[56, 198] the pore sizes, pore distributions, and localized porosities widely vary. Without the ability to decouple the multiple structural variables of a 3D microporous coating and precisely tune their characteristics, it becomes difficult to predict and optimize the exact contribution of each effects on their overall boiling behaviors.

IOs are an emerging category of 3D microporous structure that is useful to gaining fundamental insights toward boiling heat transfer due to their extreme structural regularity and tunable features.[135, 146] The highly-interconnected and porous scaffold provides enormous surface area for increased heat transfer rate, significantly increased nucleation sites, and open

permeable pathways for low-resistance liquid and vapor transport. Since IOs derived from an inverted template of monodispersed spheres, their pore and structural characteristics can be engineered to systematically investigate the effect of their pore characteristics on boiling performances. The additional capability to control the structure porosity and thickness also isolates singe-parameter effects by eliminating multiple interplaying thermofluidic mechanisms.

In this chapter, the pool boiling performance of 3D highly-ordered nickel IOs is investigated with deionized (DI) water as the working fluid at atmospheric pressure. To understand the thermophysical relationships between structural characteristics and boiling physics, the porous media thickness ($\sim$1 to 10 μm) and pore diameters (0.3 to 1.0 μm) were selectively modulated. Theoretical interpretations of the boiling phenomena inside highly-ordered 3D interconnected microporous coatings are examined by considering the hydrodynamic interactions between dynamic wetting, evaporation, structural permeability, and viscous pressure drop associated with liquid-vapor ebullition cycle within the space confinement of the microporous matrix, which are then compared to experimental critical heat fluxes (CHFs). In efforts to model the thermofluidic interactions occurring during boiling, various influencing parameters are considered, including surface wettability, structural porosity, structural durability, and bubble nucleation dynamics. This study aims to ascertain the fundamental insights toward boiling behaviors using well-regulated 3D microporous structures to provide engineering guidance toward designing highly-efficient two-phase thermal management devices for next-generation microelectronics.

4.2 Fundamentals of Boiling Heat Transfer

The efficacy of boiling can be quantified by the heat transfer coefficient (HTC), which is defined as the ratio between the applied heat flux q" and the wall superheat ΔT, which is
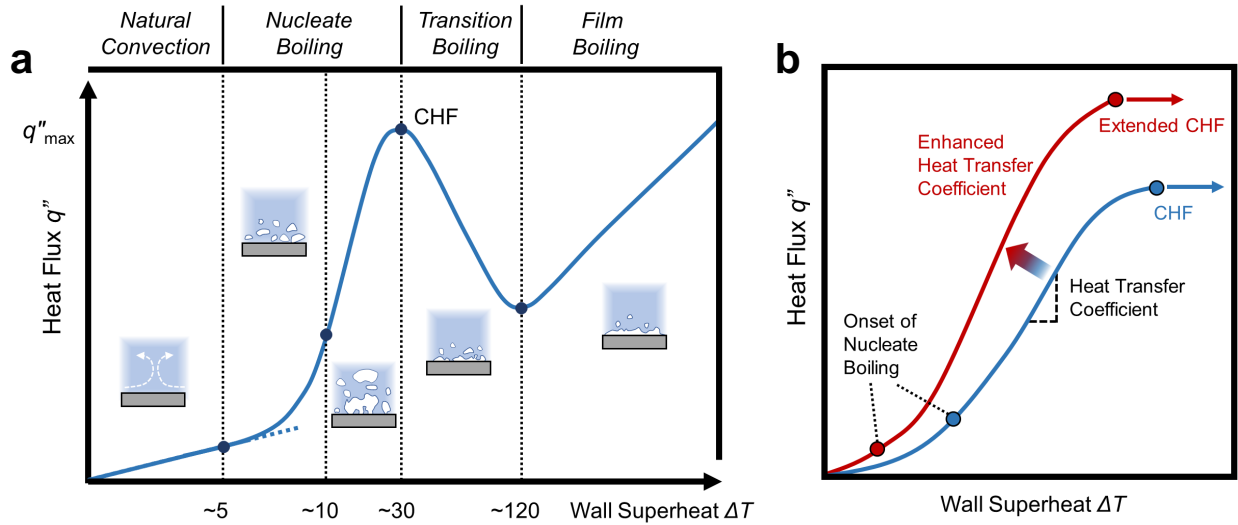
Figure 4.2: Boiling Curves. (a) Representative changes in heat fluxes as a function of wall superheat, depicting the different regimes of pool boiling. (b) The enhancement of boiling heat transfer efficacy by initiating the onset of nucleate boiling at lower wall superheat and extending the critical heat flux.

the temperature difference between the heated surface and bulk fluid $\Delta T = T_{wall}$ - T_{sat}. At a low applied heat flux, heat is transferred from the heated surface to the liquid pool through means of natural convection due to the gradient in the working fluid density (see Figure 4.2a for schematic depicting various regimes of pool boiling). The low HTC of natural convection causes the wall superheat to increase faster with heat flux. Further increase in heat fluxes beyond the natural convection causes vapor bubbles to form at the heated surface, which indicates the onset of nucleate boiling (ONB). Initially at this regime, few and isolated bubbles nucleate due to the scarce nucleation sites. As the heat flux increases, more nucleation sites become activated to transition to fully developed nucleate boiling regime. As a result, the HTC significantly improves with increasing heat flux until approaching the CHF, where the departing bubbles coalesce to form a high thermal resistance vapor barrier between the solid surface and bulk liquid (typically denoted as film boiling). Such condition prevents further heat transfer between the heated surface and the liquid pool, and

the thermal performance limits are indicated by a spike in surface temperature caused by surface burnout.

Countless investigations over the past few decades have aimed to extend the upper boiling limit as well as enhance the heat transfer performance.[59, 184, 199, 200] By exploiting the thermo-physical properties of the working fluid, surface material, and structure, several groups have attempted to initiate the ONB at lower wall superheats. This causes a higher slope increase in the boiling curve, such that the CHF is extended and the HTC (i.e., ratio of $q"/\Delta T$) is enhanced (see Figure 4.2b). These strategies can be categorized as either active (i.e., electrowetting and surfactant) [201, 202] or passive (i.e., heterogeneous surface wettability and surface microstructures) [190] in efforts to manipulate the bubble dynamics. The systematic control of both the hydraulic and vapor transport in boiling offers the optimization and balance between the competing mechanisms of surface rewetting and bubble dynamics, respectively. Among other passive approaches to increasing the CHF is the utilization of porous surface coating, which can manufactured through various techniques that include but are not limited to sintering, brazing of particles, deposition of nanofluid, electrolytic deposition, galvanizing, flame spraying, and metallic coating of porous foams.[2, 6, 185, 203–207]

4.3 Experimental Methods

4.3.1 Nickel Inverse Opal Fabrication

In contrast to IO sample preparation highlighted in Chapter 3, the scaffolding materials for the IOs in this boiling study are composed on nickel instead of copper. This is due to the higher structural durability of nickel in extreme boiling environment in comparison to copper,[133] which is later reviewed. The nickel IO sample preparation process is similar to

that of copper IO, but several modifications are made to make the sample compatible with the boiling experiment apparatus.

In brief, nickel IOs are fabricated by templating self-assembled spheres. A double-sided gold-coated silicon substrate is functionalized in 1 mM of aqueous 3-MPS for at least 24 hr to render the surface hydrophilic. The substrate is vertically submerged in a colloidal suspension (0.6% with DI water as the solvent) of monodispersed polystyrene spheres with diameters of either 0.3, 0.6, or 1.0 μm, which dictate the pore diameters. A heated base of 55 °C prevents sedimentation through gentle convective mixing of the suspension while the spheres self-assemble into opal templates as the solvent evaporates. The deposited opals are annealed in an oven at $\sim$95 °C to increase sphere-to-sphere contact area. To maintain similar porosities, sphere diameters of 0.3, 0.6, and 1.0 μm are annealed for 1, 2, and 3 hr, respectively, resulting in an IO porosity of 78% - 80%. Nickel is then electrodeposited into the void spacings between the opal template with an effective current density of 1.5 mA/cm^2 in galvanostatic mode, using a three-electrode setup in an aqueous solution of 1 M NiSO$_4$ + 0.2 M NiCl$_2$ + 0.6 M H$_3$BO$_3$. A large nickel plate and the opal sample serve as the counter and working electrode, respectively, and maintain a separation distance of $\sim$2 cm while the Ag/AgCl serves as a reference electrode. To prevent nickel deposition on the gold-coated backside of the silicon substrate, a lacquer coats the conductive surface area before the electrodeposition process. The resulting nickel-polystyrene composite structure immerses in a bath of tetrahydrofuran for a minimal of 12 hr to dissolve the sacrificial polystyrene spheres, revealing a highly-porous nickel scaffold. In the tetrahydrofuran bath, the lacquer coating on the substrate backside is also removed. The porous sample is rinsed with acetone, isopropanol alcohol, and DI water and further treated with plasma cleaning (Gatan, Solarus Model 950) for 4 min to remove remaining surface contaminants (Ar: 30 sccm, O2: 30 sccm, 50 W, 481 mTorr).
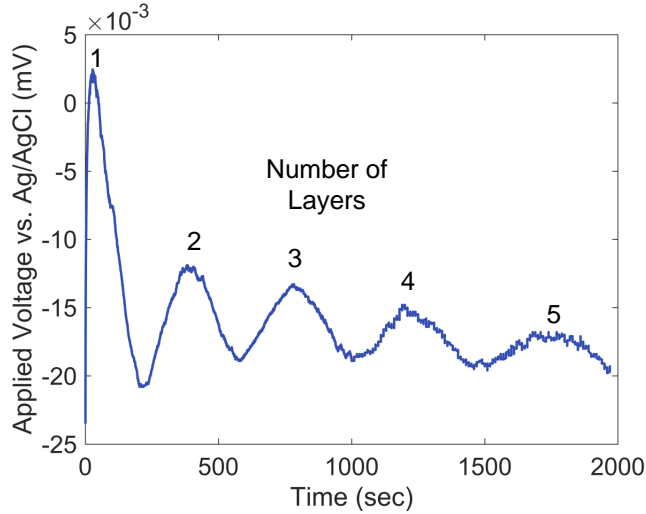
Figure 4.3: Inverse Opal Thickness Controlled through Electrodeposition. A typical galvanostatic electrodeposition characteristic of electrodeposited metals into the voids of a colloidal crystal. The current remains constant at -1.875 mA over a total seed gold layer area of 30 mm^2.

IO thickness can be controlled during the electrodeposition process. Using galvanostatic mode, the thickness of electrodeposited metal filling the cavities of the colloidal crystal template can be monitored using *in situ* potential transient measurement.[146, 208, 209] A typical galvanostatic measurement during metal electrodeposition into the voids between opal template is shown in Figure 4.3, which exhibits a voltage damping oscillation behavior. [210] The oscillations represent the varying electrochemically available surface area as the metal fills up around the curvature of the packed spheres along each opal layer.[208] That is, the smallest available surface area (i.e., the valleys in the oscillations) corresponds to the center of the spheres of that associated layer and each peak corresponds to the completion of a single IO layer. The continually decreasing damping oscillations is a result from increasingly anisotropic galvanostatic metal growth with each opal layer due to uncontrollable metal deposition and template defects such as vacancies, stacking faults, and cracks. The existence of voltage oscillations during electrodeposition suggests that the majority of the opal template is crystalline and that metal growth is fairly uniform.

4.3.2 Surface Wettability Measurement

A goniometer (Kyowa Interface Science MCA-6) pneumatically dispenses ∼15 nL of DI water to measure the droplet contact angle on the surface. Surface wettability measurements are conducted at 22 °C with ∼50% relative humidity. A high-speed camera (Photron FASTCAM SA8) records the droplet discharge at 1000 fps. An embedded software (FAMAS) automatically fits the droplet profile using half-angle method to determine the contact angle. Static contact angles are measured using sessile droplet technique, and dynamic contact angles are measured by increasing and decreasing the droplet volume to determine the advancing and receding contact angles, respectively.

4.3.3 Structural Durability of Porous Structures

From the perspective of practical applications, it is imperative to examine the feasibility of utilizing metallic IO coatings for two phase heat transfer applications. This is ensured by considering the coating durability and performance repeatability of IOs. Therefore, the structural changes endured by the nickel IOs as a result of boiling are examined. As shown in Figure 4.4, the physical morphology the nickel IOs remains unchanged before boiling and after reaching CHF. This contrasts significantly with copper IOs, which previously reported the destruction of the IO architecture with increasing boiling exposure.[133] The superior capability of nickel to maintain its structural integrity under the extreme boiling conditions suggests that nickel can be used as an ideal architectural material for IOs due to its relatively high thermal conductivity and limited oxidative states. This motivates the utilization of nickel as the scaffolding materials in this boiling performance investigation.
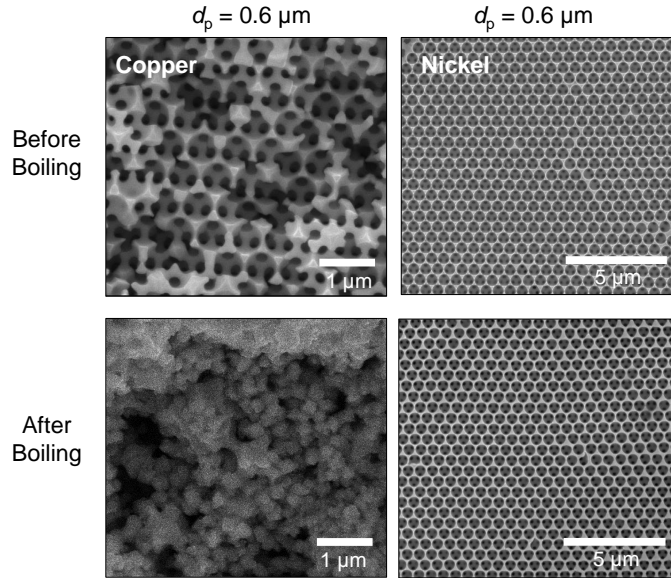
Figure 4.4: Effect of Boiling on Inverse Opal Structural Integrity. Top view SEM images of a representative inverse opal structure composed from copper or nickel. For copper structures, boiling causes significant structure damages with increasing boiling exposure. Nickel inverse opals show relatively no physical changes before and after a boiling experiment.

4.3.4 Structural Porosity Calculation

Top and cross-sectional images of the IO are captured using SEM (FEI Quanta) and post-processed with ImageJ (NIH). The via d_{via} and pore diameter d_{pore} are measured and used to determine the IO structural porosity, using a correlation derived using CFD models documented in prior work:[9, 63] $\varphi = 0.5833(d_{via}/d_{pore}) + 0.6633$. Rigorous measurements of d_{via} and d_{pore} are collected. Representative statistical distributions for each set of pore diameters are shown in Figure 4.5, which confirms the strict monodispersity of the pore diameter and uniformity of the via diameter. Using the derived correlation, the porosities of IOs are determined to be between 78% and 80% for all samples.
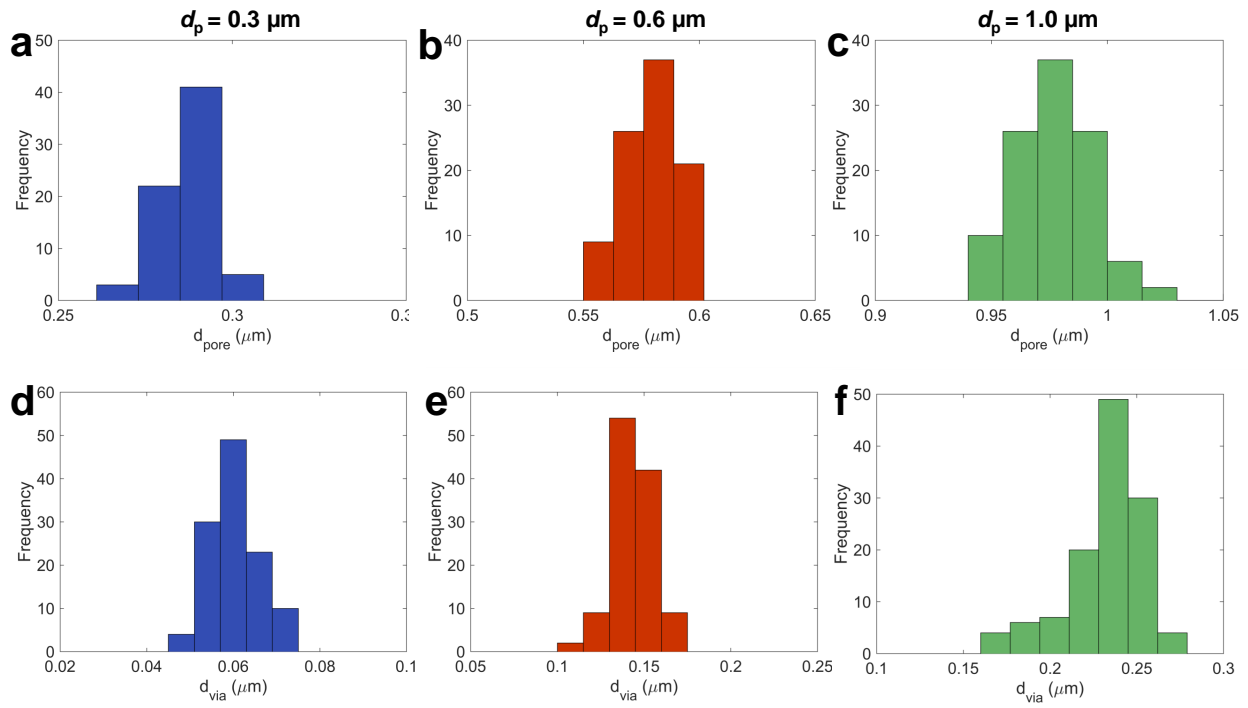
Figure 4.5: Representative Statistical Distribution of Pore and Via Diameters.
The representative frequency distributions of pore and via diameters (blue, red, and green for the expected 0.3, 0.6, and 1.0 m pore diameter samples, respectively) demonstrate the uniformity of the pore feature sizes throughout the porous media.

4.3.5 Pool Boiling Measurement

Nucleate pool boiling heat transfer of nickel IO coated surfaces is experimentally investigated with varying pore diameters and structural thicknesses. DI water serves as the working fluid, which is degassed thoroughly before experiments. At the base of the apparatus, four cylindrical cartridge heaters (Omega, CIR-2015) are placed inside a copper block (see Figure 4.6 for boiling apparatus schematics). The cartridge heaters are controlled by an AC voltage regulator (Variac Transformer), which heat the copper block to transfer the heat flux toward the mounted sample. A thermocouple located slightly above the heated sample inside the liquid pool is connected to a guard heater through a PID controller, which ensures that the pool liquid remains at saturated temperature. By tuning the electric power supply through the cartridge heaters, the applied heat flux to the sample can be slowly increased. At each heat flux, temperatures are monitored through a linked data acquisition system (LabJack U6) and recorded once reached steady state.

The surface temperature of the nickel IO (i.e., T_{wall}) is estimated using a thermal resistance model, which considers the temperature gradient along the heated copper block as well as across the mounting silver paste and the evaporated thin metallic films. Glass wool is used to surround the heated copper block such that it sufficiently insulates the copper block for one-dimensional thermal conduction toward the sample to be assumed. Additionally, a thin resin of polydimethylsiloxane (PDMS) seals the edges around the substrate to reduce parasitic heat losses to the liquid pool. The temperature gradient along the length of the copper block is measured using the four incrementally positioned thermocouples. For the temperature gradient across the mounted sample, the thermal resistance across the multiple layers of thin films are determined. Accounting for the thermal conductivity k and film thickness t of each associated layer, the thermal resistance model can be derived as

$$R_{eff} = \frac{t_{sp}}{k_{sp}} + R_{TIM} + \frac{t_{Au,bottom}}{k_{Au}} + \frac{t_{Cr}}{k_{Cr}} + \frac{t_{Si}}{k_{Si}} + \frac{t_{Ti}}{k_{Ti}} + \frac{t_{Cr}}{k_{Cr}} + \frac{t_{Au,top}}{k_{Au}} + \frac{t_{NiIO}}{k_{NiIO}} \qquad (4.1)$$
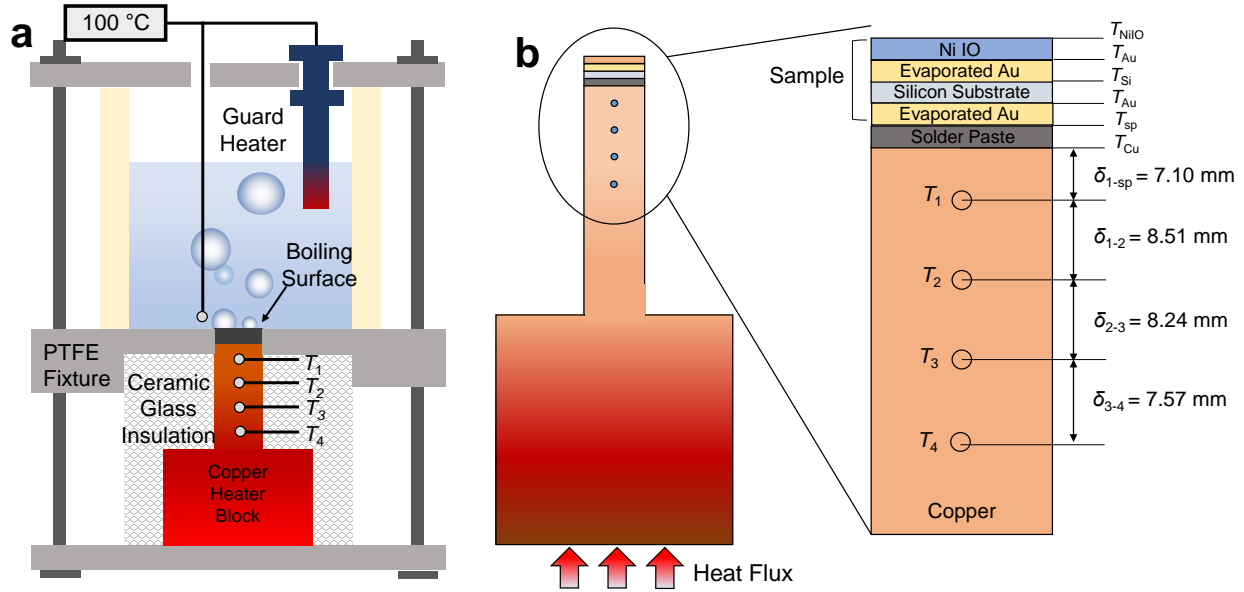
Figure 4.6: Schematic of Pool Boiling Experimental Setup. (a) A boiling apparatus with a clear enclosed chamber allows direct experimental observation. A guard heater ensures that the working fluid temperature remains saturated using a proportional integral derivative (PID) controller. Cartridge heaters inside the copper block are powered by a power supply to heat up the copper block, uniformly transferring thermal energy toward the mounted sample. The glass wool insulation surrounding the copper block reduces the heat loss to the ambient environment such that one-dimensional heat conduction can be assumed. Thermocouples are incrementally positioned below the mounted sample. A high-speed camera (not illustrated) records the bubble dynamics during boiling. The heat flux applied to the copper block can be adjusted using an electric power regulator and confirmed with a powermeter. At each applied heat flux, the temperatures are recorded at steady state. (b) Schematic of sample mounting. Four K-type thermocouples are incrementally positioned along the length of the copper block and below the sample to determine temperature gradient between T_1 and T_4. The sample consists of a silicon substrate with thin films of chromium and gold evaporated on the bottom side and titanium and gold evaporated on the top side. The adhesive layers of chromium and titanium are not schematically shown to improve schematic interpretation. A thin film of silver paste mounts the sample onto the copper block heater.

82

Materials	Subscript Notation	Thickness t (nm)	k (W/mK)
Chromium	Cr	100	94
Gold (bottom)	Au,bottom	1000	314
Silicon	Si	5×10^5	130
Titanium	Ti	15	22
Gold (top)	Au,top	100	314
Nickel IO	NiIO	$\sim$2-10 $\times$ 10^3	15

Table 4.1: Thin film characteristics used for nickel inverse opal sample preparation.

The film thicknesses t and thermal conductivity k values used are shown in Table 4.1. Chromium and titanium are used as adhesive layers for gold film deposition. Silver paste (subscript notation of sp) serves as the thermal interface material between the copper block and nickel IO sample, which has a general thickness of 7.1×10^6 nm and a thermal resistance R_{TIM} of 8.71×10^{-6} m²K/W.

Using the average measured temperature gradient across the four incrementally positioned K-type thermocouples during during steady state, the applied heat flux q" on the samples can therefore be estimated using Fourier's Law

$$q^{"} = \frac{-k_{Cu}}{3}(\frac{T_1 - T_2}{t_{1-2}} + \frac{T_2 - T_3}{t_{2-3}} + \frac{T_3 - T_4}{t_{3-4}}) \tag{4.2}$$

The surface temperature of the porous structure (T_{wall}) can then be estimated using the following

$$T_{wall} = T_1 - q^{"}R_{eff} \tag{4.3}$$

To produce the boiling curves, $q"$ is plotted against the wall superheat ($\Delta T = T_{wall} - T_{sat}$). The heat transfer coefficient HTC can be determined by relating the applied heat flux $q"$ to the associated wall superheat: HTC = $q"/\Delta T$.

The accuracy of the K typed thermocouple is within $\pm$ 1.1°C. According to the law of propagation of uncertainty, the maximum uncertainties associated with the heat flux and HTC are $\pm$ 7.26 W/m^2 and $\pm$ 10.28°C, respectively.

A clear boiling chamber allows for visual monitoring of nucleating bubble dynamics. A high-speed camera (FASTCAM Mini AX50) captures bubble nucleation, growth, and departure at 2000 fps at 1024 $\times$ 1024 resolution. The departing bubble diameters and maximum base diameters are observed from unobscured nucleation sites near boiling incipience. The examined bubbles do not coalesce with other nucleation sites during the bubble growth and departure cycle.

4.4   Influencing Parameters and Behaviors

4.4.1   Water Vapor Permeability through Inverse Opal

A computational fluid dynamics (CFD) simulation models (ANSYS Fluent, Version 17.1) predicts the fluid permeability of a inverse opal of various pore diameters and porosities. Due to the continuous solid matrix with open interconnected pores, the flow through the pore network can be modeled using a repeating unit cell. With a representative unit cell of an inverted face centered cubic (FCC), an inlet flow at constant velocity (through the left face) with an outlet pressure (at the right face). The other faces of the unit cell pose symmetric boundary conditions to represent the periodicity of the unit cell (see Figure 4.7).

Using SIMPLE scheme for pressure-velocity coupling, the pressure gradient ΔP through the unit cell is determined and applied to Darcy law to predict the permeability K

$$Q = \frac{KA}{\mu}\frac{\Delta P}{L} \qquad\qquad (4.4)$$

where Q is the volumetric flow rate, A is the cross-section area of the medium, μ is the viscosity of the fluid, and ΔP is the hydrostatic pressure drop, and L is the length of the sample in the flow direction. The permeability of water vapor through an inverse opal unit cell is displayed in Figure 4.8 across a range of pore diameters and porosities (78% - 83%). The permeability of liquid water is shown for comparison, which shows approximately an order of magnitude lower in permeability for any given pore diameter. High mesh number is used to minimize mesh size effects in the calculations. For instance, the mesh number used in calculating for a unit cell with pore diameter of 1.2 μm is 393,320.

4.4.2 Surface Wetting Behaviors of Inverse Opal

The interdependency between surface wettability and bubble nucleation dynamics contribute significantly to the boiling heat transfer efficacy.[184, 189] Hydrophilic surfaces (i.e., surface with static contact angle of less than 90°) and superhydrophilic surfaces (i.e., contact angles approaching zero) improve surface rewetting and can delay the CHF. However, they exhibit poor heat transfer performance at lower heat fluxes in the nucleate boiling regime. In contrast, hydrophobic surfaces (i.e., surface with static contact angles of greater than 90°) and superhydrophobic surfaces (i.e., surface with static contact angles of greater than 150°) induce ONB at lower wall superheat and activates higher nucleation site densities at low
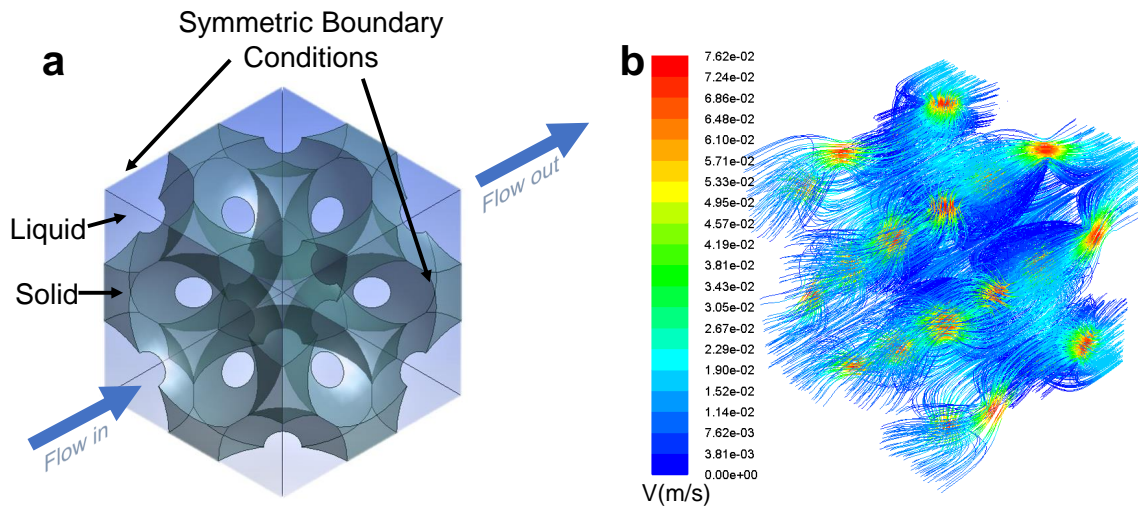
Figure 4.7: Permeability calculation and simulation based on fluid transport through an inverse opal. (a) Unit cell of inverse opal with geometry and boundary conditions. The fluid is introduced using 0.01 m/s velocity inlet (left face) and pressure outlet boundary conditions(right face). The other surfaces are set to have symmetric boundary conditions. The gray is the solid domain and blue is the liquid domain. (b) A representative modeling of the fluid velocity streamlines inside an inverse opal structure.
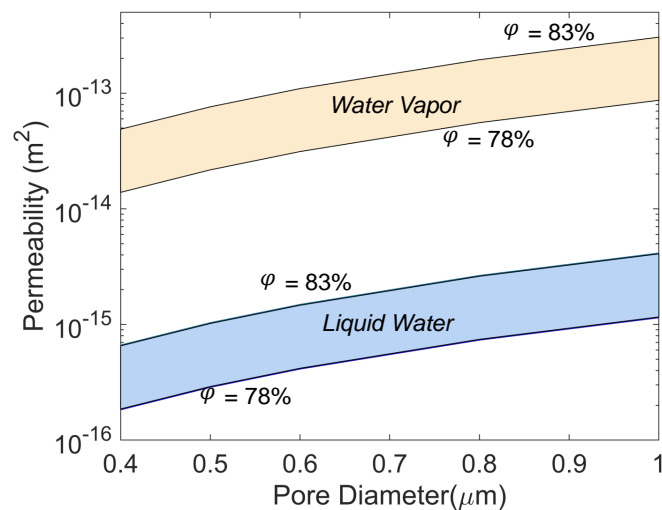
Figure 4.8: Liquid and Water Vapor Permeability The permeability of liquid water (blue band) and water vapor (light orange band) for inverse opals with a range of pore diameters and porosities.
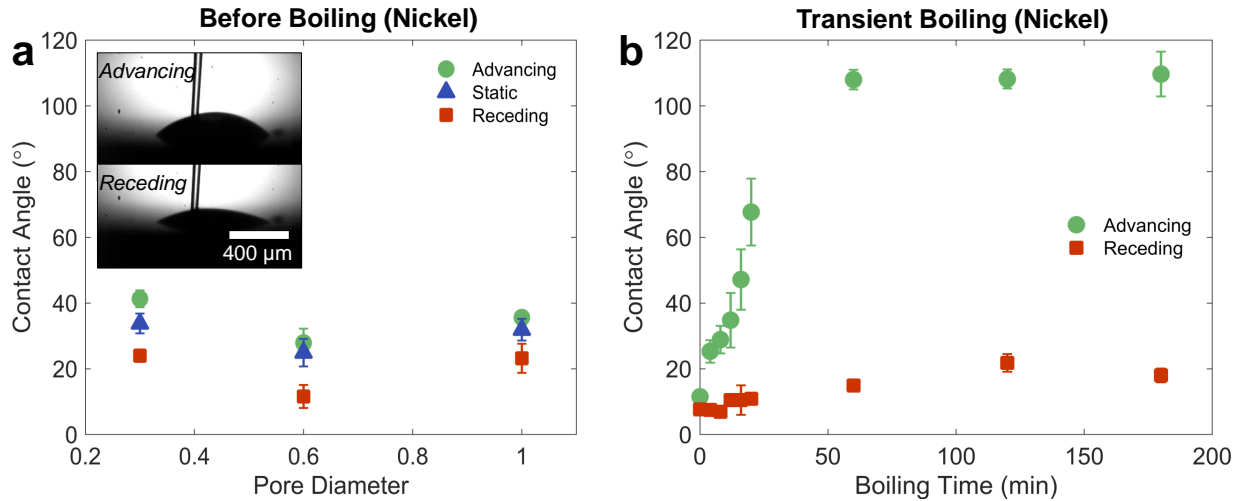
Figure 4.9: Surface Wettability of Nickel Inverse Opals from Boiling (a) Before boiling, the nickel inverse opals are hydrophilic with contact angle hysteresis of ∼20°, irrespective of their associated pore diameters. (b) The surface wettability of the inverse opal structure is periodically measured throughout after being exposed to boiling condition. The surface quickly oxidizes and finally becomes nonwetting at ∼110° and ∼20° in advancing and receding angle, respectively, within the first hour of boiling. Since boiling experiments typically exceed one hour, the nickel inverse opals can be reasonably considered to be hydrophobic within the time scale of a boiling measurement.

heat fluxes, resulting in efficient heat transfer but cause premature film boiling at high heat fluxes.

For hydrophilic *porous* media, the ebullition cycle documented in previous reports discuss a continuous liquid wicking driven by the pore capillary force to rewet the heated surfaces.[182, 191] However, this assumes the surface energy of the microporous medium remains constant throughout the boiling process (i.e., highly wetting), which has been rarely validated. This is especially important for highly conductive metallic surfaces (e.g., copper and nickel) often used in two-phase heat transfer studies, which are prone to oxidize and change in surface energy.

To understand the transient surface wettability of nickel IOs during pool boiling, water contact angle of the samples before and periodically over a span of 3 h under boiling environment are measured. Prior to the boiling measurements, the nickel IOs are plasma cleaned, which
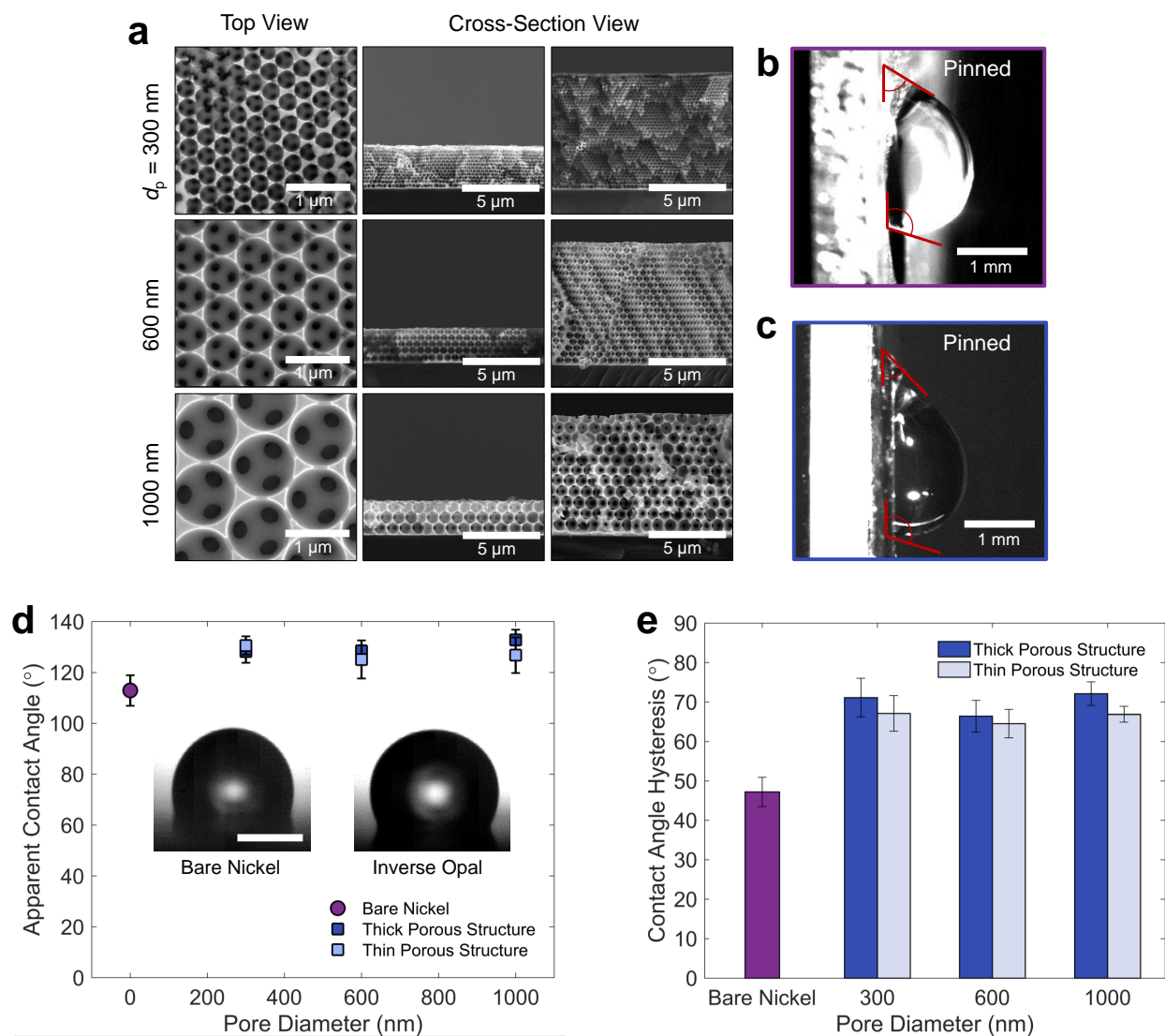
Figure 4.10: Droplet Impingement on Nickel Inverse Opals (a) Morphology of nickel inverse opals with various combinations of pore diameters (300, 600, and 1000 nm) and structural thickness (~ 3 and ~ 9 μm) as shown with top and cross-sectional SEM images. Water droplet remains strongly pinned to both (b) flat and (c) porous nickel even at 90° tilt. (d) Apparent contact angles from sessile droplet technique for inverse opals with various pore diameters and structural thicknesses as well as a flat nickel plate. The insets show representative camera captures of hydrophobic droplet profile. Scale bar is 200 nm. (e) While the surfaces are hydrophobic, the droplets remain impinged on the surfaces, leading to a significantly high contact angle hysteresis, irrespective of pore diameters or thicknesses.

show hydrophilic characteristics with receding and advancing contact angle of $\theta_{rec} \approx 15°$ and $\theta_{adv} \approx 40°$, respectively (Figure 4.9a). Afterward, the porous nickel is placed into a glass beaker with saturated boiling DI water to mimic the pool boiling condition. The water is maintained at 100 °C with a PID controller, and the beaker surrounding is insulated to reduce heat loss. At various time increments, the sample is removed from the boiling liquid pool and dried with compressed air before measuring the dynamic contact angles with a goniometer. As shown in Figure 4.9b, the relatively hydrophilic surface rapidly increases in hydrophobicity with $\theta_{adv} \approx 110°$ after the first hour before stabilizing at $\theta_{adv} \approx 120°$ after 3 h. The rapid changes in wettability can be attributed to surface chemistry and energy modification caused by metallic oxidation since no physical changes in the porous features are observed before and after the boiling process (Figure 4.4).[63, 133] Since the advancing contact angle quickly increases to ∼120° within a few hours, the nickel IOs are assumed to be nonwetting during the span of a typical boiling experiment. It is noteworthy to mention that the receding contact angles θ_{rec} remain consistently low at ∼20° before and during the boiling exposure. This suggests strong liquid impingement upon the microporous surfaces, which is consistent with previous finding that demonstrated that water droplets remain pinned to nickel IOs even when the surface is tilted to 90° despite possessing hydrophobic static contact angles of 130°, irrespective of pore diameter or thickness (see Figure 4.10).[137] The wetting characteristics of nickel IOs presented here resemble those of parahydrophobic surfaces (i.e., high static contact angle and high contact hysteresis).[211] The strong adherence of the droplet to the IO surface indicates a Wenzel wetting state, as notably described when the droplet sinks into the microporous surface (see Figure 2.4).[212] In this dynamic wetting state, the three-phase contact line remains pinned to the textured surface, and bubbles grow with a fixed base diameter and liquid receding at the receding contact angle, mitigating vapor spreading across the surface and delaying CHF. Before the incipience of boiling, the liquid from the pool reservoir impinges and fills the cavities of the IOs, displacing the entrapped air through their highly-interconnected cavities and effectively
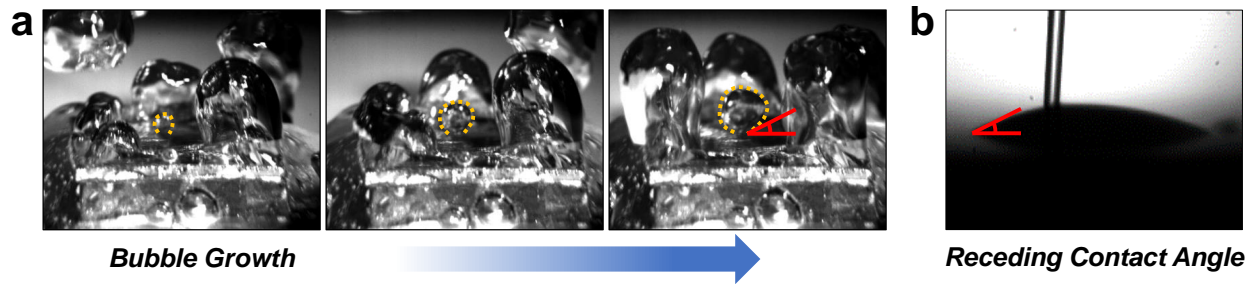
Figure 4.11: Bubble Growth with Receding Contact Angle. (a) High-speed recording showing small receding angle during bubble growth on a nickel inverse opal surface, and (b) image showing similar droplet receding contact angle on the same surface.

wetting the entire thickness. During nucleate boiling, the Wenzel wetting state can promote liquid to fill the pore spaces left behind by the escaping bubbles by the Laplace pressure. The liquid rewetting mechanism promoted by the Wenzel state presented here is supported from the observed boiling behaviors. That is, typical hydrophobic and superhydrophobic surfaces can initiate boiling incipience more efficiently at lower heat fluxes, but their inability to rewet the surfaces quickly lead to premature film boiling at moderate to high heat fluxes. However, the sustained nucleate boiling of the hydrophobic nickel IOs presented here strongly suggests that the dynamic wetting (i.e., Wenzel) is capable of maintaining a stable liquid film inside the porous structure.

4.4.3 Effect of Receding Contact Angle on Bubble Dynamics for Porous Surfaces

The surface wetting behaviors of nickel IOs have a significant impact on their vapor formation characteristics. The bubble growth and departure dynamics are studied using high-speed recording near boiling incipience when unobstructed views of isolated bubbles are available. As bubbles nucleate and grow, their contact line spreads outward and the liquid recedes away, which closely resembles the contact angle of a receding droplet at the early stages of bubble growth when buoyancy have minimal distortion effect on the bubble shape. Figure 4.11

demonstrate the similarity between the bubble growth characteristics and droplet receding contact angles. Therefore, the receding contact angle has been suggested to be an important factor in influencing bubble growth dynamics.[213]

Representative bubble growth characteristics on nickel IOs are shown in Figure 4.12. Due to the low contact angle of liquid receding away from the growing bubble, the bubble base diameter remains small during the bubble growth. This inhibits the spread of insulating vapor across the surface and allows the surfaces to continue undergoing nucleate boiling. As the bubble grows, the rising bubble shape becomes distorted by the increasing buoyancy forces. Once the bubble reaches a critical size when the buoyancy forces exceed the surface tension forces, the bubble then departs from the surface by pinching off above it, leaving a small vapor bubble at its site. The ebullition cycle repeats.

The prevention of vapor film spreading and bubble coalescent during vapor formation is supported by the low liquid receding contact angle, causing the bubble departure diameter and base diameter to remain relatively small. In addition to bubble departure diameter and base diameter, the thermodynamic efficiency of boiling as described by the heat transfer coefficient is also influenced by the bubble departure frequency, which is found to be inversely proportional to the departure diameter. [214] High-speed recordings of the bubble departure in this study are analyzed near boiling incipience, and the results are shown in Figure 4.13. The maximum base diameters of bubble during the early growth period (before buoyancy causes the bubble to pinch off the surface) average approximately 0.52 ± 0.09 mm.

4.4.4   Bubble Transport Behaviors Inside a Porous Medium

The bubble dynamics within pool boiling rely on the interdependency of liquid replenishment and vapor generation. That is, liquid rewets the heated surfaces as vapor bubbles grow and depart from the surface. The liquid contributes to phase change through evaporation and
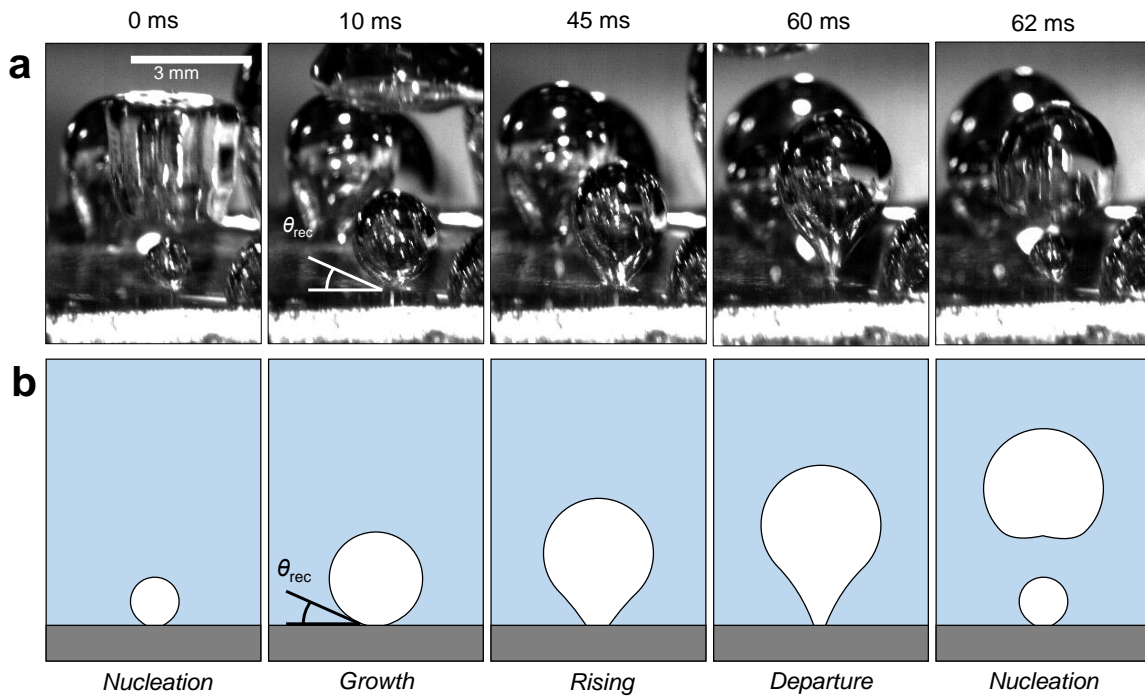
Figure 4.12: Bubble Growth and Departure Characteristics on Hydrophobic Nickel Inverse Opals. (a) The temporal evolution of bubble nucleation through departure during an ebullition cycle as captured from a high-speed recording. (b) The schematics illustrate the representative ebullition cycle. The recording shows a bubble growth with low receding contact angle on the hydrophobic nickel inverse opal surface while the triple-phase contact line remains pinned and prevents vapor from spreading across the surface. As the bubble grows larger, buoyancy begins to distort the bubble shape by pulling it upward; once buoyancy forces exceed the surface tension forces, the bubble departs from the surface. A smaller bubble nucleates at the same location, and the ebullition cycle continues.
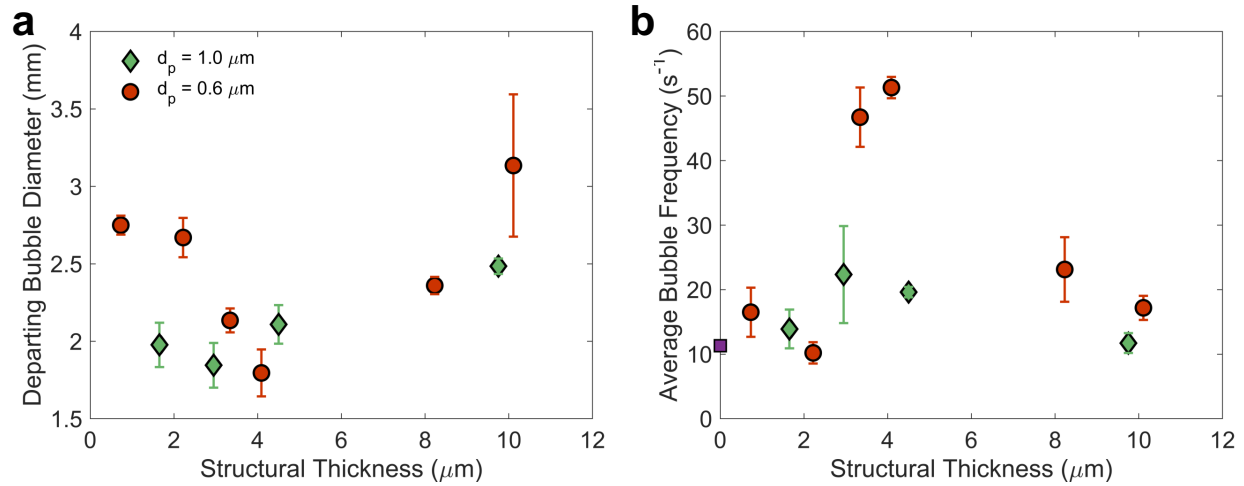
Figure 4.13: Bubble Departure Characteristics. High-speed recordings of departing bubble characteristics are post-processed to measure the (a) departing bubble diameter and (b) bubble frequency near the boiling incipience. The average departing bubble diameter of silicon is 6.72 ± 0.47 mm (not shown), and the average bubble frequency of silicon is shown in (b) as the purple square marker.

bubble formation. The ebullition cycle continues at relatively low heat fluxes until the rate of bubble nucleation and departure outpaces that of liquid rewetting with increasing heat fluxes or at CHF, during which an insulating vapor film coats the entirety of the porous structure.

Below the base of the growing bubble, evaporation of thin liquid film can contribute to the bubble growth and phase-change heat transfer mechanisms. When the pores are filled with liquid and evaporation occurs at the top of the structure, the maximum rate of evaporation can be achieved.[182] Within the IO structure, the general region filled with liquid where evaporation most likely to occur can be denoted as the "evaporation regime," as illustrated in Figure 4.14. However, the liquid infiltration through the porous structure (even under the Wenzel dynamic wetting state) during nucleate boiling is often nonuniform and unpredictable due the violent bubble extraction through the tortuous confinement of 3D microporous media, which may inhibit permeable pathways for liquid replenishment to rewet the surface. The effect of nonuniform liquid rewetting on boiling heat transfer performance is especially
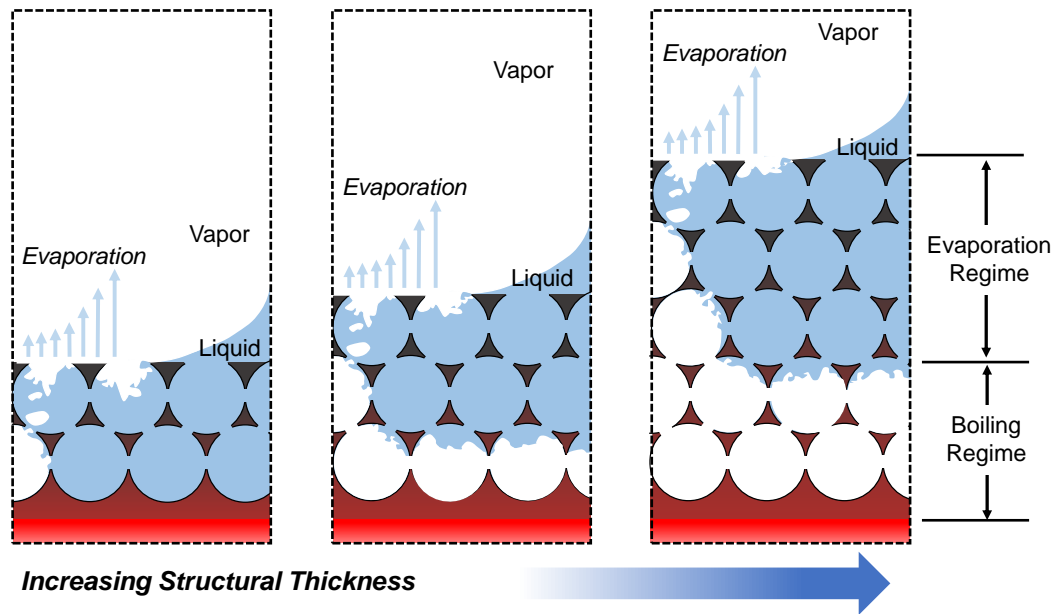
Figure 4.14: Hydrodynamic Mechanisms Inside the Confined Cavities of a Porous Medium During Nucleate Boiling. Illustrations of liquid-vapor formation and transport inside the inverse opal with varying structural thicknesses. At lower structural thicknesses, the impinged liquid can easily penetrate the entirety of the structure to provide liquid replenishment, which can contribute to phase-change heat transfer through evaporation to the bubble on the top surface. This general region is denoted as the evaporation regime. Nucleate boiling often occurs near the porous structure base. As the bubble grows, it escapes upward across the thickness of the structure. Within larger structural thicknesses, the vapor travels a longer distance, during which the bubbles continue to grow and occupy more of the interconnected pores, limiting the liquid permeable pathways. This prominent region at the porous structure base where bubbles nucleate and coalesce is denoted as the boiling regime.

poignant with increasing wicking media thickness. While increasing the microporous media increases the interfacial surface area for a higher phase-change rate, beyond a certain optimal thickness can cause the escaping bubbles to travel a greater distance across the thickness of the microporous media, during which the vapor pockets continue to grow and occupy more of the interconnected pore cavities and block the liquid permeable pathways. The partial dryout caused by the coalescent of vapor pockets will mostly occur near the base of the microporous media where the heat source is the greatest and can generally be denoted as the "boiling regime," as illustrated in Figure 4.14). The complexity of boiling within 3D interconnected microporous architecture can be further modeled by fundamental liquid-vapor interfacial transport behaviors as a function of structural thickness.

4.4.5   Theoretical Evaporation and Vapor Transport Limits

Advection heat transfer dominates as liquid impinges and permeates through the heated surfaces of the porous medium. In addition to surface advection, the thin-film evaporation between liquid-vapor interfaces contributes to the overall heat and mass transfer as a result from the liquid-vapor phase change in pool boiling. The evaporation of the liquid can estimate the overall CHF $q"_{CHF,evap}$ by considering the baseline boiling heat transfer contribution from the plain surface represented as $q"_{CHF,plain}$ as well as the heat transfer enhancement gain from the microporous coating denoted as $q"_{evap}$

$$q"_{CHF,evap} = q"_{CHF,plain} + q"_{evap} \tag{4.5}$$

When liquid evaporates and contributes to vapor formation, the maximum evaporation rate per bubble within the evaporation regime can be described as [182]

$$\dot{M}_{evap} = \pi d_b \int_0^{\delta_w} \dot{M}"_{evap} \varphi d\delta \tag{4.6}$$

where φ is the structural porosity, δ_w is the thickness of the evaporation regime, d_b is the bubble base diameter in contact with the porous surface, and $\dot{M}''_{evap}$ is the evaporation mass flux between the liquid-vapor interfaces within the porous medium. The derivation of $\dot{M}''_{evap}$ assumes that evaporation occurs at a stationary liquid-vapor interface that is maintained by steady state heat conduction across the porous medium.[182] The resulting CHF contributed by evaporation occurring at the top of the IOs can be estimated as

$$q''_{evap} = \frac{\dot{M}''_{evap} h_{fg}}{2d_b^2} \tag{4.7}$$

where h_{fg} is the latent heat of vaporization.

The evaporation of liquid to form vapor bubbles can also be initiated within the cavities of the porous medium as the wall temperature exceeds the saturation temperature. As the vapor escapes upward from the IO base, the bubble exudes a maximum viscous pressure loss Δp_v on the system that can be determined using Darcy law as [215]

$$\Delta p_v = \frac{\mu_v \delta U_v}{K_v} \tag{4.8}$$

where μ_v is the vapor dynamic viscosity, δ is the structural thickness, U_v is the vapor velocity, and K_v is the vapor permeability through the porous medium. Based on the CFD simulation results presented in Section 4.4.1, the water vapor permeability K_v through a unit cell of IO is an order of magnitude higher than the liquid permeability K_l for a given pore distribution. Despite the high permeability, the vapor transport mechanism is often hindered by partial liquid-vapor blockage within the microporous structure. As a result, the mixture of liquid-vapor transport is limited by the liquid permeability K_l before approaching CHF. Therefore, by equating K_v to K_l, a more accurate contribution of the liquid-vapor transport mechanisms toward the boiling limit can be represented. The vapor formation and blockage often occurs near the base of the wick where the heat flux is the highest. As the vapor escapes upward

96

across the porous medium with uniform pore diameter d_{pore}, the vapor velocity of U_v can be estimated as

$$U_v = \frac{q"}{h_{fg}\rho_v}$$ (4.9)

Before approaching CHF in pool boiling, the transport of the bubble through the porous medium causes a viscous pressure loss, which is expected to equal to the increased vapor pressure experienced at the wall superheat.[216] The vapor pressure drop Δp_v can be determined over the wall superheat ΔT to express the pressure-temperature relation along phase boundaries,[155] using the Clausius-Clapeyron equation [217]

$$\frac{\Delta p_v}{\Delta T} = \frac{h_{fg}}{T_{sat}\Delta v}$$ (4.10)

where Δv is the specific volume difference between liquid and vapor phases, represented as

$$\Delta v = \frac{\rho_l - \rho_v}{\rho_l \rho_v}$$ (4.11)

where T_{sat} is the saturation temperature, set equal to 372 K. The combination of Equation 4.9 and 4.10 estimates the CHF by considering the vapor transport through the porous medium with a determined structural thickness δ [155]

$$q"_{CHF,vapor} = \frac{K_l h_{fg}^2 \rho_l \rho_v^2 \Delta T}{\delta \mu_v T_{sat}(\rho_l - \rho_v)}$$ (4.12)

4.5 Results

4.5.1 Silicon as a Reference Boiling Surface

We examine the boiling efficacy of bare silicon as a reference surface to demonstrate the heat transfer enhancement contributed by the IO surfaces. To determine the optimal configuration to mount the sample onto the copper block heater, two setups are investigated. In the "edge mounting" configuration (Figure 4.15), the PDMS sealant surrounds the edges of the sample without overlapping onto it; this produces CHF_{Si} of 47.0 and 28.6 W/cm^2 and maximum HTC_{Si} of 2.11 and 0.91 W/cm^{2}K in two separate trials (yellow markers in Figure 4.16). The variances in boiling performances from this mounting configuration may derive from the difficulty of consistently securing the tested surface onto copper block heater without creating any gaps between the PDMS adhesive and silicon sample, which serve as unwanted nucleation sites. By employing the "top mounting" configuration (Figure 4.15), such that the PDMS partially covers the surrounding edges, gaps are minimized, which produces lower but consistent boiling performances (CHF_{Si} of 18.9 and 18.4 W/cm^2 and HTC_{Si} of 0.55 and 0.52 W/cm^{2}K, as shown in Figure 4.16 by magenta markers). Due to the experimental consistency, all of the nickel IOs in this study are secured using the "top mounting" configuration in order to minimize unwanted nucleation sites and obtain consistent results between samples. However, when normalizing the boiling performances of the nickel IOs to those of bare silicon, we normalized them to the highest CHF and HTC values from the "edge mounting" configuration to ensure a conservative estimation of the heat transfer enhancement. This is because the CHF of our polished silicon is lower than those presented in literature, which is typically CHF_{Si} = 66-89 W/cm^2 and HTC_{Si} = 1.66-3.89 W/cm^{2}K for the same boiling conditions: water as the working fluid at atmosphere pressure (see Table 4.2).[192, 218–221] We believe our discrepancy from literature's values is based on how the sample is mounted onto the heater, which varies between studies, and we here
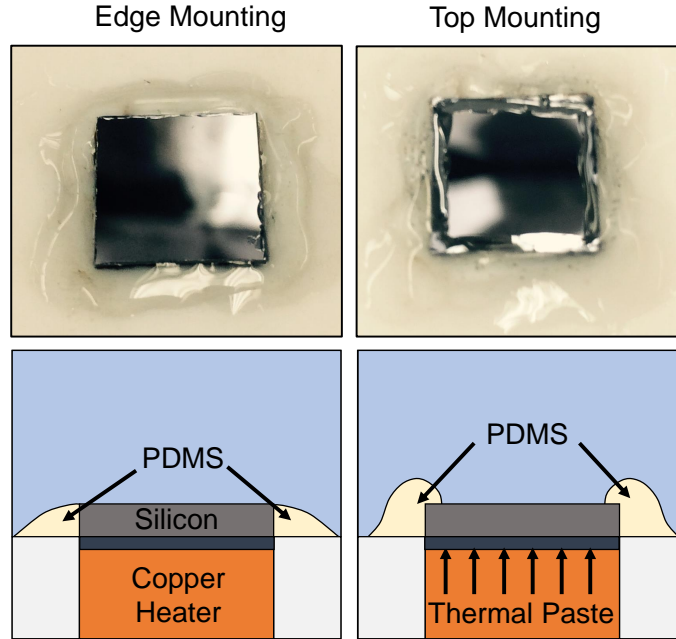
Figure 4.15: Mounting of Surfaces for Boiling Measurements Optical and schematic images of the sample mounting configurations on the copper block heater.

demonstrated that these variances in mounting configurations can alter the heat transfer performance. Nevertheless, since our HTC_{Si} is within the range of prior works, we expect that by normalizing the HTC of nickel IOs to that of bare silicon, we can provide a basis for reasonable comparisons between the boiling efficacy of different 3D porous media.

Plain	Fluid	Pressure (atm)	CHF (W/cm^2)	HTC (W/cm^{2}K)	Cite
Si	Water	1	82	2.64	[218]
Si	Water	1	79	3.89	[192]
Si	Water	1	89	3.33	[219]
Si	Water	1	75	2.01	[220]
Si	Water	1	66	1.66	[221]
Si	Water	1	47	2.11	this study

Table 4.2: Boiling performances of plain silicon as reference surfaces.
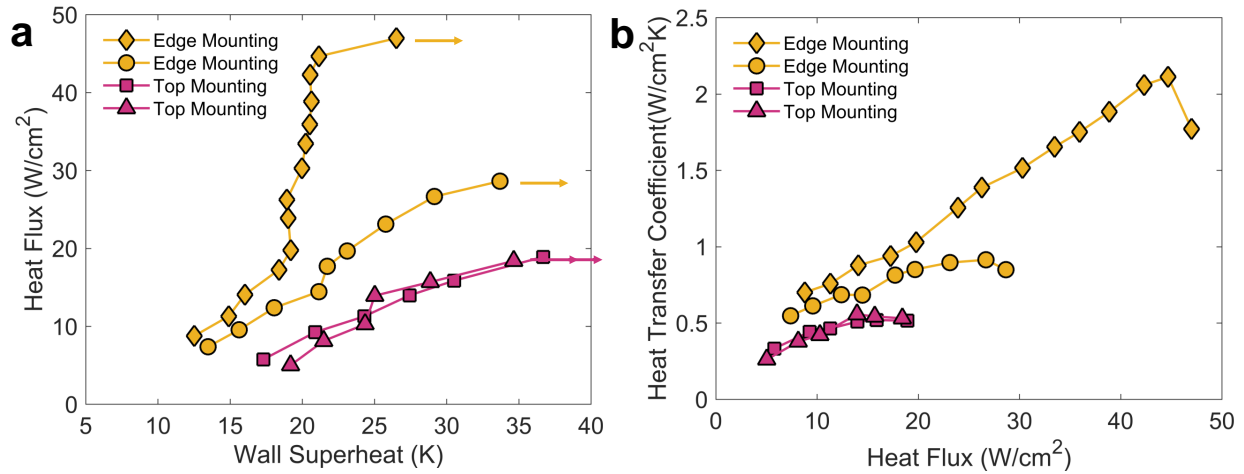
Figure 4.16: Boiling Heat Transfer of Polished Silicon Surface. (a) The boiling curves and (b) the heat transfer coefficient as a function of heat flux for polished silicon with varying mounting configurations (two separate trials for each configuration). The boiling performance of polished silicon is used as a reference to estimate the boiling enhancement contributed by the porous surface.

4.5.2 Thickness-dependent Boiling Performances

With the objective of elucidating the thickness-dependent boiling performances, nickel IOs with varying structural thicknesses δ for samples of 0.6 and 1.0 μm pore diameters are prepared, as shown in the cross-sectional SEM images in Figure 4.17. The detailed microscopic images display the 3D microporous boiling surfaces exhibiting both pore monodispersity and periodic pore packing. The structural porosity φ of the IO film is confirmed to be maintained at 78% - 80%. The associated boiling curves with the heat flux plotted as a function of wall superheat as well as HTC as a function of heat flux for structural thickness-dependent IOs are presented in Figure 4.17b-c (for 0.6 μm pore diameters) and Figure 4.17e-f (for 1.0 μm pore diameters). The results demonstrate that both the CHF and HTC initially increase with increasing structural thickness until the optimal thickness (δ = 3 - 4 μm). Further increases in the porous structure thickness lead to a deterioration in both CHF and HTC. Such general trend exists both sets of pore diameters, suggesting that boiling performance can be optimized by selecting the appropriate structural thickness for each pore diameter. In
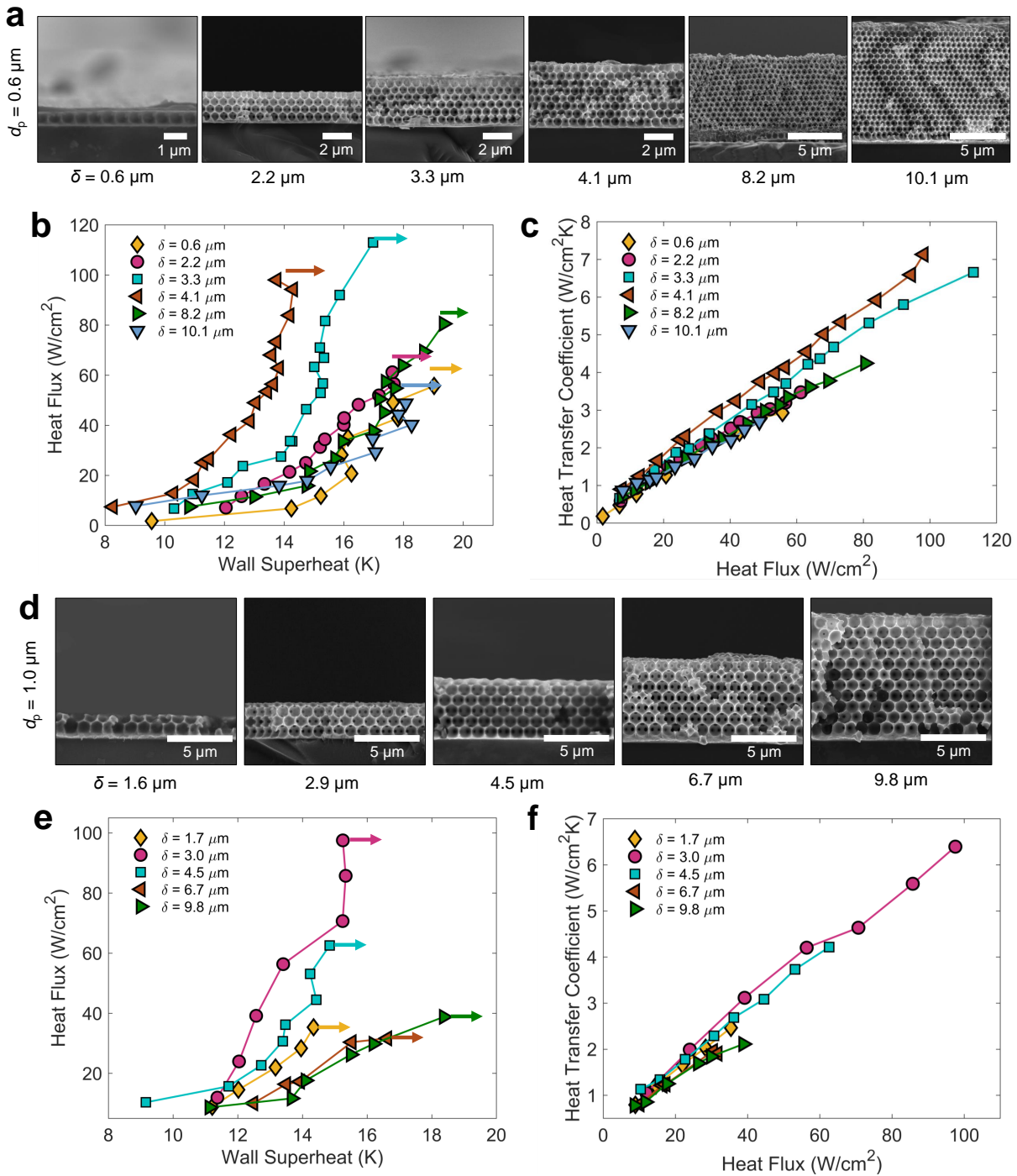
Figure 4.17: Structural Thickness-dependent Pool Boiling Performance. Cross-sectional SEM images of nickel inverse opals with varying structural thickness (between ∼1-10 μm) for pore diameter of (a) 0.6 and (d) 1.0 μm. The boiling curves of (b) 0.6 and (e) 1.0 μm pore diameter samples. The horizontal arrows indicate the CHF. The heat transfer coefficient as a function of heat flux for (c) 0.6 and (d) 1.0 μm pore diameter samples. The inverse opals possess a porosity of 80%.
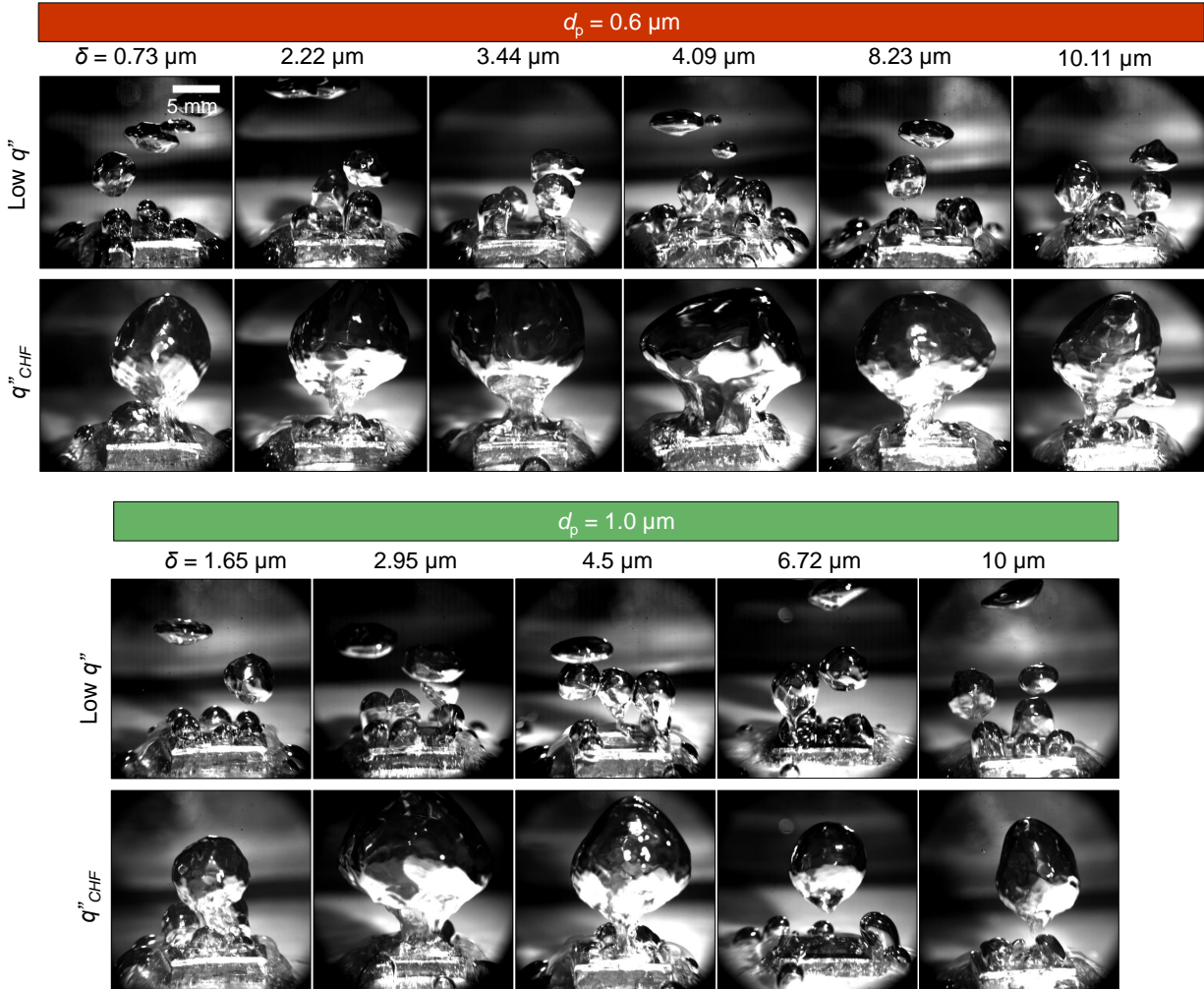
Figure 4.18: Bubble Nucleation Characteristics at Low and Critical Heat Flux.
At varying structural thicknesses δ, representative departing bubble characteristics are captured using high-speed camera for the pore diameters of 0.6 and 1.0 μm at the incipience of boiling (denoted as low $q"$) and at the critical heat flux (denoted as $q"_{CHF}$).

terms of heat transfer coefficient, the optimal thicknesses for 0.6 and 1.0 μm pore diameters are ~3 and 4 μm, respectively, while the optimal thickness that supports high critical heat flux is ~3 μm for both sets of pore diameters. The bubble departure characteristics for the thickness-dependent study are displayed in Figure 4.18 at low and critical heat fluxes.

Taking into account the liquid-vapor transport behaviors inside a porous medium, the evaporation limit (Equation 4.5) and vapor transport limit (Equation 4.12) are evaluated as a function of structural thickness δ. The evaporation and vapor transport limits are then plotted in Figure 4.19 along with the experimental measurements CHF for the 0.6 and 1.0 μm pore diameter nickel IOs. The calculation of the evaporation limit assumes that liquid pemeates through the entirety of the IO thickness, which suggests that CHF enhances with increasing δ. However, the experimental CHF maxima and reversal in boiling performance with higher δ are prompted by the vapor transport limit, which considers liquid-vapor interfacial transport inside the IOs that become a dominate governing mechanism for transport behaviors. The wall superheat ΔT used in Equation 4.12 is based on the average ΔT of various δ studied in the set of $d_{pore} = 0.6$ and 1.0 μm. The theoretical limits predicted using fundamental hydrodynamic principles shown in Figure 4.19 matches relatively well with the experimental measurements. This can be contributed to the highly-ordered microporous architecture of IOs with explicitly controllable features, which allows for predictable results.

When comparing the boiling heat transfer performance for the 0.6 and 1.0 μm pore diameter IOs with varying thicknesses between 1 and 10 μm in Figure 4.20, both set of pore diameters exhibit similar trends in increasing boiling efficacy before decreasing. However, the 1.0 μm pore diameter IOs consistently exhibit lower boiling performances than the 0.6 m pore diameter IOs for any given δ. The maximum observed critical heat fluxes are ~115 and 100 W/cm^2 for 0.6 and 1.0 m pore diameter samples, respectively. To understand this phenomenon, the investigation is extended to study the effect of IO pore diameter on boiling performance.
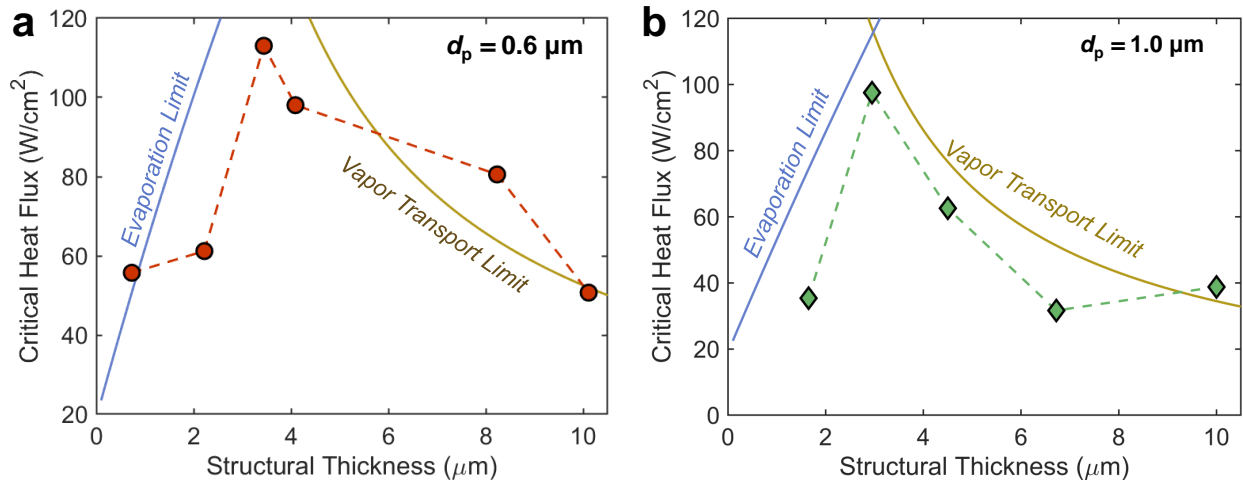
Figure 4.19: Heat Transfer Predictions of Structural Thickness-dependent Pool Boiling Performance. The evaporation and vapor transport limits as respectively predicted from Equation 4.7 and 4.12 are plotted along with the experimentally measured CHF of (a) 0.6 and (b) 1.0 μm pore diameter samples with varying structural thicknesses.
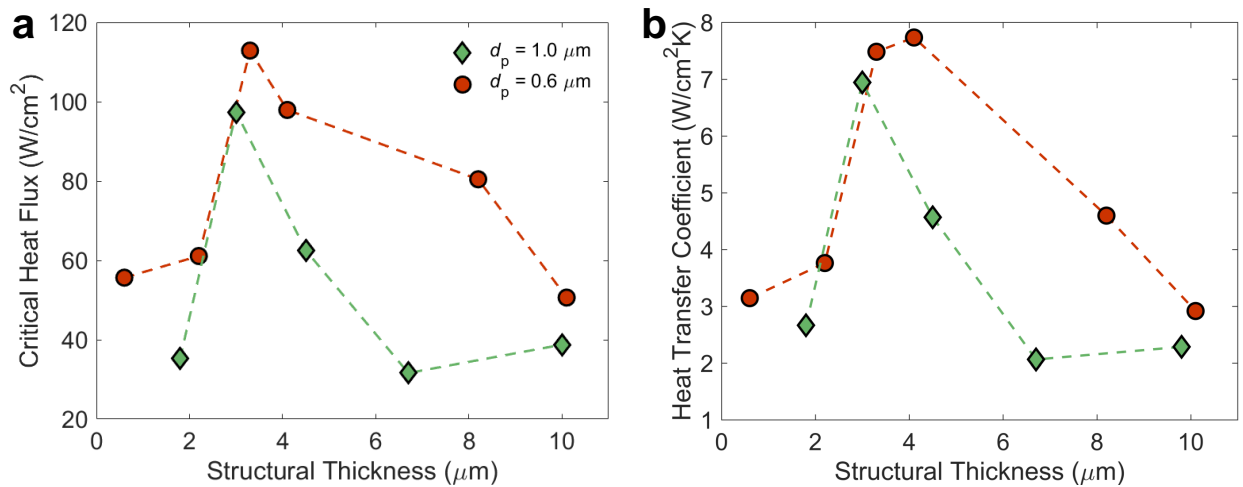
Figure 4.20: The Effect of Structural Thickness on Boiling Performance for Inverse Opals with Different Pore Diameters. (a) The critical heat flux and (b) heat transfer coefficient are plotted as a function of structural thickness for the 0.6 μm pore diameter (red-filled circles) and 1.0 μm pore diameter (green-filled diamonds) samples. The boiling performances initially increase for both sets of pore diameters until approaching a critical thickness, which then causes the boiling performances to deteriorate. The 0.6 μm pore diameter samples consistently outperform the 1.0 μm pore diameter samples for any given structural thickness.
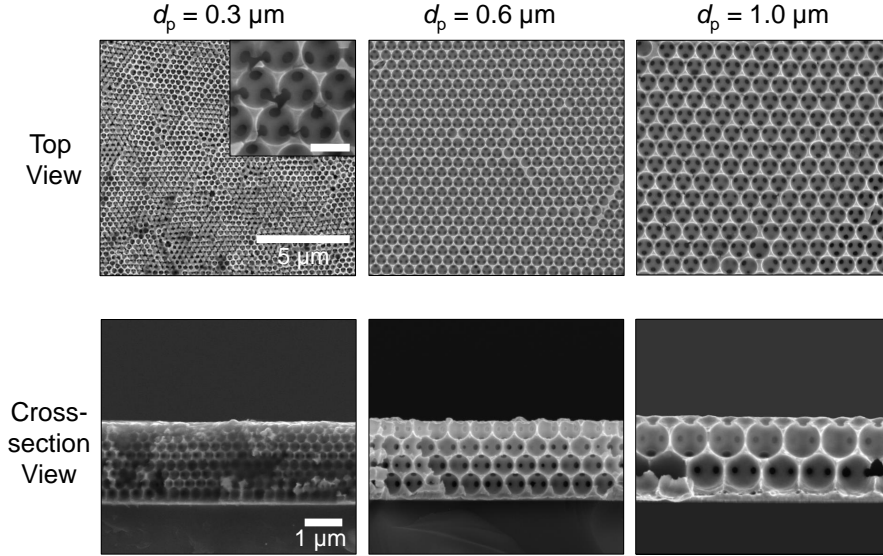
Figure 4.21: Morphology of Inverse Opals with Constant Structural Thickness.
Representative top and cross-sectional SEM images of nickel inverse opals with pore diameters ranging from 0.3 to 1.0 μm. The large-scale crystalline and highly-interconnected pore packing of the porous matrix demonstrate tunable structural thicknesses. The inset SEM image has a scale bar of 300 nm.

4.5.3   Pore Diameter-Dependent Boiling Performances

The boiling performances of nickel IOs with varying pore diameters (d_{pore} = 0.3, 0.6, and 1.0 μm) are investigated. Figure 4.21 displays the corresponding SEM images of the different pore diameter IO samples. The cross-sectional images shows that the IO structures maintain a constant δ = 2 μm and φ = 80%.

The boiling curves as a function of the wall superheat for the pore diameter-dependency experiments are plotted in Figure 4.22a, which demonstrate the 0.6 μm pore diameter IO exhibiting the highest boiling limit at ~60 W/cm^2. The heat transfer coefficients shown in Figure 4.22b increases with the heat flux for all samples and confirms that the 0.6 μm pore diameter IO possess the highest boiling efficacy compared to the other samples.
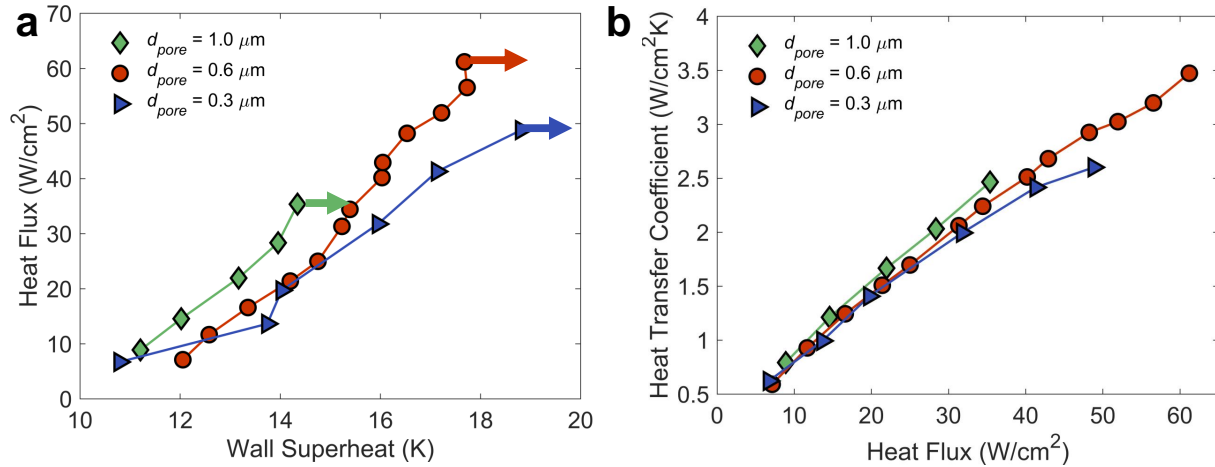
Figure 4.22: Boiling Curves of Pore Diameter-dependent Boiling Performance.
(a) Heat flux as a function of wall superheat and (b) heat transfer coefficient as a function of heat flux for nickel inverse opals with varying pore diameters (0.3, 0.6, and 1.0 μm while structural thickness remains constant at 2 μm. The horizontal arrows in (a) represents the initiation of CHF.

The resulting CHF and maximum HTC values are plotted in Figure 4.23 and suggest an increase in boiling performance with increasing pore diameter from 0.3 to 0.6 μm. However,
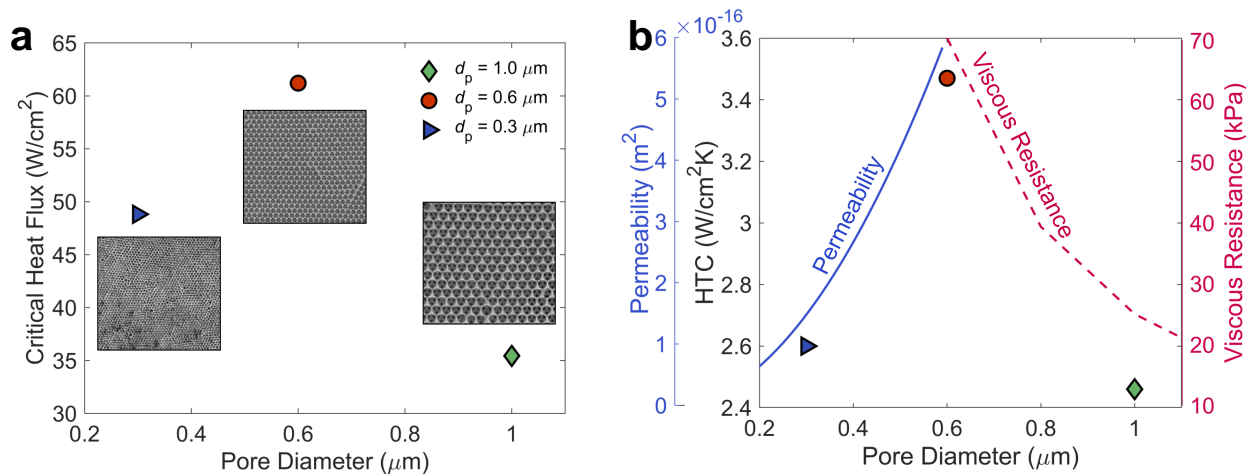
Figure 4.23: Pore Diameter-dependent Boiling Performance. At a constant structural thickness of 2 μm, (a) the critical heat flux and (b) heat transfer coefficient improve from 0.3 to 0.6 μm pore diameter before subsequently decreasing at 1.0 μm pore diameter. The permeability (blue line) and viscous resistance (magenta dashed line) associated with the inverse opal structure as a function of pore diameter are plotted.

further increase in pore diameter to 1.0 μm causes the CHF to decrease to 35 W/cm^2. This may be unexpected since larger d_{pore} provides larger structural permeability for improved liquid-vapor transport. This theory is validated by analytically estimating the liquid permeability K_l by relating a constant structural porosity φ and variable pore diameters d_{pore} through an expression $K_l = d_{pore}^2(0.07\varphi^2 - 0.0539\varphi)$, derived using CFD simulation results and is valid for 78% $<\varphi<$92%.[75] By increasing d_{pore} from 0.3 to 1.0 μm, K_l is estimated to increase from 1.5×10^{-16} to 1.7×10^{-16} m^2. Increasing permeability demonstrates the assistance of liquid-vapor routing through the enlarged pathways. However, the enlargement of d_{pore} may also contribute to an increase in viscous resistance, which can begin to dominate hydraulic transport physics.[75] The viscous resistance to fluid flow has been shown to scale inversely with the square of d_{pore}.[222] Such high viscous resistance within the microporous media can induce drag on vapor transport, affecting the bubble nucleation and departure characteristics. This may be evident when comparing the bubble departure rate of $d_{pore} =$ 0.6 μm to 1.0 μm samples with varying δ from Section 4.4.3. It is generally observed that the 1.0 μm pore diameter samples depart bubbles at slower frequencies than the 0.6 μm pore diameter samples (see Figure 4.13), and therefore, possess a lower the rate of heat flux removal.

The governing factors of permeability and viscous resistance within an IO are plotted in Figure 4.23b as blue line and dashed magenta line, respectively. The calculated permeability and viscous resistance closely match the trends of the resulting HTC with increasing IO pore diameter. Similar to rationally designing future phase-change devices with optimal structural thicknesses with reasonable design footprints, the optimal pore diameter must also be considered to holistically enhance boiling heat transfer performance.

4.5.4 Structure-Performance Enhancement Comparison

The resulting boiling performances of nickel IOs presented here are compared to those of other 3D interconnected pores for wide ranges of pore sizes. The microporous architectures used in this comparison include sintered particles, electrodeposited metal around electrochemically-generated bubbles, and commercially-available metallic or graphitic foams.[1–6] While these classes of porous structures all possess random pore interconnectivity and relatively large pore size disparities, they are evaluated owing to their three-dimensional pore interconnectivity and definable pore sizes. Therefore, micropillars and nanowire arrays are not considered for comparisons because they lack pores with measurable dimensions or pores with three-dimensional interconnectedness. In addition, the presented studies are chosen because they conducted their pool boiling measurements using DI water as the working fluid under atmospheric pressure, which is similar to our experimental conditions. This allows the current study to be comparable to the previous work. Since boiling measurement setup varies between research groups, boiling performances may slightly differ. Normalizing the reported maximum HTC values of the porous coatings to those of the plain surfaces respective to each study enables appropriate comparison in the heat transfer enhancements contributed by the microporous surfaces. The normalized HTC results are shown in Figure 4.24. Prior studies demonstrate between approximately 150% and 315% in maximum HTC enhancement. Details regarding the CHFs and HTCs reported in these studies are presented in Table 4.3 and Table 4.4, and it should be noted that only the highest HTC of monolithic porous coatings is considered from each study. In comparison, our nickel IOs improve boiling by 336% and 303% in HTC for 0.6 and 1.0 µm pore diameter structures, respectively, over plain silicon (highlighted in yellow in Figure 4.24). While the maximum HTC enhancement for porous coatings is selectively presented, the boiling performances for our nickel IOs can vary widely (between 100% and 300% HTC improvement), depending on their structural thicknesses and pore diameters.
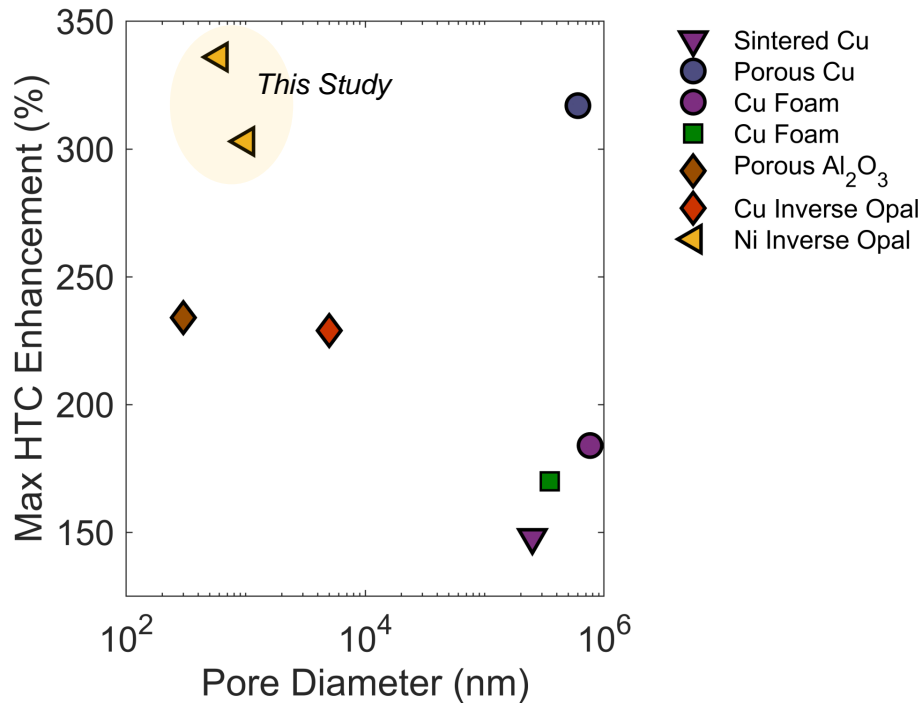
Figure 4.24: Comparing the Boiling Performances of Three-dimensionally Inter-connected Porous Media. The highest heat transfer coefficients from previous investi-gations are normalized to their plain surfaces, which are then compared to the normalized boiling performance reported from this study (highlighted in yellow). The nickel inverse opal coatings presented in this study (yellow diamonds) demonstrate up to ~350% heat transfer enhancement over plain surfaces whereas the prior studies utilizing various classes of micro-porous coatings demonstrate boiling enhancement by 100% and 325%. Prior studies include data for sintered copper (purple triangle)[1], porous copper (blue circle) [2], copper foam (purple circle) [3], copper inverse opal (red diamond) [4], copper foam (green square) [5], and porous aluminum oxide (brown diamond)[6].

Boiling Structure	CHF (W/cm^2)	HTC(W/cm^2K)	Cite
Sintered Cu	230	10.5	[1]
Electrodeposited Cu	140	19.0	[2]
Cu Foam	161	14.9	[3]
Cu Foam	52	2.38	[5]
Al_2O_3 Nanopores	271	9.6	[6]
Cu IO	225	11.0	[4]
Ni IO	113	7.1	this study

Table 4.3: Comparison of pool boiling performance from prior studies and the current experiment, which all used water as the working fluid and conducted at atmospheric pressure.

Plain	CHF_{ref} (W/cm^2)	HTC_{ref} (W/cm^2K)	$HTC_{enhanced}$ (%)	Cite
Cu	140.0	7.1	148	[1]
Cu	90.0	6.0	317	[2]
Cu	168.0	8.1	184	[3]
N/A	31.1	1.4	170	[5]
Al	126.0	4.1	234	[6]
Si	79.1	4.8	229	[4]
Si	47.0	2.1	336	this study

Table 4.4: Comparing the boiling efficacy of reference surfaces from prior and the current study, which all used water as the working fluid and conducted at atmospheric pressure.

4.6 Conclusions

Utilizing the well-regulated structural characteristics of IOs, new insights toward the fundamental boiling behaviors in 3D highly-interconnected metallic microporous media can be elucidated. The uniformity of the IO architecture permits systematic modulation of structural features and examining their mechanistic role in triggering the onset of CHF. By rationally designing the IO structures with specific combinations of structural characteristics (e.g., structural thickness and pore diameter), boiling heat transfer can be optimally enhanced up to 336% in comparison to smooth silicon surfaces. With variable structural thicknesses, the hydrodynamic competition occurs between the evaporation of the impinged liquid and the viscous resistance of the escaping vapor within the space confinement of the microporous matrix. During nucleate boiling, increasing heat fluxes cause vapor pockets to form and coalesce near the base of the microporous structure, which impede liquid from flowing to

the phase-change surfaces and is denoted as the boiling regime. While these vapor pockets contribute to improved bubble departure and consequently heat removal, the increase in structural thickness allows the vapor growth to spread within the porous media as it escapes upward, causing severe localized dryouts before the coalesce vapor bubbles have a chance to leave the media. By balancing the hydrodynamic liquid-vapor behaviors within the confinement of a rationally designed wick thickness, optimal boiling heat transfer performance can be achieved. For a given structural thickness, increasing pore diameter can enhance CHF and HTC due to the enlargement in permeability for improved liquid-vapor routings, but the continual increase in pore sizes can also limit boiling heat transfer improvement and cause a reduction to heat and mass transfer due to the increase in the viscous resistance to fluid flow.

In addition, the surface wettability of nickel IOs is examined over the duration of the boiling experiment to understand its effect on the intrinsic liquid rewetting of the surfaces and surface wetting durability. While the nickel IOs are hydrophilic before boiling, they rapidly transitioned to hydrophobic within the first hour of the boiling by exhibiting high static and advancing contact angles. However, the receding contact angles remain consistently low, which suggest that liquid remains strongly pinned to the porous structure in a Wenzel wetting state. The strong propensity to impinge liquid may contribute to the rewetting of the heated surfaces and preventing premature film boiling as often observed for hydrophobic surfaces. The low droplet receding contact angles also correlates to the angles in which liquid recedes as vapor bubble grows, which minimize bubble base diameter and prevent vapor spreading across the surface. Studying the wetting durability of materials and surfaces is critical to the understanding of dynamic wetting behaviors in complex hydrodynamic phase-change processes. The fundamental interfacial and structure-thermophysical relations elucidated from this chapter can significantly contribute to the design of next-generation phase-change thermal management devices.

Chapter 5

Conclusions and Outlook

5.1 Summary of Work

Inverse opals pose interesting properties and promising performance for use as porous wicking media in phase-change cooling systems, owing to their continuous, fluid permeable network of pores with enormous interfacial surface areas for enhanced heat and mass transport. While IOs as a structural material have been investigated within the past half decade for their optical and photonic properties, only within the past decade has IOs garnered increasing attentions for exploited uses as sensors, catalysis, separator, energy storage and conversion, and heat exchangers, with which, the fundamental understanding of the material's intrinsic mass and energy transport physics are still lacking.[86, 90, 126] In comparison, extensive efforts have been directed to elucidating transport behaviors in stochastically arranged porous media,[104, 105] but due to their random and heterogeneous nature, these efforts solely rely on computer reconstruction and describe their intrinsic properties through characteristic descriptors in a general and probabilistic manner. The regularity of IOs provides the unique opportunity to fully and deeply extract their structure-property correlations, which can be

used as engineering guidance in designing IOs for a myriad of applications, including as a wicking medium in future heat pipes and vapor chambers.

The performance of heat pipes is limited by their ability to capillary-feed liquid over long working distance from low heat flux sources. Conversely, the operating limit of ultra-thin vapor chambers is based on their boiling heat transfer efficacy at extremely high localized heat flux but over small working length. The primary differences in transfer regimes between capillary-based transport and pool boiling in these two-phase cooling devices are explored in this work for metallic IOs.

While capillary transport within a perfect, crystalline inverse opal unit cell can be trivially modeled due to exact knowledge of the geometry and symmetries using finite elements, hydraulic transport in a polycrystalline inverse opal superstructure requires more detailed knowledge of the underlying transport physics in the presence of grain boundaries and defects. Leveraging the high spatial, temporal and contrast resolution of fluorescent microscopy combined with scanning electron microscopy, the liquid propagation can be investigated with high fidelity. The capillary-assisted hydraulic transport through IOs demonstrate unique discretized stop-and-go motions across grain boundaries, that become the dominant hydraulic resistance to mass transport. The degree of porous domain anisotropy significantly favors enhanced liquid flow in preferential directions. With a highly viscous working fluid, the flow rate is strongly influenced by the permeability and porosity of the media. Microscopic examination of the boundaries reveal that their characteristics are nonuniform with varying width and height along their length; defects also exist along the boundaries, such as breakage, where liquid percolate across because of the lower hydraulic resistance needed to overcome the barrier. Rigorous monitoring of the capillary flow within individual domains reveal that the intrinsic permeability of the crystalline media decrease with increasing propagating distance due to the throttling caused by the grain boundaries. This work establishes

fundamental insights toward the modification of Darcy law in describing and predicting hydraulic transport in polycrystalline porous media.

Boiling has been utilized to effectively remove massive amount of unwanted heat in many industrial processes, and it can be used to describes the performance limit of vapor chambers. The understanding and enhancement in boiling heat transfer performance have been an ongoing effort for over the last half century with significant focus on structured surfaces and porous coatings as the phase-change surfaces. Despite much effort, the universal acceptance on the complex liquid-vapor interactions within 3D interconnected porous media is still lacking, which makes empirical correlations difficult between studies. This is mainly due to the irregularity in pore distributions and structural arrangement often used in boiling measurements. The well-regulated and ordered microporous architecture of IOs allow systematic examination of how their structural characteristics affect boiling behaviors. Experimental results demonstrate that the IO structure-property relation can be tuned (in terms of pore diameter and structural thickness) to yield optimal boiling performances, which demonstrate up to 336% enhancement over smooth surfaces. The optimal IO thickness is approximately 3 to 4 m, which is manifested through the balance of liquid-vapor occupation within the spatial confinement of the inverse opal structure. The optimization of boiling performances with varying pore diameters (0.3-1.0 m) can be attributed to the hydraulic competitions between permeability and viscous resistance to liquid-vapor transport. This study unveils thermophysical understandings to enhance multiphase heat transfer in microporous media for ultrahigh heat flux thermal management.

5.2 Broader Perspectives

5.2.1 Surface Engineering of Metallic Inverse Opals

Despite the ideal high thermal conductivity of nickel and copper for phase-change heat transfer applications, their surface chemistry renders them naturally hydrophobic and prevents them from wicking fluid such as water. While water penetration through the porous media has been demonstrated through liquid pinning, sustainable capillary-driven transport cannot be supported. Instead, other liquids, such as refrigerant, can be utilized because of their lower surface energy. However, since the latent heat of vaporization for these fluids are approximately two orders of magnitude lower than that of water and are typically ideal for devices operating at low superheat temperatures, their usage and intrinsic performance may be severely limited. To leverage the high latent vaporization of water, the surface energy of the metallic IO skeleton can be engineered to promote water wicking (or repulsion).

Previous surface engineering attempts to modify the surface chemistry and energy of copper IOs include chemical or materials coating, chemical oxidation, electrochemical oxidation, and thermal oxidation, which prove to be scalable, simple, and cost-effective. [63, 93, 223] In chemical coating, thin self-assembled monolayer can conformally coat the skeleton without altering the morphology of the porous media. By selecting the appropriate chemical composition (e.g., sodium 3-mercapto propanesulfonate or dodecanonic acid), the wetting characteristics can be either highly hydrophilic or superhydrophobic. Similar results can also be achieved through atomic layer deposition (ALD) of materials (e.g., silica to render the surface hydrophilic). In chemical oxidation, the metallic surfaces can be immersed in a chemical solution to grow nanoscale oxide features directly on the surfaces. Depending on the combinations of process temperature, processing time, and chemical compositions, various sizes and densities of these oxides can be synthesized and consequently tune the degree of surface hydrophobicity to hydrophilicity. Electrochemical oxidation utilizes electrochem-

115

istry to deposit nanostructural oxides onto the surface. Thermal oxidation can functionalize the surface through diffusing oxidizing agents into the structural materials at high temperatures ranging approximately 300 $^{|circ}$C. Surface engineering methods can influence the final porosity and permeability of the structure, which needs to be taken into account when designing the media. Surface modifications can also create hierarchical structures that exhibit multiscalar features that can be leveraged for numerous interfacial transport applications. Through the conjunction of one or more of these methods, both the wetting functionality and the corresponding liquid transport capability of water through the porous matrix can be systematically controlled. Nevertheless, the durability of the engineered surface must be validated for the continuation of the intended functionalities over an extended period of time or under extreme heating conditions.

5.2.2 Large-scale Manufacturing of Metallic Inverse Opals

The mass and heat transport properties of IO demonstrated here are performed using IO fabricated at the small scale (approximately 1 cm^2). From the application-based perspective, large scale and rapid manufacturing of well-ordered IOs need to be realized to make the material-based technology viability for industrial adoption.

Among the enumerated opal deposition techniques explored, spin-coating and Langmuir-Blodgett demonstrate poor crystalline packing radially and handling difficulty of thin film, respectively. [108, 224] While vertical deposition produces highly-ordered colloidal crystals, such template deposition method poses certain process limitations. For instance, the process can only accommodate sphere diameters below 1 μm and has a limited areal coverage of 1 - 2 cm^2. Lastly, vertical deposition is a time-consuming process such that larger areal coverage deposition occurs over the span of days, making the process unsuitable for high throughput production.
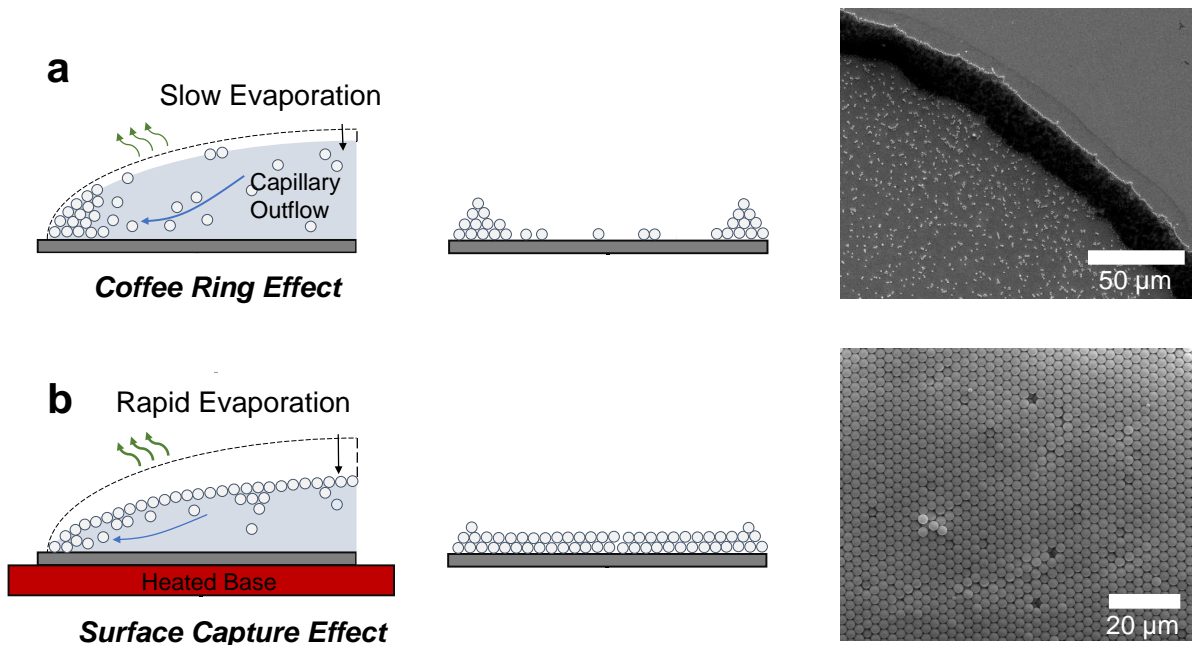
Figure 5.1: Opal Self-Assembly through Dropcasting of Suspension of Monodisperse Nanospheres. (a) Schematics and SEM images showing the clustering of colloids in a coffee-ring formation. (b) By speeding the self-assembly process, colloids are forced to pack into crystalline arrangement with limited migration toward the solid-liquid-vapor interfacial edges.

An alternative templating deposition process includes gravity sedimentation through drop-casting method, [122] which can address the limitations in sphere sizes and opal coverage area. As the dropcasted colloidal suspension dries on a surface, the majority of the spheres migrates towards the edge of the droplet due to capillary action at the solid-liquid-vapor thin film, producing a coffee ring effect. Such phenomena deposits disproportionate amount of spheres radially (Figure 5.1). However, by optimizing the colloidal concentration and surface temperature, the self-assembly of spheres can be controlled to exhibit crystalline packing and reduce the coffee ring effect. In this method, a high colloidal concentration of 4% and elevated substrate temperature of 80 °C (through hot plate heating) promotes rapid sphere self-assembly. The rise in temperature causes the evaporative front to quickly collapse, trapping the sufficiently available spheres to self-assemble into crystalline packing while reducing the ability for spheres to migrate toward the droplet edges, a process called
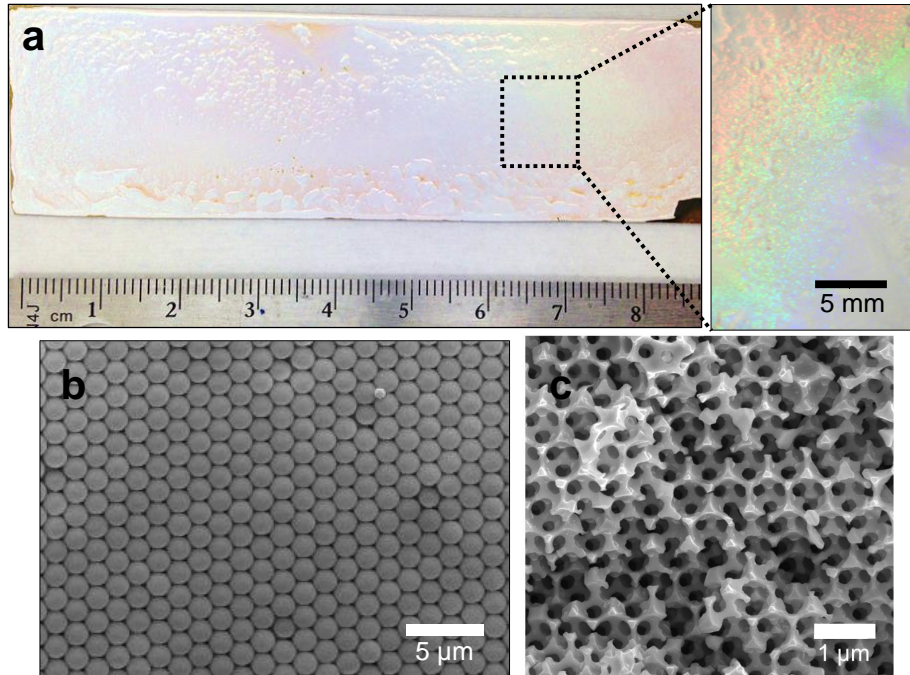
Figure 5.2: Fabrication of Large-Scale Inverse Opal through Rapid Evaporation Process. (a) Deposition of crystalline opal template. The opalescent quality of the template can be seen through optical reflection from various incident angle of white light. Top view (SEM) image of the (b) opal template and (c) copper IO structure.

surface capture effect. [176] Rapid evaporation dropcasting method allows us to deposit larger area of high-quality templated opal up to 2500 cm^2 within minutes (see Figure 5.2). Larger areal coverage is not tested within the current study but remains possible to scale up using such strategies. The simple sedimentation process permits various sphere sizes to be used, allowing us to create ordered inverse opal structures with >1 μm pore diameter. The optimized dropcasting method promises tremendous feasibility in creating well-ordered porous architecture with high throughput for industrial and manufacturing applications.

Dropcasting method of opal template can also be employed to create high-quality 3D inverse opal structures on flexible substrates of any conductive materials, such as copper. Figure 5.3 demonstrate a fabricated copper inverse opal structure on a large-scale, flexible copper foil substrate. The high thermal conductivity of the foil enhances heat spreading, and the copper-copper bonding eliminates any potential material mismatch coefficients that can cause
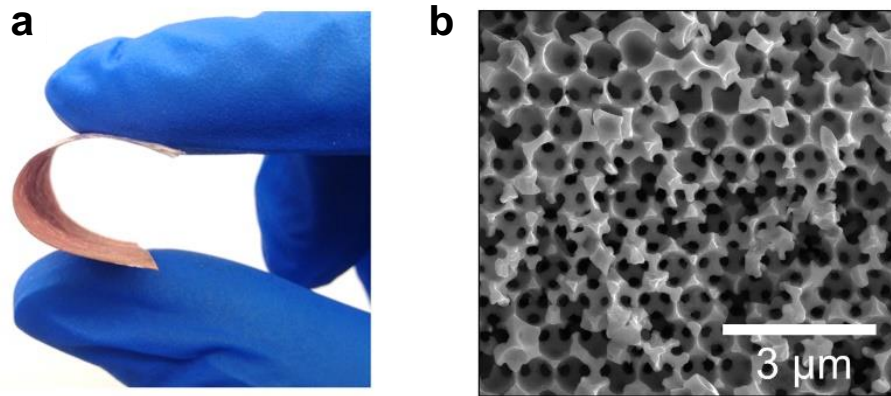
Figure 5.3: Fabrication of Copper Inverse Opal on Flexible Copper Foil. (a) The porous coated foil can withstand significant bending stresses without little to no structural damages. (b) SEM image of the copper inverse opal structure after multiple cycles of substrate bending.

structural delamination from the substrate under physical and thermal stresses. The combination of dropcasting fabrication technique and the low cost of foil materials (in comparison to silicon or bulk copper) make the manufacturing process inexpensive with high throughput and therefore, feasible for mass production. The viability of flexible phase-change cooling technology can also be realized.

5.2.3 Polymer-based Inverse Opals

While the presented work here focuses solely on metallic IOs (copper and nickel) due to their high thermal conductivity for heat transfer application, the skeleton structure of IOs can also be created from alloys, [127] carbon, [118] or polymer [128, 131, 225] to address the unique intrinsic demand from each membrane-based applications ranging from filtration, electrochemical energy storage, and catalysis. Since thin film membrane technologies often require pore surfaces to be chemically inert due to the chemically active and corrosive nature of the working fluid, polymer-based porous media remain an ideal material-based so-

lution, promising durability, flexibility, and biocompatible. Previous investigations created IO structures with polymer and epoxy materials, such as PUA, [128] SU-8, [131] PEG, [225] PDMS, [226] and PNIPAM, [227] some of which require specialized cleanroom facility as to prevent exposure to UV light during production. A ubiquitous polymer found in everyday materials is polyethylene terephthalate (PET) (e.g., in single-used water bottles) due to its low material cost, ease is mass manufacturing process, and surface inertness. Despite the material's high utility, no known PET-based inverse opal exists.

Here, it has been demonstrated that PET-based IOs can be created. In contrast to the template-assisted fabrication of porous structures described here for metallic IOs, which use a polymer (polystyrene) as the template and metal as the structural material, polymeric IOs use silica microspheres as the template and polymer as the structural materials. The material composition of the template and the backfilling materials must be starkly different in order to selectively etch the template while retain the porous skeleton. In this case, monodispersed silica microspheres self-assemble into close-pack crystalline arrangement through dropcasting method. Since the density of silica microspheres is much higher than that of traditional polystyrene microspheres, the particles will rapidly sediment, making vertical deposition technique impossible. After liquefying PET into an appropriate viscosity, the PET wicks into the hydrophilic silica opal film. After PET solidifies, the silica template is dissolved with hydrofluoric acid, revealing the PET IO structure, as shown in Figure 5.4. The ability to manufacture PET-based IOs increases the design space for porous media in a simple and cost-effective manner. The fabrication approach can be applied to other polymers, such as biocompatible and biodegradable polymer-based scaffolds for drug delivery and tissue engineering as well as thermally conductive polymers to enable flexible vapor chambers or heat pipes. [228–230]

120
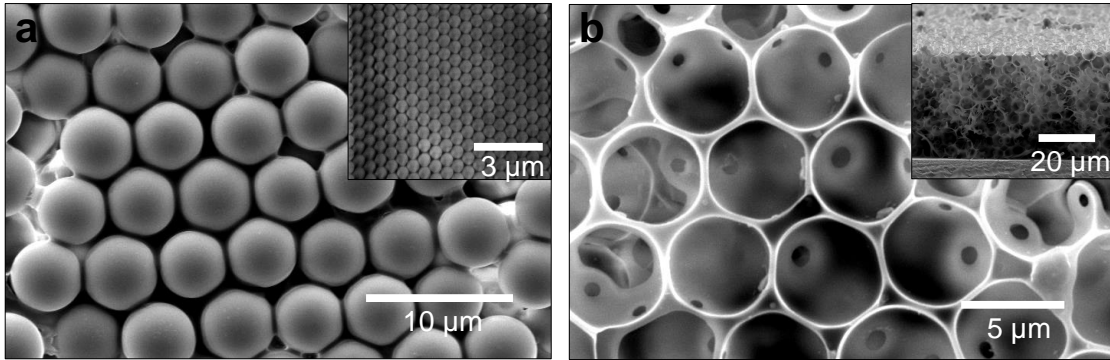
Figure 5.4: PET-Based Inverse Opal. (a) SEM images of silica microspheres with PET resin infiltrated into the void spacings. (b) After removing silica opal template, PET scaffold remains.

5.3 Future Work: Evaporation and Condensation Heat Transfer

While the capillary and boiling performance limits of two-phase heat transfer devices are evaluated, the mechanisms of evaporation and condensation also play a significant role in utilizing the latent heat of vaporization of the working fluid to transport heat from source to sink. Despite its importance, investigative efforts into the evaporation and condensation heat transfer of IOs have been extremely limited, [33, 231–233] and this lack of understanding and engineering framework delay the development of IO-based two-phase cooling devices.

Since grain boundaries in polycrystalline IOs increase the hydraulic transport resistance when laterally transporting fluid in-plane, it is expected that the rate of liquid replenishment may be difficult to maintain in pace with that of liquid evaporation, which can lead to rapid localized dry-out. Therefore, it will be of interest to observe the evaporation heat transfer limit with liquid being fed from the base to the top of the IOs (i.e., through-plane direction) to circumvent fluid transport across grain boundaries. In this hydraulic transport

configuration, IO film can be applied on top of a groove structure for a composite wick design, which promises the benefits of large capillary pressure and enormous evaporating surfaces (maintained by the small pores of the IO) as well as high permeability for constant liquid feeding (supported by the lateral grooves). Such heterogeneous wick designs have demonstrated superior fluid and heat transfer performance over homogeneous wicks [28, 234] and may be the solution to transporting liquid to the evaporating surfaces of IOs without needing to overcome inhibition presented by grain boundaries. It should be noted that while the metallic IOs are expected to be hydrophobic, liquid may still infiltrate from the base into the IO membrane due to the liquid pinning (under the observed Wenzel wetting state), which will facilitate continuous liquid feeding as evaporation occurs. Understanding the evaporative cooling limits will provide key insights into the the heat transfer performances of heat pipes and vapor chambers at lower wall temperatures.

Near the heat sink, the behaviors in which liquid vapor condensate affect the effectiveness of enthalpy removal from the system. For instance, as water vapor condenses on hydrophilic surfaces, filmwise condensation occurs such that the liquid film accumulates and grows in thickness. With the low thermal conductivity of water, heat transfer resistance between the surface and liquid increases with the liquid film thickness. To effectively remove the condensate, hydrophobic surfaces can be employed to nucleate micro- and macroscopic droplets, which rapidly shed with gravity (termed dropwise condensation) and have been shown to be an order of magnitude higher in heat transfer efficiency than filmwise condensation. [235] With the unaltered metallic IOs demonstrated here, it is expected that they will undergo dropwise condensation due to the material's hydrophobicity. However, droplet shedding may not be possible due to liquid pinning, even when the surface is tilted to 90° as previously demonstrated. The inability to remove the condensed drops causes the drop to grow, coalesce, and induce enormous heat transfer resistances. Therefore, novel strategies in surface engineering are needed to potentially design IOs with gradient surface energy along their working length to promote liquid shedding near heat sink (Cassie-Baxter hydrophobic wet-

122

ting state) while liquid wicking near heat source (Wenzel hydrophilic state). The adopted surface engineering solutions, such as conformal microstructural coatings, need to also be examined for performance durability not in terms of days or weeks commonly studied but in years and possibly decades of the device's lifetime.

Bibliography

[1] C.H. Li, T. Li, P. Hodgins, C.N. Hunter, A.A. Voevodin, J.G. Jones, and G.P. Peterson. Comparison study of liquid replenishing impacts on critical heat flux and heat transfer coefficient of nucleate pool boiling on multiscale modulated porous structures. *International Journal of Heat and Mass Transfer*, 2011.

[2] A. M. Gheitaghy, H. Saffari, D. Ghasimi, and A. Chasemi. Effect of electrolyte temperature on porous electrodeposited copper for pool boiling enhancement. *Applied Thermal Engineering*, 2017.

[3] Y. Yang, X. Ji, and J. Xu. Pool boiling heat transfer on copper foam covers with water as working fluid. *International Journal of Thermal Sciences*, 2010.

[4] H. Lee, T. Maitra, J. Palko, C. Zhang, M. Barako, Y. Won, M. Asheghi, and K. E. Goodson. Enhanced heat transfer using microporous copper inverse opals. In *International Technical Conference and Exhibition on Packaging and Integration of Electronic and Photonic Microsystems*, 2017.

[5] S. Moghaddam, M. Ohadi, and J. Qi. Pool boiling of water and fc-72 on copper and graphite foams. In *International Electronic Packaging Technical Conference and Exhibition*, 2003.

[6] B. J. Zhang and K. J. Kim. Effect of liquid uptake on critical heat flux utilizing a three dimensional, interconnected alumina nano porous surfaces. *Applied Physics Letters*, 2012.

[7] A. McWilliams. The market for thermal management technologies. Technical report, BCC Research, 2019.

[8] M.L. Bauer, Q.N. Pham, C.B. Saltonstall, and P.M. Norris. Thermal conductivity of vertically aligned carbon nanotube arrays: Growth conditions and tube inhomogeneity. *Applied Physics Letters*, 105(15):151909, 2014.

[9] Q.N. Pham, L.S. Larkin, C.C. Lisboa, C.B. Saltonstall, L. Qiu, J.D. Schuler, T.J. Rupert, and P.M Norris. Effect of growth temperature on the synthesis of carbon nanotube arrays and amorphous carbon for thermal applications. *Physica Status Solidi A*, 2017.

[10] L. Qiu, K. Scheider, S.A. Radwan, L.S. Larkin, C.B. Saltonstall, Y. Feng, X. Zhang, and P.M. Norris. Thermal transport barrier in carbon nanotube array nano-thermal interface materials. *Carbon*, 2017.

[11] W. Yu, C. Liu, L. Qiu, P. Zhang, W. Ma, Y. Yue, H. Xie, and L.S. Larkin. Advanced thermal interface materials for thermal management. *Eng. Sci*, 2018.

[12] M.T. Barako, S. Roy-Panzer, T.S. English, T. Kodama, M. Asheghi, T.W. Kenny, and K.E. Goodson. Thermal conduction in vertically aligned copper nanowire arrays and composites. *ACS Applied Materials & Interfaces*, 2015.

[13] M.T. Barako, Y. Gao, A.M. Marconnet, M. Asheghi, and K.E Goodson. Solder-bonded carbon nanotube thermal interface materials. *13th InterSociety Conference on Thermal and Thermomechanical Phenomena in Electronic Systems*, 2012.

[14] M.T. Barako, S.G. Isaacson, F. Lian, E. Pop, R.H. Dauskardt, K.E. Goodson, and J. Tice. Dense vertically aligned copper nanowire composites as high performance thermal interface materials. *ACS Applied Materials & Interfaces*, 2017.

[15] S. Wang, Y. Yin, C. Hu, and P. Rezai. 3d integrated circuit cooling with microfluidics. *Micromachines*, 2018.

[16] C. Mandalapu, I. Abdel-Motaleb, S. Hong, and R. Patti. Design, fabrication, and testing of a liquid cooling platform for high power 3d-ics. *8th International Symposium on Next Generation Electronics (ISNE)*, 2019.

[17] A. Bar-Cohe, K. Matin, N. Jankowski, and D. Sharar. Twophase thermal ground planes: technology development and parametric results. *Journal of Electronic Packaging*, 2015.

[18] R. Lewis, S. Xu, L.-A. Liew, C. Coolidge, R. Yang, and Y.-C. Lee. Thin flexible thermal ground planes: Fabrication and scaling characterization. *Journal of Microelectromechanical Systems*, 2015.

[19] C.-J. Weng. Advanced thermal enhancement and management of led packages. *International Communications in Heat and Mass Transfer*, 2009.

[20] Y.S. Ju, M. Kaviany, Y. Nam, S. Sharratt, G.S. Hwang, I. Catton, and E. Fleming. Planar vapor chamber with hybrid evaporator wicks for the thermal management of high-heat-flux and high-power optoelectronic devices. *International Journal of Heat and Mass Transfer*, 2013.

[21] Q. Cai, A. Bhunia, C. Tsai, M. W. Kendig, and J. F DeNatale. Studies of material and process compatibility in developing compact silicon vapor chambers. *J. Micromech. Microeng.*, 2013.

[22] J. Gou and W. Liu. Feasibility study on a novel 3d vapor chamber used for li-ion battery thermal management system of electric vehicle. *Applied Thermal Engineering*, 2019.

[23] J. Zeng, S. Zhang, G. Chen, L. Lin, Y. Sun, L. Chuai, and W. Yuan. Experimental investigation on thermal performance of aluminum vapor chamber using micro-grooved wick with reentrant cavity array. *Applied Thermal Engineering*, 2018.

[24] Y. Tang, L. Lin, S. Zhang, J. Zeng, K. Tang, G. Chen, and W. Yuan. Thermal management of high-power leds based on integrated heat sink with vapor chamber. *Energy Conversion and Management*, 2017.

[25] S.M. Thompson, A.A. Hathaway, C.D. Smoot, C.A. Wilson, H.B. Ma, R.M. Young, L. Greenberg, B.R. Osick, S. Van Campen, B.C. Morgan, D. Sharar, and N. Jankowski. Robust thermal performance of a flat plate oscillating heat pipe during high-gravity loading. *Journal of Heat Transfer*, 2011.

[26] Q. Wang, Z. Rao, Y. Huo, and S. Wang. Thermal performance of phase change material/oscillating heat pipe-based battery thermal management system. *International Journal of Thermal Sciences*, 2016.

[27] M. Annamalai and S. Dhanabal. Experimental studies on porous wick flat plate heat pipe. In *International Refrigeration and Air Conditioning Conference*, 2010.

[28] G. Franchi and X. Huang. Development of composite wicks for heat pipe performance enhancement. *Heat Transfer Engineering*, 2008.

[29] K.C. Leong, C.Y. Liu, and G.Q. Lu. Characterization of sintered copper wicks used in heat pipes. *Journal of Porous Materials*, 4(4):303–308, 1997.

[30] J.-H. Liou, C.-W. Chang, C. Chao, and S.-C. Wong. Visualization and thermal resistance measurement for the sintered mesh-wick evaporator in operating flat-plate heat pipes. *International Journal of Heat and Mass Transfer*, 53(7):1498–1506, 2010.

[31] S.-C. Wong, J.-H. Liou, and C.-W. Chang. Evaporation resistance measurement with visualization for sintered copper-powder evaporator in operating flat-plate heat pipes. *International Journal of Heat and Mass Transfer*, 53(19):3792–3798, 2010.

[32] Y. Sun, S. Zhang, G. Chen, Y. Tang, and F. Liang. Experimental and numerical investigation on a novel heat pipe based cooling strategy for permanent magnet synchronous motors. *Applied Thermal Engineering*, 2020.

[33] K. Montazeri, S. Zhang, M.J.A. Qomi, and Y. Won. Investigation of atomistic-scale thin-film evaporation. *2018 17th IEEE Intersociety Conference on Thermal and Thermomechanical Phenomena in Electronic Systems (ITherm)*, 2018.

[34] P. Hanafizadeh, M. Ashjaee, M. Goharkhah, K. Montazeri, and M. Akram. The comparative study of single and two-phase models for magnetite nanofluid forced convection in a tube. *International Communications in Heat and Mass Transfer*, 2015.

[35] J.A. Weibel, S.V. Garimella, and M.T. North. Characterization of evaporation and boiling from sintered powder wicks fed by capillary action. *International Journal of Heat and Mass Transfer*, 2010.

[36] K. De Kerpel, S.D. Schampheleire, H. Steuperaert, P.D. Jaeger, and M.D. Paepe. Experimental study of the effect of felt wick porosity on capillary-driven heat pipes. *Applied Thermal Engineering*, 2016.

[37] S. Zhang, Y. Tang, J. Zeng, W. Yuan, J. Chen, and C. Chen. Pool boiling heat transfer enhancement by porous interconnected microchannel nets at different liquid subcooling. *Applied Thermal Engineering*, 2016.

[38] Y. Tang, H. Tang, J. Li, S. Zhang, B. Zhuang, and Y. Sun. Experimental investigation of capillary force in a novel sintered copper mesh wick for ultra-thin heat pipes. *Applied Thermal Engineering*, 2017.

[39] S. Zhang, Y. Sun, W. Yuan, Y. Tang, H. Tang, and K. Tang. Effects of heat flux, mass flux and channel width on flow boiling performance of porous interconnected microchannel nets. *Experimental Thermal and Fluid Science*, 2018.

[40] C. Li and G.P. Peterson. Evaporation/boiling in thin capillary wicks (ii)—effects of volumetric porosity and mesh size. *Journal of Heat Transfer*, 128(12):1320–1328, 2006.

[41] D. Jafari, H. Shamsi, S. Filippeschi, P. Di Marco, and A. Franco. An experimental investigation and optimization of screen mesh heat pipes for low-mid temperature applications. *Experimental Thermal and Fluid Science*, 2017.

[42] S. Zhang, J. Chen, Y. Sun, J. Li, J. Zeng, W. Yuan, and Y. Tang. Experimental study on the thermal performance of a novel ultra-thin aluminum flat heat pipe. *Renewable Energy*, 2019.

[43] Y. Li, H.-F. He, and Z.-X. Zeng. Evaporation and condensation heat transfer in a heat pipe with a sintered-grooved composite wick. *Applied Thermal Engineering*, 2013.

[44] G. Huang, W. Yuan, Y. Tang, B. Zhang, S. Zhang, and L. Lu. Enhanced capillary performance in axially grooved aluminium wicks by alkaline corrosion treatment. *Experimental Thermal and Fluid Science*, 2017.

[45] J. Cheng, G. Wang, Y. Zhang, P. Pi, and S. Xu. Enhancement of capillary and thermal performance of grooved copper heat pipe by gradient wettability surface. *International Journal of Heat and Mass Transfer*, 2017.

[46] S. Zhang, Y. Tang, W. Yuan, J. Zeng, and Y. Xie. A comparative study of flow boiling performance in the interconnected microchannel net and rectangular microchannels. *International Journal of Heat and Mass Transfer*, 2016.

[47] Y. Sun, G. Chen, S. Zhang, Y. Tang, J. Zeng, and W. Yuan. Pool boiling performance and bubble dynamics on microgrooved surfaces with reentrant cavities. *Applied Thermal Engineering*, 2017.

[48] Y. Nam, S. Sharratt, C. Byon, S.J. Kim, and Y. S. Ju. Fabrication and characterization of the capillary performance of superhydrophilic cu micropost arrays. *Journal of Microelectromechanical Systems*, 2010.

127

[49] R. Xiao, R. Enright, and E.N. Wang. Prediction and optimization of liquid propagation in micropillar arrays. *Langmuir*, 2010.

[50] M.R.S. Shirazy and L.G. Frechette. Capillary and wetting properties of copper metal foams in the presence of evaporation and sintered walls. *International Journal of Heat and Mass Transfer*, 2013.

[51] J. Qu, Q. Sun, H. Wang, D. Zhang, and J. Yuan. Performance characteristics of flat-plate oscillating heat pipe with porous metal-foam wicks. *International Journal of Heat and Mass Transfer*, 2019.

[52] H.S. Jo, S. An, X.H. Nguyen, Y.I. Kim, B.-H. Bang, S.C. James, J. Choi, and S.S. Yoon. Modifying capillary pressure and boiling regime of micro-porous wickstextured with graphene oxide. *Applied Thermal Engineering*, 2018.

[53] X. Yang, J. Yu, Z. Guo, L. Jin, and Y.-L. He. Role of porous metal foam on the heat transfer enhancement for a thermal energy storage tube. *Applied Energy*, 2019.

[54] D. Jafari, W.W. Wits, and B.J. Geurts. Metal 3d-printed wick structures for heat pipe application: Capillaryperformance analysis. *Applied Thermal Engineering*, 2018.

[55] S. G. Liter and M. Kaviany. Pool-boiling chf enhancement by modulated porous-layer coating: Theory and experiment. *International Journal of Heat and Mass Transfer*, 2001.

[56] J. Xu, X. Ji, W. Zhang, and G. Liu. Pool boiling heat transfer of ultra-light copper foam with open cells. *International Journal of Heat and Mass Transfer*, 2008.

[57] S. Jun, J. Kim, D. Son, H.Y. Kim, and S.M. You. Enhancement of pool boiling heat transfer in water using sintered copper microporous coatings. *Nuclear Engineering and Technology*, 2016.

[58] R. L. Webb. Nucleate boiling on porous coated surface. *Heat Transfer Engineering*, 1983.

[59] S. Sarangi, J.A. Weibel, and S.V. Garimella. Effect of particle size on surface-coating enhancement of pool boiling heat transfer. *International Journal of Heat and Mass Transfer*, 2015.

[60] S. Sarangi, J. A. Weibel, and S. V. Garimella. Quantitative evaluation of the dependence of pool boiling heat transfer enhancement on sintered particle coating characteristics. *Journal of Heat Transfer*, 2016.

[61] R.P. Rioux, E.C. Nolan, and C.H. Li. A systematic study of pool boiling heat transfer on structured porous surfaces: From nanoscale through microscale to macroscale. *AIP Advances*, 2014.

[62] L. Courbin, J.C. Bird, M. Reyssat, and H.A. Stone. Dynamics of wetting: Form inertial spreading to viscous imbibition. *Journal of Physics: Condensed Matter*, 2009.

[63] Q.N. Pham, B. Shao, Y. Kim, and Y. Won. Hierarchical and well-ordered porous copper for liquid transport properties control. *ACS Applied Materials & Interfaces*, 2018.

[64] D.M. Spori, T. Drobek, S. Zürcher, M. Ochsner, C. Sprecher, A. Mühlebach, and N.D. Spencer. Beyond the lotus effect: Roughness influences on wetting over a wide surface-energy range. *Langmuir*, 2008.

[65] Y.H. Yeong, A. Milionis, E. Loth, and I.S. Bayer. Microscopic receding contact line dynamics on pillar and irregular superhydrophobic surfaces. *Scientific Reports*, 5:8384, 2015.

[66] A. Davis, Y.H. Yeong, A. Steele, I.S. Bayer, and E. Loth. Superhydrophobic nanocomposite surface topography and ice adhesion. *ACS Applied Materials & Interfaces*, 6(12):9272–9279, 2014.

[67] P.G. de Gennes, F. Brochard-Wyart, and D. Quere. *Capillarity and Wetting Phenomena: Drops, Bubbles, Pearls, Waves.* New York: Springer, 2004.

[68] C.W. Extrand, S.I. Moon, P. Hall, and D. Schmidt. Superwetting of structured surfaces. *Langmuir*, 2007.

[69] E. Martines, K. Seunarine, H. Morgan, N. Gadegaard, C.D.W Wilkinson, and M.O. Riehle. Superhydrophobicity and superhydrophilicity of regular nanopatterns. *Nano Letters*, 2005.

[70] J. Park, H.-S. Han, Y.-C. Kim, J.-P. Ahn, M.-R. Ok, K.E. Lee, J.-W. Lee, P.-R. Cha, H.-K. Seok, and H. Jeon. Direct and accurate measurement of size dependent wetting behaviors for sessile water droplets. *Scientific Reports*, 2015.

[71] K. Seo, M. Kim, J.K. Ahn, and D.H. Kim. Effects of drop size and measuring condition on static contact angle measurement on a superhydrophobic surface with goniometric technique. *Korean Journal of Chemical Engineering*, 2015.

[72] C. Ishino, M. Reyssat, E. Reyssat, K. Okumura, and D. Quere. Wicking within forests of micropillars. *A Letters Journal Exploring the Frontiers of Physics*, 2007.

[73] E.W. Washburn. The dynamics of capillary flow. *Physical Review*, 1921.

[74] J. M. Bell and F. K. Cameron. The flow of liquids through capillary spaces. *Journal of Physical Chemistry*, 1906.

[75] Q.N. Pham, M.T. Barako, J. Tice, and Y Won. Microscale liquid transport in polycrystalline inverse opals across grain boundaries. *Scientific Reports*, 2017.

[76] C. Byon and S.J. Kim. Capillary performance of bi-porous sintered metal wicks. *International Journal of Heat and Mass Transfer*, 2012.

[77] B.S. Kim, G. Choi, D.I. Shim, K.M. Kim, and H.H. Cho. Surface roughening for hemi-wicking and its impact on convectiveboiling heat transfer. *International Journal of Heat and Mass Transfer*, 2016.

[78] N. Fries, K. Odic, M. Conrath, and M. Dreyer. The effect of evaporation on the wicking of liquids into a metallic weave. *Journal of Colloid and Interface Science*, 2008.

[79] E. Fragiadaki, S. Harhalakis, and E.P. Kalogianni. Characterization of porous media by dynamic wicking combined with image analysis. *Colloids and Surfaces A: Physicochemical and Engineering Aspects*, 2012.

[80] L. J. Gibson. The hierarchical structure and mechanics of plant materials. *Journal of the Royal Society of Society Interface*, 2012.

[81] I. Zlotnikov, D. Shilo, Y. Dauphin, H. Blumtritt, P. Werner, E. Zolotoyabkoe, and P. Fratzla. In situ elastic modulus measurements of ultrathin protein-rich organic layers in biosilica: Towards deeper understanding of superior resistance to fracture of biocomposites. *RSC Adv*, 2013.

[82] C. Xu, Z. Wei, H. Gao, Y. Bai, H. Liu, H. Yang, Y. Lai, and L. Yang. Bioinspired mechano-sensitive macroporous ceramic sponge for logical drug and cell delivery. *Advanced Science*, 2017.

[83] L.C. Palmer, C.J. Newcomb, S.R. Kaltz, E.D. Spoerke, and S.I. Stupp. Biomimetic systems for hydroxyapatite mineralization inspired by bone and enamel. *Chemical Reviews*, 2008.

[84] N. Reznikov, R. Shahar, and S. Weiner. Bone hierarchical structure in three dimensions. *Acta Biomaterialia*, 2014.

[85] L. Jin, X. Huang, G. Zeng, H. Wu, and M. Morbidelli. Conductive framework of inverse opal structure for sulfur cathode in lithium-sulfur batteries. *Scientific Reports*, 2016.

[86] H. Zhang, X. Yu, and P.V. Braun. Three-dimensional bicontinuous ultrafast-charge and-discharge bulk battery electrodes. *Nature nanotechnology*, 6(5):277–281, 2011.

[87] T. Semenic and I. Catton. Experimental study of biporous wicks for high heat flux applications. *International Journal of Heat and Mass Transfer*, 2009.

[88] Q. Cai and C. Chen. Design and test of carbon nanotube biwick structure for high-heat-flux phase change heat transfer. *Journal of Heat Transfer*, 2010.

[89] J. Liu, H.G. Zhang, J. Wang, J. Cho, J.H. Pikul, E.S. Epstein, X. Huang, J. Liu, W.P. King, and P.V Braun. Hydrothermal fabrication of three-dimensional secondary battery anodes. *Advanced Materials*, 2014.

[90] P.A. Shinde, Y. Seo, S. Lee, Q.N. Pham, and S.C. Jun Y. Won. Layered manganese metal-organic framework with high specific and areal capacitance for hybrid supercapacitors. *Chemical Engineering Journal*, 2020.

[91] J.-M. Vanson, A. Boutin, M. Klotz, and F.-X. Coudert. Transport and adsorption under liquid flow: the role of pore geometry. *Soft Matter*, 2017.

[92] J.-J. Lv, M. Jouny, W. Luc, W. Zhu, J.-J. Zhu, and F. Jiao. A highly porous copper electrocatalyst for carbon dioxide reduction. *Advanced Materials*, 2018.

[93] P.P. Dubey, Q.N. Pham, H. Cho, and Y. Won Y. Kim. Controlled wetting properties through heterogeneous surfaces containing two-level nanofeatures. *ACS Omega*, 2017.

[94] L.-P. Lefebvre, J. Banhard, and D.C. Dunand. Porous meta ls and metalli foams :current status and recent developments. *Advanced Engineering Materials*, 2008.

[95] F. Gritti and G. Guiochon. Perspectives on the evolution of the column efficiency in liquid chromatography. *Analytical Chemistry*, 2013.

[96] S.J. Harris and P. Lu. Effects of inhomogeneities—nanoscale to mesoscale—on the durability of li-ion batteries. *Journal of Physical Chemistry C*, 2013.

[97] M. Milina, S. Mitchell, P. Crivelli, D. Cooke, and J. Pérez-Ramírez. Mesopore quality determines the lifetime of hierarchically structured zeolite catalysts. *Nature Communications*, 2014.

[98] P. Zhu, T. Kong, X. Tang, and L. Wang. Well-defined porous membranes for robust omniphobic surfaces via microfluidic emulsion templating. *Nature Communication*, 2017.

[99] E.M. Herzig, K.A. White, A.B. Schofield, W.C.K. Poon, and P.S. Clegg. Bicontinuous emulsions stabilized solely by colloidal particles. *Nature Materials*, 2007.

[100] H. Rho, S. Lee, S. Bae, T.-W. Kim, D.S. Lee, H.J. Lee, J.Y. Hwang, T Jeong, S. Kim, J.-S. Ha, and S.H. Lee. Three-dimensional porous copper-graphene heterostructures with durability and high heat dissipation performance. *Scientific Reports*, 2015.

[101] J.D. Mendlesohn, C.J. Barrett, V.V. Chan, A.J. Pal, A.M. Mayes, and M.F. Rubner. Fabrication of microporous thin films from polyelectrolyte multilayers. *Langmuir*, 2000.

[102] H.-C. Shin and M. Liu. Copper foam structures with highly porous nanostructured walls. *Chemistry of Materials*, 2004.

[103] A. Celebioglu and T. Uyar. Electrospinning of nanofibers from non-polymeric systems: polymer-free nanofibers from cyclodextrin derivatives. *Nanoscale*, 2012.

[104] V. Baranaua and U. Tallarek. Random-close packing limits for monodisperse and polydisperse hard spheres. *Soft Matter*, 2014.

[105] H. Liasneuski, D. Hlushkou, S. Khirevich, Höltzel, U. Tallarek, and S. Torquato. Impact of microstructure on the effective diffusivity in random packings of hard spheres. *Journal of Applied Physics*, 2014.

[106] A.B.D. Nandiyanto, N. Hagura, F. Iskandar, and K. Okuyama. Design of a highly ordered and uniform porous structure with multisized pores in film and particle forms using a template-driven self-assembly technique. *Acta Materialia*, 2010.

[107] Y.-H. Ye, F. LeBlanc, A. Haché, and V.-V. Truong. Self-assembling three-dimensional colloidal photonic crystal structure with high crystalline quality. *Applied Physics Letters*, 78(1):52–54, 2001.

[108] X. Zhou, C. Liu, Z. Zhang, L. Jiang, and J. Li. A novel nanogold multilayer constructed by langmuir–blodgett and self-assembly techniques. *Journal of Colloid and Interface Science*, 2005.

[109] D.S. Raimundo, B. Hatton, M. Kolle, and J. Aizenberg. Self-assembled polystyrene micro-spheres applied for photonic crystals and templates fabrication. *Journal of Integrated Circuits and System*, 1:39–43, 2006.

[110] A. Sharstniou, S. Niazuzorau, P.M. Ferreira, and B.P. Azeredo. Electrochemical nanoimprinting of silicon. *Proceedings fo the National Academy of Sciences of the United States of America*, 2019.

[111] S.M. Kamali, S. Arbabi, H. Kwon, and A. Faraon. Metasurface-generated complex 3-dimensional optical fields for interference lithography. *Proceedings fo the National Academy of Sciences of the United States of America*, 2019.

[112] X. Zhang, A. Vyatskikh, H. Gao, J.R. Greer, and X. Li. Lightweight, flaw-tolerant, and ultrastrong nanoarchitected carbon. *Proceedings fo the National Academy of Sciences of the United States of America*, 2019.

[113] M. Farsari, M. Vamvakaki, and B. N. Chichkov. Multiphoton polymerization of hybrid materials. *Journal of Optics*, 2010.

[114] I. Yadroitsev, I. Shishkovsky, P. Bertrand, and I. Smurov. Manufacturing of fine-structured 3d porous filter elements by selective laser melting. *Applied Surface Science*, 2009.

[115] W.Y. Yeong, N. Sudarmadji, H.Y.Y. Yu, C.K. Chua, K.F. Leong, S.S. Venkatraman, Y.C.F. Boey, and L.P. Tan. Porous polycaprolactone scaffold for cardiac tissue engineering fabricated by selective laser sintering. *Acta Biomaterialia*, 2010.

[116] S. Guddati, A.S.K. Kiran, M. Leavy, and S. Ramakrishna. Recent advancements in additive manufacturing technologies for porous material applications. *International Journal of Advanced Manufacturing Technology*, 2019.

[117] D.D. Gu, W. Meiners, K. Wissenbach, and R. Poprawe. Laser additive manufacturing of metallic components: materials, processes and mechanisms. *International Materials Reviews*, 2012.

[118] A.E. Aliev, S.B. Lee, R.H. Baughman, and A.A. Zakhidov. Thermal properties of carbon inverse opal photonic crystals. *Journal of Luminescence*, 2007.

[119] H. Huang, J. Chen, Y. Yu, Z. Shi, H. Möhwald, and G. Zhang. Controlled gradient colloidal photonic crystals and their optical properties. *Colloids and Surfaces A: Physicochemical and Engineering Aspects*, 428:9–17, 2013.

[120] R. Kubrin, R.M. Pasquarelli, M. Waleczek, H.S. Lee, R. Zierold, J.J. do Rosário, P.N. Dyachenko, J.M. Montero Moreno, A.Y. Petrov, and R. Janssen. Bottom-up fabrication of multilayer stacks of 3d photonic crystals from titanium dioxide. *ACS Applied Materials & Interfaces*, 8(16):10466–10476, 2016.

[121] M.A. McLachlan, N.P. Johnson, M. Richard, and D.W McComb. Thin film photonic crystals: synthesis and characterisation. *Journal of Materials Chemistry*, 14(2):144–150, 2004.

[122] Y.A. Vlasov, V.N. Astratov, A.V. Baryshev, A.A. Kaplyanskii, O.Z. Karimov, and M.F. Limonov. Manifestation of intrinsic defects in optical properties of self-organized opal photonic crystals. *Physical Review E*, 2000.

[123] Q. Yan, L.K. Teh, Q. Shao, C.C. Wong, and Y.-M. Chiang. Layer transfer approach to opaline hetero photonic crystals. *Langmuir*, 24(5):1796–1800, 2008.

[124] K.R. Phillips, G.T. England, S. Sunny, E. Shirman, T. Shirman, N. Vogel, and J. Aizenberg. A colloidoscope of colloid-based porous materials and their uses. *Chemical Society Reviews*, 2015.

[125] E. Armstrong and C. O'Dwyer. Artificial opal photonic crystals and inverse opal structures – fundamentals and applications from optics to energy storage. *Journal of Materials Chemistry C*, 2015.

[126] G. Collins, M. Blomker, M. Osiak, J.D. Holmes, M. Bredol, and C. O'Dwyer. Three-dimensionally ordered hierarchically porous tin dioxide inverse opals and immobilization of palladium nanoparticles for catalytic applications. *Chemistry of Materials*, 25(21):4312–4320, 2013.

[127] C.-T. Hsieh, C.-L. Huang, Y.-A. Chen, and S.-Y. Lu. Nifemo alloy inverse-opals on ni foam as outstanding bifunctional catalysts for electrolytic water splitting of ultra-low cell voltages at high current densities. *Applied Catalysis B: Environmental*, 2019.

[128] D.K. Rhee, B. Jung, Y.H. Kim, S.J. Yeo, S.-J. Choi, A. Rauf, S. Han, G.-R. Yi, D. Lee, and P.J. Yoo. Particle-nested inverse opal structures as hierarchically structured large-scale membranes with tunable separation properties. *ACS Applied Materials & Interfaces*, 2014.

[129] Y.-J. Lee and P.V. Braun. Tunable inverse opal hydrogel ph sensors. *Advanced Materials*, 2003.

[130] D.Y. Kim, J. Suk, D.W. Kim, Y. Kang, S.H. Im, Y. Yang, and O.O. Park. An electrochemically grown three-dimensional porous si@ ni inverse opal structure for high-performance li ion battery anodes. *Journal of Materials Chemistry A*, 2(18):6396–6401, 2014.

[131] Y. Cho, S.Y. Lee, L. Ellerthorpe, G. Feng, G. Lin, G. Wu, J. Yin, and S. Yang. Elastoplastic inverse opals as power-free mechanochromic sensors for force recording. *Advanced Functional Materials*, 2015.

[132] Q. Wang and R. Chen. Ultrahigh flux thin film boiling heat transfer through nanoporous membranes. *Nano Letters*, 2018.

[133] Q.N. Pham, S. Zhang, L. Cheng-Hui, S. Hao, and Y. Won. Boiling heat transfer performance of three-dimensionally ordered microporous copper with modulated pore diameters. In *International Electronic Packaging Technical Conference and Exhibition*, 2018.

[134] Q.N. Pham, Y. Suh, B. Shao, and Y. Won. Boiling heat transfer using spatially-variant and uniform microporous coatings. *ASME 2019 International Technical Conference and Exhibition on Packaging and Integration of Electronic and Photonic Microsystems*, 2019.

[135] H. Lee, T. Maitra, J. Palko, C. Zhang, M.T. Barako, Y. Won, M. Asheghi, and K.E. Goodson. Copper inverse opal surfaces for enhanced boiling heat transfer. In *ASME 2017 International Technical Conference and Exhibition on Packaging and Integration of Electronic and Photonic Microsystems*, 2017.

[136] T.J. Dusseault, J. Gires, M.T. Barako, Y. Won, D.D. Agonafer, M. Asheghi, J.G. Santiago, and K.E. Goodson. Inverse opals for fluid delivery in electronics cooling systems. In *Thermal and Thermomechanical Phenomena in Electronic Systems (ITherm)*, 2014.

[137] Q.N. Pham, S. Zhang, K. Montazeri, and Y. Won. Droplets on slippery lubricant-infused porous surfaces: A macroscale to nanoscale perspective. *Langmuir*, 2018.

[138] Q.N. Pham, S. Zhang, S. Hao, K. Montazeri, C.-H. Lin, J. Lee, A. Mohraz, and Y. Won. Boiling heat transfer with a well-ordered microporous architecture. *ACS Applied Materials & Interfaces*, 2020.

[139] J.F. Galisteo-López, M. Ibisate, R. Sapienza, L.S. Froufe-Pérez, Á. Blanco, and C. López. Self-assembled photonic structures. *Advanced Materials*, 2011.

[140] P.V. Braun. Materials chemistry in 3d templates for functional photonics. *Chemistry of Materials*, 2013.

[141] S.-M. Yang, S.G. Jang, D.G. Choi, S. Kim, and H.K. Yu. Nanomachining by colloidal lithography. *Small*, 2006.

[142] A. Stein, F. Li, and N.R. Denny. Morphological control in colloidal crystal templating of inverse opals, hierarchical structures, and shaped particles. *Chemistry of Materials*, 2008.

[143] R. Rengarajan, P. Jiang, D.C. Larrabee, V.L. Colvin, and D.M. Mittleman. Colloidal photonic superlattices. *Physical Review B*, 64(20):205103, 2001.

[144] P. Jiang, J.F. Bertone, K.S. Hwang, and V.L. Colvin. Single-crystal colloidal multi-layers of controlled thickness. *Chemistry of Materials*, 11(8):2132–2140, 1999.

[145] Q.N. Pham. Fabrication of copper inverse opals for microscale liquid transport in polycrystalline porous media. Master's thesis, UC Irvine, 2018.

[146] M.T. Barako, A. Sood, C. Zhang, J. Wang, T. Kodama, M. Asheghi, X. Zheng, P.V. Braun, and K.E. Goodson. Quasi-ballistic electronic thermal conduction in metal inverse opals. *Nano Letters*, 16(4):2754–2761, 2016.

[147] R.G. Shimmin, A.J. DiMauro, and P.V. Braun. Slow vertical deposition of colloidal crystals: A langmuir- blodgett process? *Langmuir*, 22(15):6507–6513, 2006.

[148] L. Wang and X.S. Zhao. Fabrication of crack-free colloidal crystals using a modified vertical deposition method. *Journal pf Physical Chemistry C*, 2007.

[149] A. Blanco, E. Chomski, S. Grabtchak, M. Ibisate, S. John, S. W. Leonard, C. Lopez, F. Meseguer, H. Miguez, J. P. Mondia, G. A. Ozin, O. Toader, and H. M van Driel. Large-scale synthesis of a silicon photonic crystal with a complete three-dimensional bandgap near 1.5 micrometres. *Nature*, 2000.

[150] S.H. Park and Y. Xia. Macroporous membranes with highly ordered and three-dimensionally interconnected spherical pores. *Advanced Materials*, 1999.

[151] Y.G. Ko, D.H. Shin, G.S. Lee, and U.S. Choi. Fabrication of colloidal crystals on hydrophilic/hydrophobic surface by spin-coating. *Colloids and Surfaces A: Physicochemical and Engineering Aspects*, 2011.

[152] J.S. Katz T. Liu K.E Goodson J. Tice M.T. Barako, S. Lingamneni. Optimizing the design of composite phase change materials for high thermal power density. *Journal of Applied Physics*, 2018.

[153] M.T. Barako, V. Gambin, and J. Tice. Integrated nanomaterials for extreme thermal management: a perspective for aerospace applications. *Nanotechnology*, 29(15):154003, 2018.

[154] C. Zhang, J.W. Palko, G. Rong, K.S. Pringle, M.T. Barako, T.J. Dusseault, M. Asheghi, J.G. Santiago, and K.E. Goodson. Tailoring permeability of microporous copper structures through template sintering. *ACS Applied Materials & Interfaces*, 2018.

[155] C. Zhang, J. W. Palko, M. T. Barako, M. Asheghi, J. G. Santiago, and K. E. Goodson. Enhanced capillary-fed boiling in copper inverse opals via template sintering. *Advanced Functional Materials*, 2018.

[156] F. Nan, Z. Kang, J. Wang, M. Shen, and L. Fang. Carbon quantum dots coated bivo4 inverse opals for enhanced photoelectrochemical hydrogen generation. *Applied Physics Letters*, 2015.

[157] D.N. Nguyen and H. Yoon. Recent advances in nanostructued conducting polymer: from synthesis to practical applications. *Polymers*, 2016.

[158] Q. Zhong, H. Xu, H. Ding, L. Bai, Z. Mu, Z. Xie, Y. Zhao, and Z. Gu. Preparation of conducting polymer inverse opals and its application as ammonia sensor. *Colloids and Surfaces A: Physicochemical and Engineering Aspects*, 2013.

[159] P. Jiang, J. Cizeron, J. F. Bertone, and V. L. Colvin. Preparation of macroporous metal films from colloidal crystals. *Journal of the American Chemical Society*, 1999.

[160] J. Ma, B.R. Parajuli, M.G. Ghossoub, A. Mihi, J. Sadhu, P.V. Braun, and S. Sinha. Coherent phonon-grain boundary scattering in silicon inverse opals. *Nano Letters*, 2013.

[161] Y.-J. Lee, S.A. Pruzinsky, and P.V. Braun. Glucose-sensitive inverse opal hydrogels: Analysis of optical diffraction response. *Langmuir*, 2004.

[162] Y. Suh, Q.N. Pham, B. Shao, and Y. Won. The control of colloidal grain boundaries through evaporative vertical self-assembly. *Small*, 2019.

[163] C. Jin, M.A. McLachlan, D.W. McComb, R.M. De La Rue, and N.P. Johnson. Template-assisted growth of nominally cubic (100)-oriented three-dimensional crack-free photonic crystals. *Nano Letters*, 2005.

[164] B. Hatton, L. Mishchenko, S. Davis, K.H. Sandhage, and J. Aizenberg. Assembly of large-area, highly ordered, crack-free inverse opal films. *Proceedings fo the National Academy of Sciences of the United States of America*, 107(23):10354–10359, 2010.

[165] J. Zhou, J. Wang, Y. Huang, G. Liu, L. Wang, S. Chen, X. Li, D. Wang, Y. Song, and L. Jiang. Large-area crack-free single-crystal photonic crystals via combined effects of polymerization-assisted assembly and flexible substrate. *NPG Asia Materials*, 2012.

[166] A.A. Chabanov, Y. Jun, and D.J. Norris. Avoiding cracks in self-assembled photonic band-gap crystals. *Applied Physics Letters*, 84(18):3573–3575, 2004.

[167] A. Rogacs, J.E. Steinbrenner, J.A. Rowlette, J.M. Weisse, X.L. Zheng, and K.E. Goodson. Characterization of the wettability of thin nanostructured films in the presence of evaporation. *Journal of Colloid and Interface Science*, 2010.

[168] Y. Zhu, D.S. Antao, Z. Lu, S. Somasundaram, T. Zhang, and E.N. Wang. Prediction and characterization of dry-out heat flux in micropillar wick structures. *Langmuir*, 2016.

[169] A. Anbari, H.-T. Chien, S.S. Datta, W. Deng, D.A. Weitz, and J. Fan. Microfluidic model porous media: Fabrication and applications. *Small*, 2018.

[170] K. Xu, T. Liang, P. Zhu, P. Qi, J. Lu, C. Huh, and M. Balhoff. A 2.5-d glass micromodel for investigation of multi-phase flow in porous media. *Lap Chip*, 2017.

[171] A.T. Krummel, S.S. Datta, S. Münster, and D. A. Weitz. Visualizing multiphase flow and trapped fluid configurations in a model three-dimensional porous medium. *AlChE Journal*, 2013.

[172] M. Khishvand, A.H. Alizadeh, and M. Piri. In-situ characterization of wettability and pore-scale displacements during two- and three-phase flow in natural porous media. *Advances in Water Resources*, 2016.

[173] A. AlRatrout, M.J. Blunt, and B. Bijeljic. Wettability in complex porous materials, the mixed-wet state, and its relationship to surface roughness. *Proceedings fo the National Academy of Sciences of the United States of America*, 2018.

[174] S. Berg, H. Ott, S.A. Klapp, A. Schwing, R. Neiteler, N. Brussee, A. Makurat, L. Leu, F. Enzmann, J.-O. Schwarz, M. Kersten, S. Irvine, and M. Stampanoni. Real-time 3d imaging of haines jumps in porous media flow. *Proceedings fo the National Academy of Sciences of the United States of America*, 2013.

[175] T. Pak, I.B. Butler, S. Geiger, M.I.J. van Dijke, and K.S. Sorbie. Droplet fragmentation: 3d imaging of a previously unidentified pore-scale process during multiphase flow in porous media. *Proceedings fo the National Academy of Sciences of the United States of America*, 2015.

[176] Y. Li, Q. Yang, M. Li, and Y. Song. Rate-dependent interface capture beyond the coffee-ring effect. *Scientific Reports*, 2016.

[177] S. Berg and J.V. Wunnik. Shear rate determination from pore-scale flow fields. *Transport in Porous Media*, 2017.

[178] G. Ni, G. Li, and S. Boriskina. Steam generation under one sun enabled by a floating structure with thermal concentration. *Nature Energy*, 2016.

[179] H. Ghasemi, G. Ni, A. Marconnet, J. Loomis, S. Yerci, N. Miljkovic, and G. Chen. Solar steam generation by heat localization. *Nature Communications*, 2014.

[180] P. Raghupathi and S. Kandlikar. Characterization of pool boiling of seawater and regulation of crystallization fouling by physical aberration. *Heat Transfer Engineering*, 38, 09 2016.

[181] J.W. Palko, H. Lee, C. Zhang, T.J. Dusseault, T. Maitra, Y. Won, D.D. Agonafer, J. Moss, F. Houshmand, G. Rong, J.D. Wilbur, D. Rockosi, I. Mykyta, D. Resler, D. Altman, M. Asheghi, J.G. Santiago, and K.E. Goodson. Extreme two-phase cooling from laser-etched diamond and conformal, template-fabricated microporous copper. *Advanced Functional Materials*, 27(45):1703265, 2017.

[182] M. Tetreault-Friend, R. Azizian, M. Bucci, T. McKrell, J. Buongiorno, M. Rubner, and R. Cohen. Critical heat flux maxima resulting from the controlled morphology of nanoporous hydrophilic surface layers. *Applied Physics Letters*, 2016.

[183] V. S. Nikolayev, D. Chatain, Y. Garrabos, and D. Beysens. Experimental evidence of the vapor recoil mechanism in the boiling crisis. *Physical Review Letters*, 2006.

[184] H.S. Ahn, C. Lee, H. Kim, H. Jo, S. Kang, J. Kim, J. Sin, and M.H. Kim. Pool boiling chf enhancement by micro/nanoscale modification of zircaloy-4 surface. *Nuclear Engineering and Design*, 2010.

[185] S. Mori and Y. Utaka. Critical heat flux enhancement by surface modification in a saturated pool boiling: A review. *International Journal of Heat and Mass Transfer*, 2017.

[186] W. Wu, H. Bostanci, L.C. Chow, Y. Hong, M. Su, and J.P. Kizito. Nucleate boiling heat transfer enhancement for water and fc-72 on titanium oxide and silicon oxide surfaces. *International Journal of Heat and Mass Transfer*, 53(9):1773 – 1777, 2010.

[187] H.J. Jo, H.S. Ahn, S.H. Kang, and M.H. Kim. A study of nucleate boiling heat transfer on hydrophilic, hydrophobic and heterogeneous wetting surfaces. *International Journal of Heat and Mass Transfer*, 54(25):5643 – 5652, 2011.

[188] A.R. Betz, J. Xu, H. Qiu, and D. Attinger. Do surfaces with mixed hydrophilic and hydrophobic areas enhance pool boiling? *Applied Physics Letters*, 97(14):141909, 2010.

[189] A.R. Betz, J. Jenkins, C.-J. Kim, and D. Attinger. Boiling heat transfer on superhydrophilic, superhydrophobic, and superbiphilic surfaces. *International Journal of Heat and Mass Transfer*, 2013.

[190] M.M. Rahman, J. Pollack, and M. McCarthy. Increasing boiling heat transfer using low conductivity materials. *Scientific Reports*, 2015.

[191] J. Kim, S. Jun, R. Laksnarain, and S.M. You. Effect of surface roughness of pool boiling heat transfer at a heated surface having moderate wettability. *International Journal of Heat and Mass Transfer*, 2016.

[192] K.-H. Chu, R. Enright, and E. N. Wang. Structured surfaces for enhanced pool boiling heat transfer. *Applied Physics Letters*, 2012.

[193] C. Li, Z. Wang, P.-I. Wang, Y. Peles, N. Koratkar, and G. P. Peterson. Nanostructured copper interfaces for enhanced boiling. *Small*, 2008.

[194] N. S. Dhillon, J. Buongiorno, and K. K. Varanasi. Critical heat flux maxima during boiling crisis on textured surfaces. *Nature Communications*, 2015.

[195] M. Ha and S. Graham. Pool boiling characteristics and critical heat flux mechanisms of microporous surfaces and enhancement through structural modification. *Applied Physics Letters*, 2017.

[196] Y.C. Yortsos and A.K. Stubos. Phase change in porous media. *Current Opinion in Colloid & Interface Science*, 2001.

[197] P. Lloveras, F. Salvat-Pujol, L. Truskinovsky, and E. Vives. Boiling crisis as a critical phenomenon. *Physical Review Letters*, 2012.

[198] A.K. Sadghiani, A.R. Motezakker, S. Kasap, I.I. Kaya, and A. Kosar. Foamlike 3d graphene coatings for cooling systems involving phase change. *ACS Omega*, 2018.

[199] D.H. Min, G.S. Hwang, Y. Utsa, O.N. Cora, M. Koc, and M. Kaviany. 2-d and 3-d modulated porous coatings for enhanced pool boiling. *International Journal of Heat and Mass Transfer*, 2009.

[200] X. Ji, J. Xu, Z. Zhao, and W. Yang. Pool boiling heat transfer on uniform and non-uniform porous coating surfaces. *Experimental Thermal and Fluid Science*, 2013.

[201] H. Xu, R. Yan, S. Wang, and C.-L. Chen. Bubble detachment assisted by electrowetting-driven interfacial wave. *Physics on Fluids*, 2017.

[202] H. J. Cho, J. P. Mizerak, and E. N. Wang. Turning bubbles on and off during boiling using charged surfactants. *Nature Communication*, 2015.

[203] M.S. El-Genk and A.F. Ali. Enhanced nucleate boiling on copper micro-porous surfaces. *International Journal of Heat and Mass Transfer*, 2010.

[204] P. Xu, Q. Li, and Y. Xuan. Enhanced boiling heat transfer on composite porous surface. *International Journal of Heat and Mass Transfer*, 2015.

[205] A. Jaikumar and S.G. Kandlikar. Ultra-high pool boiling performance and effect of channel width with selectively coated open microchannels. *International Journal of Heat and Mass Transfer*, 2016.

[206] H. Kim, H.S. Ahn, and M.H. Kim. On the mechanism of pool boiling critical heat flux enhancement in nanofluids. *Journal of Heat Transfer*, 2010.

[207] S. Mori, S.M. Aznam, and K. Okuyama. Enhancement of the critical heat flux in saturated pool boiling of water by nanoparticle-coating and a honeycomb porous plate. *International Journal of Heat and Mass Transfer*, 2015.

[208] N. Sapoletova, T. Makarevich, K. Napolskii, E. Mishina, A. Eliseev, A. van Etteger, T. Rasing, and G. Tsirlina. Controlled growth of metallic inverse opals by electrodeposition. *Physical Chemistry Chemical Physics*, 12(47):15414–15422, 2010.

[209] A.V. Chumakova, G.A. Valkovskiy, A.A. Mistonov, V.A. Dyadkin, N.A. Grigoryeva, N.A. Sapoletova, K.S. Napolskii, A.A. Eliseev, Andrei V. Petukhov, and S.V. Grigoriev. Periodic order and defects in ni-based inverse opal-like crystals on the mesoscopic and atomic scale. *Physical Review B*, 90(14):144103, 2014.

[210] T. Sumida, Y. Wada, T. Kitamura, and S. Yanagida. Construction of stacked opaline films and electrochemical deposition of ordered macroporous nickel. *Langmuir*, 18(10):3886–3894, 2002.

[211] T.P. Allred, J.A. Weibel, and S.V. Garimella. The petal effect of parahydrophobic surfaces offers low receding contact angles that promote effective boiling. *International Journal of Heat and Mass Transfer*, 2019.

[212] R.N. Wenzel. Resistance of solid surfaces to wetting by water. *Industrial & Engineering Chemistry*, 1936.

[213] Y. Chen, R. Mertz, and R. Kulenovic. Numerical simulation of bubble formation on orifice plates with a moving contact line. *International Journal of Multiphase Flow*, 2009.

[214] N. Zuber. Nucleate boiling. the region of isolated bubbles and the similarity with natural convection. *international Journal of Heat and Mass Transfer*, 1963.

[215] H. Darcy. *Les fontaines publiques de la ville de Dijon: exposition et application...* Victor Dalmont, 1856.

[216] S.M. Rao and A. Balakrishnan. Analysis of pool boiling heat transfer over porous surfaces. *Heat and Mass Transfer*, 1997.

[217] D. A. Kofke. Direct evaluation of phase coexistence by molecular simulation via integration along the saturation line. *Journal of Chemical Physics*, 1993.

[218] R. Chen, M.C. Lu, V. Srinivasan, Z. Wang, H.H. Cho, and A. Majumdar. Nanowires for enhanced boiling heat transfer. *Nano Letters*, 2009.

[219] A. Zou and S.C. Maroo. Critical height of micro/nano structures for pool boiling heat transfer enhancement. *Applied Physics Letters*, 2013.

[220] H. Kim, H.S. Ahn, H.J. Kwak, M.H. Kim, and D.E. Kim. Boiling crisis controlled by capillary pumping and viscous friction: Liquid penetration length and dry spot diameter. *Applied Physics Letters*, 2016.

[221] Z. Yao, Y.-W. Lu, and S.G. Kandlikar. Effects of nanowire height on pool boiling performance of water on silicon chips. *International Journal of Thermal Sciences*, 2011.

[222] F.A.L. Dullien. *Porous media: Fluid transport and pore structure.* Academic Press, 2012.

[223] D.V. Le, Q.N. Pham, J. Lee, S. Zhang, and Y. Won. Evaporative wicking phenomena on nanotextured surfaces. *Journal of Electronic Packaging*, 2019.

[224] Z.-Z. Gu, A. Fujishima, and O. Sato. Fabrication of high-quality opal films with controllable thickness. *Chemistry of Materials*, 2002.

[225] A.N. Stachowiak, A. Bershteyn, E. Tzatzalos, and D.J. Irvine. Bioactive hydrogels with an orderedcellular structure combineinterconnected macroporosity androbust mechanical properties. *Advanced Materials*, 2004.

[226] K.Y. Lee, J. Chun, J.-H. Lee, K.N. Kim, N.-R. Kang, J.-Y. Kim, M.H. Kim, K.-S. Shin, M.K. Gupta, J.M. Baik, and S.-W. Kim. Hydrophobic sponge structure-based triboelectric nanogenerator. *Advanced Materials*, 2014.

[227] J. Xie, M. Doroshenko, U. Jonas, H.-J. Butt, and K. Koynov. Temperature-controlled diffusion in pnipam-modified silica inverse opals. *ACS Macro Letters*, 2016.

[228] T.D. Dziubla, M.C. Torjman, J.I. Joseph, M. Murphy-Tatumb, and A.M. Lowmana. Evaluation of porous networks of poly(2-hydroxyethyl methacrylate) as interfacial drug delivery devices. *Biomaterials*, 2001.

[229] C. Oshman, B. Shi, C. Li, R.G. Yang, Y.C. Lee, , and V.M. Bright. Fabrication and testing of a flat polymer micro heat pipe. *15th International Solid-State Sensors, Actuators and Microsystems Conference*, 2010.

[230] C. Oshman, L. Qian, L. Li-Anne, Y. Ronggui, V.M. Bright, , and Y.C. Lee. Flat flexible polymer heat pipes. *Journal of Micromechanics and Microengineering*, 2012.

[231] K. Montazeri, H. Lee, and Y. Won. Microscopic analysis of thin-film evaporation on spherical pore surfaces. *International Journal of Heat and Mass Transfer*, 2018.

[232] J. Oh, R. Zhang, P.P. Shetty, J.A. Krogstad, P.V. Braun, and N. Miljkovic. Thin film condensation on nanostructured surfaces. *Advanced Functional Materials*, 2018.

[233] K. Montazeri, S. Hao, M.J.A. Qomi, and Y. Won. Molecular dynamics investigation of liquid and vapor interactions near an evaporating interface: A theoretical genetics perspective. *Advanced Theory and Simulations*, 2020.

[234] J. Wang and I. Catton. Enhanced evaporation heat transfer in triangular grooves covered with a thin fine porous layer. *Applied Thermal Engineering*, 2001.

[235] J.W. Rose. Dropwise condensation theory and experiment: A review. *Proceedings of the Institution of Mechanical Engineers, Part A: Journal of Power and Energy*, 2002.

A   Copyright Permission

Figure A.1: Copyright Permission from *ACS Applied Materials & Interfaces.*

Figure A.2: Copyright Permission from *ACS Applied Materials & Interfaces.*

Figure A.3: Copyright Permission from *Langmuir*.

B Code

Listing B.1: MATLAB Detection and Measurement of Propagated Distance of a Wicking Front.

```matlab
clear all;
close all;


%% Inputs Needed
v = VideoReader('I:\UCI Nanoscale Architecture Lab\MATLAB\
   Nanoarchitecture Lab\Microscopic Wicking Motion\Videos\600
   nm_CuIO_exp32_1mgmL_long_repeat_002_singleChannels.wmv'); %
   insert video files
step=1:1:453; %frame steps and frame limits
time= step.*0.464; %time scale conversion: 1 frame = 0.464 s
y=90:1:950; %five horizontal lines separated by ˜200 px spacing
   ; 90:1:950 end



shift.ti=[49 86 138]; %when shifts start (Input needed [sec])
shift.tf=[57 95 147]; %when shifts finish (Input needed [sec])
shift.d=[954 679 439]; %camera translation distance  for each
   shift (Input needed) *hint:should divide by 2


for j=1:length(step)
    frame=read(v,step(j));
```

144

```matlab
        frame_bw=im2bw(frame,0.015); %convert to black and white
            with given threshold (Input needed)
        bw=imfill(frame_bw,'holes'); %fill any holes enclosed by
            boundaries for noise reduction
        for  i=1:length(y) %knowing that its 1080x1920 px frame
            resolution
            distance(j,i)=sum(bw(y(i),:)); %taking into account
                that 1 px = 1 um; ergo, no length scale conversion
                needed
        end
        meanHeight(j)=mean(distance(j,:))'; %retrieve average
            propagated height
        sd(j)=std(distance(j,:))'; %retrieve standard deviation
            between the five horizontal lines
end




for  i=1:length(y)
results(i).d=distance(:,i);
results(i).t=step'.*0.464;
results(i).line=y(i);



for ii=1:length(shift.ti) % Adjustment due to camera shifting
```

```matlab
        t1=find(results(i).t>=shift.ti(ii),1);t2=find(results(i).t
            >=shift.tf(ii),1); %determine the time span during
            camera shift
        results(i).d(t1:t2)=NaN; %if camera is shifting, nullify
            the data
        results(i).d(t2:end)=results(i).d(t2:end)+shift.d(ii); %add
             the translation distance onto values to account for the
            camera shifting
    end


% noise reduction through end of frame view and screen
    translation
for j=3:length(step)
    if distance(j,i)<distance(j-1,i) && distance(j-1,i)<=
        distance(j-2,i) %if distance continually decreasing,
        this means camera is shiftting
        mask2(j,i)=j;
        results(i).d(j,1)=NaN; %nullify such data
    end
    if distance(j,i)>=1040 %if distance is approximately
        greater than 1040 px, this means liquid front is
        approaching the end of the screen
        mask2(j,i)=j;
        results(i).d(j,1)=NaN; %nullify such data to eliminate
            inaccurate data
    end
end
```

```matlab
% initializing the start of liquid propagation at around t = 0
    sec
for j=2:(length(mask2(:,i))-1)
    if mask2(j,i)>0 && mask2(j-1,i)==0 && mask2(j+1,i)==0
        mask2(j,i)=0;
        results(i).d(j,1)=NaN;
    end
end


mask(i)=find(results(i).d<40,1,'last'); %if values of distances
    is less than 30
results(i).d=results(i).d((1+mask(i)):end,1)*0.001; % shift
    distance value %%%%%%%%%%%%%%%%%%%%%%%%%%%%%%%%%%%%%%%%%
results(i).t=results(i).t(1:(end-mask(i)),1); % and shift time
    value to the beginning
end


%% PLOTTING


figure(1);hold all;
for i=1:length(y)
%    time2=[1:1:length(Results(i).PropDistance)].*0.464;
%    plot(time2,Results(i).PropDistance);
```

```matlab
% errorHeight_plot=errorbar(results(i).t, meanHeight(j), sd(j))
  ;
% meanHeight_plot=plot(results(i).t, meanHeight(j), 'o');


    spatiotemp_freq_plot=plot(results(i).t,results(i).d,'-','
       MarkerFaceColor',[0.47 0.67 0.19],'MarkerEdgeColor'
       ,[0.0 0.67 0.19], 'color',[0.0 0.67 0.19],'linewidth'
       ,5);
    spatiotemp_freq_plot.Color(4)= 0.005;



    max_time(i) = length(results(i).t); %declaring new variable
       to retrieve the total time span after accounting for t0
       shift


end



%% STEP 2

% after plotting spatio-temporal frequency plot in STEP 1,
% manually determine the time frame during camera shift after
   t0;
% afterward, input the time frame in ti_mean and tf_mean array
```

```matlab
ti_mean=[21 63 115];tf_mean=[22 64 128]; %manual input of time
    frame [sec] between camera shift; inputted after observation
     of t0 shift


figure(2); hold all;
min_maaxtime=min(max_time);tmean=[1:1:min_maaxtime].*0.464; %
    determine the minimum length of the total time; declare time
     stamp variable for plotting average data points
for j=1:min_maaxtime %obtaining the mean and standard deviation
    of propagated height for each time stamp
    for i=1:length(y)
    distance2(j,i) = results(i).d(j);
    end
mean_d(j) = nanmean(distance2(j,:)); %determine the average
    value, ignoring nullified value
dev(j) = std(distance2(j,:),'omitnan'); %determine the standard
    deviation, ignoring nullified value
end


% take into account for time during camera shift, so that no
    mean values
% are plotted
for ii=1:length(shift.ti) % Adjustment due to camera shifting
    t1=find(tmean>ti_mean(ii),1);t2=find(tmean>=tf_mean(ii),1);
        %determine the time span during camera shift
    mean_d(t1:t2)=NaN; %if camera is shifting between the
        specified time frame, nullify the data in between
```

```matlab
end
% errorbar([1:1:min_maaxtime].*0.464,mean_d,dev);
% plot([1:1:min_maaxtime].*0.464,mean_d, '-', 'linewidth', 1.5)
   ;



% superimposing mean and standard deviation values on top of
   raw spatio-temporal frequency data
for i=1:length(y)
  spatiotemp_freq_plot=plot(results(i).t,results(i).d,'-', '
     color',[0.2 .4 0.2],'linewidth',2.5);
     spatiotemp_freq_plot.Color(4)= 0.003;
end


nanflag = {'gap'}; %plot by bounding the upper and lower
   standard deviation while omitting missing data during camera
    shift
[hl, hp]=boundedline([1:1:min_maaxtime].*0.464,mean_d,dev, 'nan
   ', nanflag, 'alpha', 'k-');
ho=outlinebounds(hl,hp);
set(hl, 'linewidth', 3);



%% PLOTTING PARAMETERS
xlim([0 167]);
```

150

```matlab
hXLabel=xlabel('Time (s)');
hYLabel=ylabel('Propagation Distance (mm)');
box on
x0=0;
y0=0;
width=420;
height=315;
set(gcf,'units','points','position',[x0,y0,width,height])

set( gca                          , ...
    'FontName'    , 'arial' );
set(gca                , ...
    'FontSize'    , 15              );
set([hXLabel, hYLabel]   , ...
    'FontSize'    , 16              );

hold off
```

Listing B.2: Monte Carlo Simulation of Hydraulic Transport in Polycrystalline Porous Media.

```matlab
clc;
clear all% Clear the command window.
close all;  % Close all figures (except those of imtool.)
clear;  % Erase all existing variables. Or clearvars if you
   want.
workspace;  % Make sure the workspace panel is showing.
format long g;
format compact;
fontSize = 20;
hold all

%intrinsic permeability distribution
%using excel fit and distribution
K_mean = @(d) 0.0363e-16*exp(-0.0007*d./1e-6); % unit in m
K_sigma = @(d) K_mean(d)./3.3e-18*1.306e-18; % unit in m

%crystalline domain travel length in unit of m
%based on normalized distrubtion of domain length of width
Lmu=77.64E-6;
Lsigma=25.45E-6;

%Grain boundary width distribution
GBmu=3.0E-6; %unit in m
GBsigma=1.2E-6; %unit in m
```

```matlab
%Fluid and Porous Structure Parameters
porosity=0.909;
viscosity=0.87; %mPa*s
r_eff=4.04e-7; % effective pore radius in unit of m
surftension=76.35; %mN/m



count=100; %number of Monte Carlo trial runs
maxL=3.5E-3; %max sample length in unit of m
maxTime=350; %max experiment time in unit of s
for i=1:count
    %initialize parameters
    j=1;
    time(i,j)=0;
    dist(i,j)=0;


while time(i,j)<maxTime && dist(i,j) <= maxL
  j=j+1;
  time0 = time(i,j-1); dist0 = dist(i,j-1); %time and distance
     at the begining of the grain



%probability of occurrence
K_0(i,j)=normrnd(K_mean(dist0),K_sigma(dist0));
while K_0(i,j)<0 K_0(i,j)=normrnd(K_mean(dist0),K_sigma(dist0))
    ;end
```

```matlab
%randomly retrieve travel length within single crystalline
    domain, which is
%dependent upon the direction of flow, since transverse flow
    direction has
%shorter mean free path travel distance in between boundary
    defects
crystal_travelLength=normrnd(Lmu,Lsigma);


for ii=1:300
%particle propagation inside grain based on Washburn Equation
dist(i,j)=dist(i,j-1)+ crystal_travelLength/300;
time(i,j)=time0+((dist(i,j)-dist0)^2*(r_eff*viscosity*porosity)
    /((4*surftension*K_0(i,j)))); %unit of s;
j=j+1;
K_0(i,j)=K_0(i,j-1);
end


%determine time stoppage at grain boundary as a function of
    distance and
%time, using 3D plane fitting
delta_t_avg=3.458E-6*dist(i,j-1)+4.738E-2*time(i,j-1)-2.197; %
    unit of s
if delta_t_avg <= 0
    delta_t_avg = 0;
end
```

```matlab
%randomly sample a grain boundary witdth to modify the average
    time
GB_width=normrnd(GBmu,GBsigma);


delta_t=GB_width*delta_t_avg./GBmu; %to determine the spread of
    delta t based on grain boundary widths
dist(i,j)=dist(i,j-1)+ GB_width; %distance propagation
    contributed by grain boundary width
time(i,j)=time(i,j-1)+ delta_t; %propagation distance
    contributed by delta t_GB


%halt archival of data generation once reach max sample size or
    max
%allocated propagation time
if time(i,j)>=maxTime || dist(i,j) >= maxL
dist(i,j)=NaN;
%determine the final height and height that are last recorded
h(i)=dist(i,j-1);
t(i)=time(i,j-1);
%determine the effective permeability based on the collective
    transport
%properties across multiple domains and boundaries
keff(i)=h.^2*r_eff*viscosity*porosity/(4*t*surftension);
end


end
```

```matlab
plot(time(i,:), dist(i,:).*10^3, 'color', [0.45 1 0.5], '
    LineWidth', 2);
end


%determine the average effective permeability over the number
    of trial runs
m=mean(keff)
```